Methodological contributions to the simulation of charge and energy transport in molecular materials

Zur Erlangung des akademischen Grades eines

DOKTORS DER NATURWISSENSCHAFTEN

(Dr. rer. nat)

der KIT-Fakultät für Chemie und Biowissenschaften

des Karlsruher Instituts für Technologie (KIT)

genehmigte

DISSERTATION

von

MSc ETH Julian J. Kranz

1. Referent: Prof. Dr. Marcus Elstner
2. Referent: Prof. Dr. Wolfgang Wenzel
Tag der mündlichen Prüfung: 17. Dezember 2017

Zusammenfassung

Diese Arbeit beschäftigt sich mit methodischen Entwicklungen zur Untersuchung von Ladungs- und Energietransportprozessen in molekularen Materialen. Damit ist gemeint, dass neue Ansätzen zur Untersuchung solcher Prozesse eingeführt und getestet, nicht etwa spezielle Prozesse im Detail ergründet, werden. Insbesondere liegt der Fokus auf Methoden zur Untersuchung organischer, halbleitender Materialien mit hohen Ladungsträgermobilitäten oder effizienter Ekzitonendiffusion, wobei die vorgestellten Methoden weitaus breiter anwendbar sind.

Zunächst wenden wir eine ursprünglich für den Ladungstransport in DNA-Strängen entwickelte, und später von Heck et al. für organische Halbleiter adaptierte, Methode auf Anthrazenkristalle an. Wir berechnen damit die korrekte Temperaturabhängigkeit der Lochmobilität. Diese ist eng mit dem zugrundeliegenden Transportmechanismus verwoben und kann im Falle von bandartigem Transport, wie in Anthrazen, nicht mit *hopping*basierten Methoden reproduziert werden. Daraufhin führen wir eine Methode zur Berechnung von Ekzitonendiffusionskonstanten in molekularen Materialien auf Basis der direkten Propagation der Ekzitonenwellenfunktion ein. Um solche Rechnungen möglich zu machen, werden unter Ausnutzung der molekularen Struktur Näherungen auf verschiedenen Ebenen eingeführt. Die neue Methode wird, um sie zu testen, auf Ekzitonentransport in Anthrazen angewendet und wir diskutieren dabei auch technische Details, die für die obig angesprochenen Ladungstransportstudien ebenfalls relevant sind.

Bei der Propagation der Ekzitonenwellenfunktion müssen viele elektronische Strukturrechnungen angeregter Zustände durchgeführt werden, so dass dazu eine sehr schnelle Methode notwendig ist. Wir verwenden die approximative TD-DFTB Methode, die auf DFT mit einem GGA Funktional basiert. Es ist bekannt, dass GGA Funktionale für ausgedehnte π-Elektronensysteme, wie sie in organischen Halbleitern ständig vorkommen, nicht zuverlässig sind. Innerhalb von DFT lösen sogenannte *long-range corrected* (LC) Funktionale das Problem. Wir führen LC Funktionale in TD-DFTB ein, was Änderung am Formalismus erfordert. Wir zeigen, dass damit typische Probleme mit π-Systemen und Ladungstransferanregungen gelöst werden, bei tausendfach schnelleren Rechnungen als mit konventionellem TD-DFT.

Abschließend beschäftigen wir uns mir der DFTB Methode selbst. LC Funktionale haben einen Parameter, der idealerweise systemspezifisch gewählt wird. Bei jeder Anpassung müssen für DFTB neue Parameter berechnet werden. Ein Satz von atompaarweisen Funktionen, genannt Repulsivpotentiale, erfordern dabei bisher viel Handarbeit. Wir versuchen diesen Vorgang zu automatisieren, indem wir DFTB mit Methoden aus der künstlichen Intelligenz verbinden.

Summary

This work is concerned with methodological developments for the study of charge and energy transport processes in molecular materials. That means new approaches to investigate such processes are introduced and tested, rather than specific processes studied in-depth. Special focus is put on methods to study organic, semiconducting materials with high charge carrier mobilities or efficient excitonic diffusion, although the presented methods have much broader applicability.

First, we apply a method, originally developed for charge transport in DNA strands, and later adapted by Heck et al. for organic semiconductors, to anthracene crystals. Hence, we calculate the correct temperature dependence of the hole mobility. This is closely related to the underlying transport mechanism and in the case of anthracene cannot be reproduced with hopping based methods.

Following up, we introduce a method for the calculation of exciton diffusion constants in molecular materials, based on the direct propagation of the exciton wavefunction. To permit such calculations, approximations on different levels are introduced, exploiting the molecular structure. In order to test it, this new method is applied to exciton transport in anthracene, and going along we discuss technical aspects, also relevant for the above mentioned charge transport studies.

Propagating the exciton wavefunction, many electronic structure calculations of excited states have to be performed, thus requiring a fast method. We use the approximate TD-DFTB method, based on DFT with a GGA functional. It is known that GGA functionals are not reliable for extended π-electron systems, as they occur ubiquitously in organic semiconductors. Within DFT, so-called long-range corrected (LC) functionals solve the problem. We introduce LC functionals in TD-DFTB, requiring changes to the formalism. We demonstrate that hence typical problems with π-systems and charge transfer excitations are solved, with thousandfold faster calculations compared to conventional TD-DFT.

Finally, we deal with the DFTB method itself. LC functionals have a parameter that is ideally chosen system-specific. For every adaption new DFTB parameters must be calculated. Therefore, a set of atom pairwise functions, called repulsive potentials, require much manual effort. We try to automatize this process by combining DFTB with methods from artificial intelligence.

Previous publication and copyright

Much of this work is based on the following published material:

- **Chapter 3**:
  Heck, A.[1], Kranz, J. J.[1], & Elstner, M. (2016).
  Simulation of Temperature-Dependent Charge Transport in Organic Semiconductors with Various Degrees of Disorder.
  J. Chem. Theory Comput., 12(7), 3087-3096.
  Reproduced are results and figures from the paper. However, the presentation and text is original.

- **Chapter 4**:
  Kranz, J. J., & Elstner, M. (2016).
  Simulation of singlet exciton diffusion in bulk organic materials.
  J. Chem. Theory Comput., 12(9), 4209-4221.
  Reproduced with some changes.

- **Chapter 5**:
  Kranz, J. J., Elstner, M., Aradi, B., Frauenheim, T., Lutsker, V., Garcia, A. D., & Niehaus, T. A. (2017).
  Time-dependent extension of the long-range corrected density functional based tight-binding method.
  J. Chem. Theory Comput., 13(4), 1737-1747.
  Reproduced with some changes.

- **Chapter 6**:
  Kranz, J. J. Kubillus, M., Ramakrishnan, R., von Lilienfeld, O. A., & Elstner, M. (2017).
  Generalized DFTB repulsive potentials from unsupervised machine learning.
  submitted for publication
  Reproduced with some changes. The final publication is likely to change throughout the review process.

The published material is under copyright of the American Chemical Society. See also the copyright notices on the first page of each chapter, as mandated by ACS policy.

---

[1]These authors contributed equally

Other related publications

The following two publications were created alongside the material presented in this thesis and are topically related. While their results are not presented, the insights gained inspired the rest of the work.

- Heck, A., Kranz, J. J., Kubar, T., & Elstner, M. (2015).
  Multi-scale approach to non-adiabatic charge transport in high-mobility organic semiconductors.
  J. Chem. Theory Comput., 11(11), 5068-5082.

- Berdakin, M., Taccone, M., Kranz, J. J., Pino, G., & Sanchez, C. G. (2016).
  Disentangling the Photophysics of DNA-Stabilized Silver Nanocluster Emitters.
  J. Phys. Chem. C, 120(42), 24409-24416.

Acknowledgments

First of all, I'd like to express my sincere gratitude to my adviser Marcus Elstner for not only offering me the opportunity to work in an exciting field and an outstanding team, but for truly letting me explore my interests, while always having good advice and an eye for the bigger picture. I have found this to be not at all self-evident throughout my short career.

I'm also indebted to Thomas Niehaus (Lyon) and Anatole von Lilienfeld (Basel) who were great co-advisers on some of my projects.

My previous academic advisers Aicko Schumann (Calgary/Charleston), Jörn Davidsen (Calgary), and Nuno Araújo (Zurich/Lisbon) taught me many useful things for which I'm still thankful.

Next, I want to thank my collaborators Alexander Heck, Maximilian Kubillus, Christián Sánchez (Córdoba), Adriel Domínguez García (MPI Hamburg), and Vitalij Lutsker (Regensburg) who brought so much to our joint work, Bálint Aradi who taught me the inner workings of DFTB+, and Tomáš Kubař who taught me the basics of our own code and usually knew something about everything.

The last three years wouldn't have been as much fun without the fine people of the TCB team who are not only colleagues, but friends. Many thanks to all of you!
Especially, had it not been for Sabine Holthoff, I might well have turned crazy over bureaucracy and gone broke over unreimbursed travel expenses.

Muchísimas gracias a mi futura esposa, Vega Pérez Wohlfeil, por tu apoyo continuo durante mi doctorado y en mi vida en general. Significa mucho para mí.
I also have to thank her for a lot of proof reading and help with some figures.

Abschließend möchte ich meiner Mutter Kornelia Kranz für ihre endlose Unterschtützung zeit meines Lebens danken, ohne die ich nicht wäre, wo ich bin.

Contents

1 Introduction

Charge and energy transport phenomena in molecular materials are of great practical relevance, as electronic components made of amorphous or crystalline organic materials have continuously gained popularity over the last decades. Many are produced at the large industrial scale, and hold great promise in terms of material properties and processability [1–3] over their inorganic counterparts, but performance for many applications still lacks behind. Organic semiconducting materials are commonly used in organic field effect transistors (OFETs) [4, 5], organic light emitting diodes (OLEDs) [6, 7], and organic photovoltaic devices (OPVs) [8, 9].

OPVs in particular provide a very good example for how charge and energy transport properties are relevant for device performance. In an organic solar cell, light is converted into electronic energy. Energy conversion happens in four steps: At first, incoming photons are absorbed in the bulk of the material; then the absorbed energy migrates to an interface in the form of an exciton, a bound electron-hole pair. Charges are separated at the interface in the third step, and eventually the separated electrons and holes migrate to the electrodes. With what ease excitons and charges can move around in the material thus crucially affects the efficiency of the device, since the longer it takes excitons and charges to reach interfaces and electrodes, the higher are the rates of premature deexcitation or charge recombination. In the light of its industrial significance, it is not surprising that charge and energy transport has been extensively studied experimentally and theoretically; theory is useful both in order to further understanding of the underlying mechanics of transport, allowing for educated molecular design, and as a predictive tool to sample the vast space of potential materials.

However, charge and energy transport can be very complicated phenomena. Charge transport, for instance, is well understood in the limiting regimes of very high charge carrier mobility, as found in inorganic semiconductors, and comparatively low carrier mobility, as in amorphous organic semiconductors. This last regime is known as the hopping regime, as charges are localized on individual molecules and move by way of thermally activated, random hops. In the case of high charge carrier mobility, transport is mostly determined by the electronic band structure and random charge-phonon scattering; hence, this limit is known as the band or band-like regime. The intermediate regime, though, is far less well understood. The building blocks of molecular materials are held together by dispersion interactions that are much weaker than the

forces between atoms in inorganic semiconductors or metals. This leads to large thermal fluctuations of the electronic couplings between molecules, and it appears that in the intermediate transport regime found in molecular crystals these fluctuations crucially affect transport [10], leading to an intricate interplay of electronic and nuclear degrees of freedom. In fact, for a long time thermal fluctuations of excitonic couplings have been ignored altogether [11, 12]. Because of this inherent complexity, there is much demand for novel methods in the field of charge and energy transport.

In the present work we contribute new tools for the study of transport processes in molecular materials. Some of the described methods are meant to be applied directly to study transport, while others are relevant in the context of those methods. Where transport itself is concerned, we test methods on organic semiconducting materials, like organic crystals. But the real scope of applicability is wider. A molecular material in our wider sense could be anything assembled from fragments of atoms, where interactions within the fragments are much stronger than among them – for example, a protein with individual amino acids as fragments. The existence of many potential applications is indeed a desirable feature, as we seek to make methodological contributions in this work, not study specific materials in-depth.

In the following, we will briefly introduce the contents of this work and explain how different parts are related and build upon each other.

We begin with an overview of the relevant theoretical background in chapter 2, where we also discuss the basics of charge and energy transport. Particularly, we will introduce in more detail the aforementioned limiting regimes of high and low mobility, and review the methods that are used to deal with them. This provides context for the next chapters.

In chapter 3 we apply a method that was originally developed to describe charge transport in DNA [13], and adapted for organic semiconductors by Heck et al. [14], to hole transport in an anthracene single crystal. Specifically, we will calculate the temperature dependence of the charge carrier mobility μ, as it is closely related to the underlying transport mechanism. Hole transport in anthracene is known to be band-like [15] despite fluctuation-induced charge localization [14]; thus, this is an example where no limiting case is valid. To account for the interplay of electronic and nuclear degrees of freedom, we will simulate the nonadiabatic dynamics of charge carriers and nuclei.

Chapter 4 extends this idea to exciton transport. A new method for the simulation of exciton transport in molecular materials, based on the propagation of the excitonic wavefunction in

time, is proposed and tested. In this context, several technical aspects are discussed, particularly the choice of the mixed quantum-classical, nonadiabatic dynamics scheme. Said discussion also bears relevance for the method from chapter 3.

Eventually, chapters 5 and 6 are concerned with the development of more general methods. It is well known that local and gradient-corrected DFT functionals perform poorly for spatially extended π-electron systems, which occur ubiquitously in organic semiconducting materials. The methods of chapters 3 and 4 rely on the density functional tight-bind method (DFTB), which in turn is an approximation to DFT with the underlying gradient-corrected PBE [16] functional. DFTB inherits the shortcomings of PBE, as becomes clear in chapter 4. Within DFT those problems can be solve by the introduction of long-range corrected functionals, which separate long and short ranged interactions and include long-range Hartree-Fock exchange. Long-range corrected functionals have only recently become available in DFTB [17], because they require alterations to the DFTB formalism. In chapter 4 we extend this new formalism to the time-dependent DFTB (TD-DFTB) formalism, leading to the long-range corrected TD-DFTB (LC-TD-DFTB) method for excited state calculations, and provide a computational implementation in the DFTB+ [18] program. Then we benchmark the qualitative and quantitative performance of this method, and we demonstrate by example that, indeed as in full DFT, the description of excitations involving extended π-electron systems is greatly improved. Furthermore, we show that charge transfer excitations, for which local DFT functionals fail completely, are well accounted for by LC-TD-DFTB. In conclusion, we provide a new method capable of dealing with excitations involving extended π-systems and charge transfer excitations at a thousandfold reduced computational cost compared to full DFT.

The final chapter, chapter 6, deals as well with aspects of the DFTB method, and is in part motivated by the new LC-DFTB method introduced in the previous chapter. As will be explained, the range-separation parameter ω that arises in LC-DFTB is in principle system dependent, but every change of ω requires a new parametrization of DFTB. While for most parameters reparametrization is straightforward, one set of terms (the so-called repulsive potentials) require much manual effort, rendering complete reparametrization difficult. Some progress has been made at automatizing the process [19–21], but a definitive solution is still missing. We propose an innovative approach combining DFTB with methods from unsupervised machine learning. Thus, we also attempt to move DFTB into the age of data-driven molecular modeling by enabling parametrization from uncurated and much larger data sets than so far can be meaningfully utilized.

2 Background

This chapter reviews some of the concepts and methodologies relevant in the context of charge and energy transport in molecular materials. We start out from the basic electronic structure problem, proceed with a discussion of different methods relevant for the understanding of the work presented in this book, and close with an overview of some of the models commonly used to describe transport processes in molecular materials, to put into context the results presented in the later chapters. Presentations are kept brief and expository; we try to touch upon most relevant topics, but not in detail. Extensive reviews of all topics can be found in many text books and the original literature.

2.1 Molecular simulation

2.1.1 The electronic structure problem

The fundamental object at the heart of quantum chemistry and condensed-matter physics is the molecular Hamiltonian that describes the interaction of electrons and atomic nuclei. In atomic units, where Planck's constant $\hbar$, and the electron charge e and mass m are set to unity, it reads:

$$H = \sum_i \frac{\mathbf{p}_i^2}{2} + \sum_k \frac{\mathbf{P}_k^2}{2M_k} + \frac{1}{2}\sum_{i \neq j} \frac{1}{|\mathbf{r}_i - \mathbf{r}_j|} + \frac{1}{2}\sum_{k \neq l} \frac{Z_k Z_l}{|\mathbf{R}_k - \mathbf{R}_l|} - \sum_{i,k} \frac{Z_k}{|\mathbf{r}_i - \mathbf{R}_k|}. \tag{2.1}$$

The $\mathbf{r}_i$ and $\mathbf{p}_i$ are the electronic positions and momenta, $\mathbf{R}_k$ and $\mathbf{P}_k$ those of the nuclei, and M_k, Z_k are the nuclear masses and charges. The fundamental commutator relations hold:

$$[r_{i\alpha}, r_{j\beta}] = [p_{i\alpha}, p_{j\beta}] = 0, \; [r_{i\alpha}, p_{j\beta}] = i\delta_{ij}\delta_{\alpha\beta} \tag{2.2}$$

for electrons, and likewise for nuclei. α, β label Cartesian coordinates, and δ_{ij} refers to the Kronecker delta. In the position representation, that is, using a basis of position eigenstates, the momentum operator takes the form $\mathbf{p} = -i\nabla_{\mathbf{r}}$. From the molecular Hamiltonian one commonly splits of the electronic Hamiltonian H_{elec} describing an electron cloud in an external electrostatic potential created by nuclei at fixed positions:

$$H_{\text{elec}} = \sum_i \frac{\mathbf{p}_i^2}{2} + \frac{1}{2}\sum_{i \neq j} \frac{1}{|\mathbf{r}_i - \mathbf{r}_j|} + \frac{1}{2}\sum_{k \neq l} \frac{Z_k Z_l}{|\mathbf{R}_k - \mathbf{R}_l|} - \sum_{i,k} \frac{Z_k}{|\mathbf{r}_i - \mathbf{R}_k|}. \tag{2.3}$$

The eigenvalue spectrum of H_{elec} then yields the electronic energy levels E_i, $i = 0, 1, 2, ...$:

$$H_{\text{elec}}|\psi_i\rangle = E_i|\psi_i\rangle, \tag{2.4}$$

with the electronic states $|\psi_i\rangle$. This eigenvalue problem is the time-independent electronic Schrödinger equation. The E_i as a function of the nuclear coordinates $E_i(\mathbf{R}_1, \mathbf{R}_2, ...)$ are called potential energy surfaces, as they act as an effective potential for the nuclei. Solids and molecules are stationary points on the lowest energy, or ground-state, surfaces. That is at molecular equilibrium geometries $\nabla_{\mathbf{R}} E_0(\mathbf{R}_1, ...) = 0$ holds.

The complete wavefunction $|\Psi\rangle$ of electrons and nuclei can be expanded using the electronic eigenstates:

$$|\Psi\rangle = \sum_i |\chi_i\rangle|\psi_i\rangle, \tag{2.5}$$

with nuclear wavefunctions $|\chi_i\rangle$. Applying the Hamiltonian to this form of the wavefunction and projecting out the electronic part results in

$$H|\chi_i\rangle = \left(\sum_k \frac{\mathbf{P}_k^2}{2M_k} + E_i(\mathbf{R}_1, ...) + \left[\sum_{j,k} \frac{1}{M_k} \left(2\langle\psi_i|\mathbf{P}_k|\psi_j\rangle\mathbf{P}_k + \langle\psi_i|\mathbf{P}_k^2|\psi_j\rangle \right) \right] \right) |\chi_i\rangle \tag{2.6}$$

for the Hamiltonian applied to the nuclear wavefunction. If the terms in square brackets, the so-called non-adiabatic couplings, are disregarded, the potential energy surfaces E_i act indeed as independent potentials for the nuclei. Such an assumption is known as the Born-Oppenheimer approximation and is valid whenever the energy levels are well separated, as is commonly the case near equilibrium molecular geometries. It breaks down when energy levels cross. The resulting non-adiabatic effects are of crucial importance especially for charge and energy transport processes because they allow transitions between different electronic states.

The time evolution of a quantum mechanical system obeys the time-dependent Schrödinger equation:

$$i\partial_i|\Psi(t)\rangle = H|\Psi(t)\rangle. \tag{2.7}$$

Much of this thesis is concerned with approximate solutions of eq. 2.7.

2.1.2 Density functional theory

The Hohenberg-Kohn theorems

While the molecular Hamiltonian looks alluringly simple at first glance, it is impossible to diagonalize it exactly for all but the smallest systems, because the dimension of the Hilbert space grows exponentially with the number of particles. Therefore, approximations are required

in practical application. One successful line of such approximations relies on an alternative formulation of the ground-state electronic structure problem in terms of the electron density

$$\rho(\mathbf{r}) = N \sum_{\sigma_1,...,\sigma_2} \int d^3 r_2 ... d^3 r_N \langle \psi | \mathbf{r}, \sigma_1, \mathbf{r}_2, \sigma_2, ..., \mathbf{r}_N, \sigma_N \rangle \langle \mathbf{r}, \sigma_1, \mathbf{r}_2, \sigma_2, ..., \mathbf{r}_N, \sigma_N | \psi \rangle \quad (2.8)$$

rather than the full wavefunction $|\psi\rangle$, where N is the number of electrons and σ labels spin degrees of freedom. The two Hohenberg-Kohn theorems [22] establish a connection between $\rho(\mathbf{r})$ and the electronic molecular ground state. They state respectively:

1. *There is a one-to-one correspondence, to within a constant shift, between the electronic ground state density $\rho_0(\mathbf{r})$ and the external potential $V_{ext}(\mathbf{r})$ acting on the electrons and leading to the density $\rho_0(\mathbf{r})$. In the case of molecules and solids V_{ext} is the electrostatic potential of the nuclei. Since V_{ext} fixes the entire Hamiltonian of the system, which in turn determines all properties, in principle the system is fully described by $\rho_0(\mathbf{r})$. In particular, there is a functional $E[\rho]$ that maps a density ρ to the energy $E[\rho] = \langle \psi[\rho] | H | \psi[\rho] \rangle$, where $|\psi[\rho]\rangle$ is the wavefunction that gives rise to density ρ.*

2. *The ground state density minimizes $E[\rho]$, that is $E[\rho_0] \leq E[\rho]$ for all densities ρ. This is the DFT equivalent to the Ritz variational principle, according to which the ground state wavefunction minimizes the energy expectation value.*

Hohenberg-Kohn theory guarantees the existence of $E[\rho]$ only for densities that come from a ground state for some external potential V_{ext}. The functional's scope has been extended in the work of Lieb [23] to more general, reasonable densities, so that it becomes differentiable. Hence, the second theorem leads to the condition

$$\frac{\delta E[\rho_0]}{\delta \rho} = 0, \quad (2.9)$$

which provides an equation for the ground state density and, hence, an alternative to the time-independent Schrödinger equation. So far, Hohenberg-Kohn theory is exact. However, no explicit form of $E[\rho]$ is known, and any such would likely exhibit the same exponential complexity as the exact wavefunction, so nothing would be gained. DFT has been successful because approximation of $E[\rho]$ have led to very efficient and reasonable accurate methods for calculations of molecules and solids.

The Kohn-Sham approach

We split up the functional $E[\rho]$ as

$$E[\rho] = T[\rho] + E_{xc}[\rho] + E_{H}[\rho] + \int d^3 r \, \rho(\mathbf{r}) V_{ext}(\mathbf{r}), \quad (2.10)$$

where $E_H = \int d^3r d^3r' \frac{\rho(\mathbf{r})\rho(\mathbf{r}')}{|\mathbf{r}-\mathbf{r}'|}$ is the classical Coulomb interaction of the electron density with itself, the final integral is the interaction of the density with the nuclear electrostatic potential, and the functionals $T[\rho]$ and E_{xc} entail all the complicated non-classical physics. $T[\rho]$ yields the electronic kinetic energy, and $E_{xc}[\rho]$ accounts for exchange and correlation. Now, Kohn and Sham's approach offers a simple expression for $T[\rho]$. A system of N interacting electrons is mapped to a system of N non-interacting electrons, with orthogonal single electron orbitals $|\phi_i\rangle$, $i = 1, ..., N$. The many-body wavefunction $|\psi\rangle$ for the non-interacting system is a single Slater determinant formed by the orbitals, and the kinetic energy is given by the expression for non-interacting electrons:

$$T[\phi_1, ...] = \sum_i \frac{1}{2}\langle\phi_i|\mathbf{p}_i^2|\phi_i\rangle. \tag{2.11}$$

In order to maintain the connection to the real, interacting system the density of both systems is set to be the same:

$$\rho(\mathbf{r}) = \sum_i |\langle\phi_i|r\rangle|^2. \tag{2.12}$$

Thus, the whole unknown physics is bundled in the exchange-correlation term $E_{xc}[\rho]$ that needs to account for the difference between the non-interacting and true kinetic energy, as well. Within this formalism, the variational principle eq. 2.9 leads to the set of single electron eigenvalue equations

$$\left(\frac{\mathbf{p}^2}{2} + V_{ext}(\mathbf{r}) + \frac{\delta E_{xc}[\rho]}{\delta\rho(\mathbf{r})}\right)|\phi_i\rangle = \varepsilon_i|\phi_i\rangle, \tag{2.13}$$

known as Kohn-Sham equation. From the equation, the orbitals can be found, and hence the energy through reinsertion into the functional. The orbital eigenvalues ε_i enter as Lagrangian multipliers for the orthonormality condition, and ε_N can be identified with the ionization potential by Janak's theorem [24]. Even though the orbitals $|\phi_i\rangle$ possess no a priori physical meaning, the frontier orbitals are often identified with real single electron wavefunctions, and this has been justified empirically [25].

Density functional approximation

The first attempts at a practical approximation of the exchange-correlation functional predate the rigorous foundations of DFT by Hohenberg and Kohn. Thomas and Fermi already put forward a model already in 1927 [26, 27] expressing the kinetic energy of an electron gas in terms of its density. However, their model predicts no stable molecules and is thus unfit for predictive quantum chemical applications. Successive developments have gradually improved the quantitative performance of DFT methods, while remaining computationally efficient, leading to their wide spread adoption, especially also among experimentalists. Two DFT papers are now among the ten most cited scientific works [28]. In the following, we introduce briefly a hierarchy of different functional approximations. Special attention will be payed to long-range

corrected functionals that provide the foundation for some of the work in this book and tend to be among the most accurate for many materials occurring in the context of molecular charge and energy transport.

Local density approximation

The local density approximation (LDA) goes back to the work of Kohn and Sham [29], and remains popular for solid-state systems, but is usually too inaccurate for molecules. The exchange-correlation energy is expressed as a density weighted integral over an energy density $\varepsilon_{xc}(\rho)$:

$$E_{xc}[\rho] = \int d^3 r \, \rho(\mathbf{r}) \varepsilon_{xc}(\rho(\mathbf{r})). \tag{2.14}$$

ε_{xc} is modeled by the expression for the homogeneous electron gas. Then, $\varepsilon_{xc} = \varepsilon_x + \varepsilon_c$, with the exchange contribution

$$\varepsilon_x(\rho) = -\frac{3}{4} \left(\frac{3}{\pi}\right)^{\frac{1}{3}} \rho(\mathbf{r})^{\frac{1}{3}} \tag{2.15}$$

as derived by Dirac [30]. The correlation contribution ε_c cannot be derived in closed form, but highly accurate quantum Monte Carlo results are available [31], to which analytic expressions can be fit [32–34]. LDA can be generalized to spin polarized systems, then known as local spin density approximation (LSDA), using the spin scaling relation:

$$E_x[\rho_\uparrow, \rho_\downarrow] = \frac{1}{2} \left(E_x[2\rho_\uparrow] + E_x[2\rho_\downarrow]\right), \tag{2.16}$$

which is a property of the exact functional. Here, $\rho_{\uparrow,\downarrow}$ are densities for the two different spin polarizations alone, and $E_x[\rho]$ is the exchange functional for an unpolarized system that has been approximated by the Dirac form. The correlation contribution has to be interpolated from the know unpolarized $\rho_\uparrow = \frac{\rho}{2} = \rho_\downarrow$ and fully polarized $\rho = \rho_\uparrow$ cases.

Generalized gradient approximation

LDA can only be truly useful for solids, rather than molecules, because its direct adoption from the uniform electron gas requires slowly varying densities. For this reason, corrections have been developed that take into account density fluctuations through inclusion of the density gradient $\nabla\rho(\mathbf{r})$:

$$E_{xc}[\rho] = \int d^3 r \, \rho(\mathbf{r}) \varepsilon_{xc}(\rho(\mathbf{r}), \nabla\rho(\mathbf{r})). \tag{2.17}$$

Such functionals are known as generalized gradient approximations (GGA). There is no unique way to approximate ε_{xc} in this way, but many different approaches exist. One popular GGA functional is the Perdew-Burke-Ernzerhof (PBE) functional [16]. It is derived by requiring that certain conditions known to hold for the exact functionals be reproduced by the approximative form. Therefore, it is free of fitted parameters and tends to be accurate for a broad range of
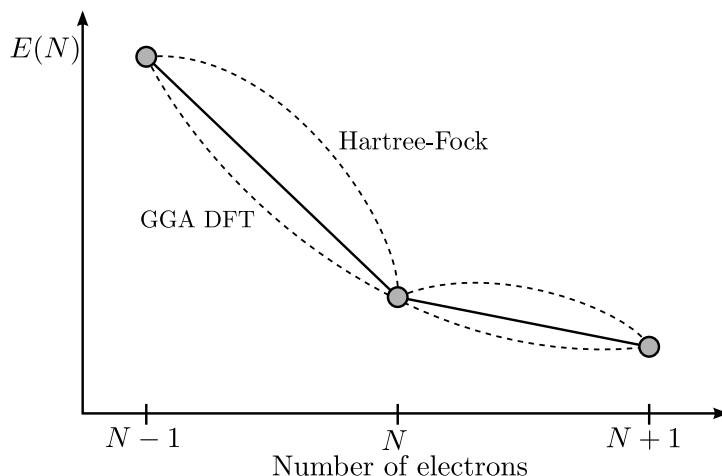
Figure 2.1: The self-interaction error of DFT functional approximations without Hartree-Fock exchange becomes apparent when the number of electrons deviates from the integers. Such scenarious can be defined in terms of density matrices with densities integrating to arbritary real numbers, and the exact functional predicts that the energy $E(N)$ follows a straight line between integer points [35]. However, due to self-interaction, the approximate functionals predict a smooth, convex form. Hartree-Fock theory is wrong in the opposite direction and predicts a concave dependence on the electron number.

systems, while many GGA functionals employ fits to reference data, limiting their applicability. PBE is usually chosen as the underlying functional of the DFTB formalism, to be introduced in a later section, and thus of particular relevance for the work in this thesis. However, introducing the technical details would exceed the scope of a short introduction, and details can be found in the literature.

Hybrid functionals

Both LDA and GGA functionals suffer from the self-interaction error. They fail to fully remove the interaction of electrons with themselves, or others with the same spin according to the exclusion principle, from the energy contribution. Consequences of this are, for instance, severely underestimated band or HOMO-LUMO gaps, and artificial electron delocalization. LDA and GGA functionals are local in the sense that the energy is the integral over functions of the density at certain points, independent of all other spatial locations. Some minor non-locality is introduced in GGA through the gradient information, but this first order expansion cannot account for interactions over larger distances. The exchange-term in Hartree-Fock theory (HF) on the other hand cancels the self-interaction exactly, but since it is calculated as an integral

over two spatial coordinates, it is non-local. Hybrid functionals take the approach to mix HF exchange $E_{\mathrm{x}}^{\mathrm{HF}}$ with GGA exchange-correlation functionals. The energy then reads:

$$E_{\mathrm{xc}}^{\mathrm{Hyb}}[\phi_1,...] = \alpha E_{\mathrm{x}}^{\mathrm{HF}}[\phi_1,...] + (1-\alpha)E_{\mathrm{x}}[\rho] + E_{\mathrm{c}}[\rho]. \tag{2.18}$$

The amount of HF exchange can be controlled through the parameter α, and different functionals use different values. Performance can also be improved by fine-tuning α for the system under investigation. For example, the PBE0 [36, 37] hybrid functional includes a fraction of $\alpha = 0.25$ HF exchange. The extremely popular B3LYP [38–40] functionals included $\alpha = 0.2$ of HF exchange, but as two additional mixing parameters.

The HF exchange term

$$E_{\mathrm{x}}^{\mathrm{HF}}[\phi_1,...] = -\frac{1}{2}\sum_{i,j}\int d^3r d^3r' \frac{\phi_i^*(\mathbf{r})\phi_j^*(\mathbf{r})\phi_i(\mathbf{r}')\phi_j(\mathbf{r}')}{|\mathbf{r}-\mathbf{r}'|} \tag{2.19}$$

depends explicitly on the individual Kohn-Sham orbitals ϕ_i, not merely on the density ρ. Consequently, the entire functional becomes orbital dependent. Because the evaluation of the HF exchange integral scales quartic with system size, DFT with hybrid functionals scales one order worse than with LDA or GGA functionals. Although in practice distance cut-offs for integrals often allow cubic scaling, hybrid functionals remain somewhat more computationally expensive.

Long-range corrected functionals

Above introduced self-interaction error is particularly severe for interactions over long distances on the scale of molecules. Indeed, with LDA or GGA functionals exchange contributions to the Kohn-Sham potential fall off very quickly:

$$V_{\mathrm{x}}(\mathbf{r},\mathbf{r}') = \frac{\delta E_{\mathrm{x}}[\rho(\mathbf{r})]}{\delta\rho(\mathbf{r}')} \sim e^{-C|\mathbf{r}-\mathbf{r}'|} \tag{2.20}$$

for $|\mathbf{r}-\mathbf{r}'| \to \infty$, with some real constant $C > 0$. However, one can exactly derive the scaling of the true exchange-correlation potential [41]:

$$V_{\mathrm{x}}(\mathbf{r},\mathbf{r}') \sim -\frac{1}{|\mathbf{r}-\mathbf{r}'|} \tag{2.21}$$

for $|\mathbf{r}-\mathbf{r}'| \to \infty$, which is falling off much slower than exponentially. In addition to a rigorous proof, there is a simple intuitive interpretation of this behavior. Imagine evaluating the Kohn-Sham potential at a point far removed from the bulk of the charge density constrained around the molecule. Since the potential is an effective single particle potential, that corresponds to a situation where one particle, namely the one on which the potential acts upon, is removed from

the molecule. Hence, there should be a single positive net charge left. At long distances, the interaction of the positive charge and the removed electron is then dominated by the monopole term, leading to specified form. While LDA and GGA exchange functionals fail to reproduce the correct scaling, the HF exchange term, on the other hand, gives rise to precisely the desired $1/r$ behavior, so that the HF exchange description is asymptotically exact. While hybrid functionals at least contain such a term, it is scaled down, and therefore too small. The incorrect long-range behavior can lead to serious errors and the complete breakdown of DFT. Perhaps most notoriously, DFT with GGA functionals in its time-dependent extension completely fails to describe charge transfer excitations. It also poorly describes spatially extended states, for example in conjugated π-systems. Both problems are very relevant for charge and energy transport applications and, therefore, for the work in this thesis. Both problems can be solved with long-range corrected functionals, whose inclusion in the approximate TD-DFTB method is introduced in a later chapter of this thesis. Long-range corrected functionals exploit the correct asymptotical scaling of HF exchange by partitioning the Coulomb interaction into a long and a short range part:

$$\frac{1}{r} = \overbrace{\frac{f(r)}{r}}^{\text{short range}} + \overbrace{\frac{1-f(r)}{r}}^{\text{long range}}. \tag{2.22}$$

The smooth function $f(r)$ switches between long and short range, i.e. $f(0) = 1$, $f'(r) < 0$, and $f(r) \to 0$ for $r \to \infty$. The error function $\text{erf}(r) = \frac{2}{\sqrt{\pi}} \int_0^r e^{-x^2} dx$ is most commonly employed $f(r) = 1 - \text{erf}(r)$, but other choices are possible as well. For the long-range corrected functionals in DFTB that will be introduced later on the exponential function is chosen for practical reasons $f(r) = e^{-r}$. Now, short and long range energy contribution are approximated separately:

$$E_{\text{x}}[\phi_1, ...] = E_{\text{x}}^{\text{sr}}[\rho] + E_x^{\text{lr,HF}}[\phi_1, ...], \tag{2.23}$$

where GGA, or alternatively hybrid, functionals are used for the short range part, and full HF exchange for the long range part:

$$E_x^{\text{lr,HF}}[\phi_1, ...], = -\frac{1}{2} \sum_{i,j} \int d^3r d^3r' \frac{\phi_i^*(\mathbf{r})\phi_j^*(\mathbf{r})(1 - f(|\mathbf{r} - \mathbf{r}'|))\phi_i(\mathbf{r}')\phi_j(\mathbf{r}')}{|\mathbf{r} - \mathbf{r}'|}. \tag{2.24}$$

Besides the correct description of charge transfer excitations and spatially extended states, long-range correction also improves the prediction of other properties, such as response properties [42–44], like the electronic polarizability, and photoemission spectra [45]. Another very useful improvement for charge and energy transport is the improved description of bond length alternations in conjugated polymers [46]. This is relevant, because the alternation strongly affects molecular relaxation energies, which in turn sensitively influence transport.

Time-dependent DFT

Although the Hohenberg-Kohn formalism does in principle establish a connection between the ground state density and the Hamiltonian, and thus with both excited states and any time evolution of the system, the variational principle only yields an equation for the ground state. Runge and Gross have laid the solid foundations for a full time-dependent extension of DFT (TD-DFT). Like the Hohenberg-Kohn theorems, there are two Runge-Gross theorems:

- *There is a one-to-one correspondence, to within a constant shift, between the time-dependent electron density $\rho(\mathbf{r},t)$ and the external time-dependent potential $V_{ext}(\mathbf{r},t)$ leading to the time-evolution of $\rho(\mathbf{r},t)$.* Through the external potential ρ determines the entire time-dependent Hamiltonian $H(t)$ and, by extension, the time-dependent wavefunction $|\psi(t)\rangle = |\psi[\rho](t)\rangle$.

- *The action*

$$A[\rho] = \int_{t_0}^{t_1} dt \, \langle \psi[\rho](t)|i\partial_t - H(t)|\psi[\rho](t)\rangle \tag{2.25}$$

  is stationary at the true density $\rho(\mathbf{r},t)$. This second theorem yields an equation of motion through the variational Euler equation

$$\frac{\delta A[\rho]}{\delta \rho} = 0. \tag{2.26}$$

Introducing time-dependent Kohn-Sham orbitals $|\phi_i(t)\rangle$ with $\rho(\mathbf{r},t) = \sum_i \langle \psi_i(t)|\mathbf{r}\rangle$ and carrying out the variation in eq. 2.26, one finds the the time-dependent Kohn-Sham equations:

$$i\partial_t|\phi_i(t)\rangle = \left(\frac{\mathbf{p}^2}{2} + V_{\text{ext}}(\mathbf{r},t) + \int d^3r' \frac{\rho(\mathbf{r}',t)}{|\mathbf{r}-\mathbf{r}'|} + V_{\text{xc}}(\mathbf{r},t) \right) |\phi_i(t)\rangle. \tag{2.27}$$

Again as in the ground state formalism, after introducing Kohn-Sham orbitals effective single particle equations result, connected by the density. The exchange-correlation potential $V_{\text{xc}} = \frac{\delta A_{\text{xc}}}{\delta \rho}$ results from the exchange-correlation action A_{xc}, which is the difference between the full action and the known kinetic and Coulomb terms. Commonly, the so called adiabatic approximation is employed, greatly simplifying the problem:

$$A_{\text{xc}}[\rho] = \int_{t_0}^{t_1} dt \, E_{\text{xc}}[\rho(t)], \tag{2.28}$$

where E_{xc} is the time-independent Kohn-Sham exchange-correlation functional. Then,

$$V_{\text{xc}}(\mathbf{r},t) = \frac{\delta E_{\text{xc}}[\rho(t)]}{\delta \rho(\mathbf{r},t)} = V_{\text{xc}}[\rho(t)](\mathbf{r}), \tag{2.29}$$

with the time-independent Kohn-Sham potential $V_{xc}[\rho]$. That is, within the adiabatic approximation the time-dependent density is simply inserted into the time-independent exchange-correlation functional. In doing so, memory effects are ignored. The approximation works well in many cases, although many failures are known too (see e.g. Refs. [47, 48]). Extensions beyond the adiabatic approximation exist and are the topic of ongoing development [49].

Time-dependent DFT is an effective method for the simulation of time-dependent quantum mechanical processes in molecules and solids. For example, it provides a theoretical foundation for the charge transfer simulations introduced in the next chapter of this thesis. However, it finds its most widespread use indirectly in the calculation of excited state properties that will be discussed in the next section.

Linear-response TD-DFT

The time evolution of an electronic system contains information about its energy spectrum. Applying a broad-band laser pulse to a system, the density response will show peaks at certain frequencies ω that are related to electronic excitations of energy $\hbar\omega$. This is the fundamental principle of spectroscopy, where the response peaks appear as absorption or emission peaks. The same principle can be exploited to calculate excitations within the framework of TD-DFT: apply an external pulse $V_{ext}(\mathbf{r},t) = \delta(t)$, which has the maximal band-width, propagate the time-dependent Kohn-Sham equations to determine the time-dependent density $\rho(\mathbf{r},t)$, and finally calculate the frequency spectrum of the density autocorrelation function $\int d^3r \rho(\mathbf{r},t)\rho(\mathbf{r},0)$. Then, the peaks in the correlation function reflect the energy spectrum.

An alternative approach to extract excited state information from the time evolution equations that is based on the same principle, but bypasses propagation in time, has been developed by Casida [50]. Casida's method is in fact so popular that it has become mostly synonymous with the term TD-DFT. Usually, TD-DFT is meant to refer to excited state calculations within Casida's framework, rather than real time propagation. The same language is also used in this thesis. In Casida's scheme, rather than to calculate a full solution to the time-dependent Kohn-Sham equations, only the linear response to an external perturbation $\delta V_{ext}(t) \sim e^{i\omega t}$ is calculated. The response function $\chi(\omega)$ exhibits singularities at the excitation frequencies. Solving for those singularities yields the desired excitation energies. In fact, many other excited state properties can be extracted from first order perturbation calculations as well [51]. Given that an entire chapter of this thesis is concerned with an extension of linear response TD-DFTB, in the following we will derive the central equations for excitation from closed shell ground states, following Casida [50].

Let $\delta V_{ext}(\mathbf{r},t)$ be a small external potential, added on top of the nuclear electrostatic potential. The perturbing potential will cause perturbations $\delta\rho_\sigma$ in the spin resolved density, and δH^σ in the Kohn-Sham Hamiltonian, with the spin index σ. The spin index has been added to the

Hamiltonian because the perturbation is spin dependent. The perturbation in the Hamiltonian consists of the external potential δV_{ext}, and a response δV_{hxc} in the Coulomb and exchange-correlation part due to the density response $\delta\rho$:

$$\delta H^\sigma = \delta V_{\text{ext}} + \delta V_{\text{hxc}}^\sigma. \tag{2.30}$$

Within linear response, $\delta\rho$ is assumed to be proportional to δV_{ext}:

$$\delta\rho_\sigma(\mathbf{r},t) = \sum_\tau \int d^3 r' \int dt' \, \chi^{\sigma\tau}(\mathbf{r},t;\mathbf{r}',t')\delta V_{\text{ext}}(\mathbf{r}',t'), \tag{2.31}$$

with the linear response function $\chi^{\sigma,\tau}(\mathbf{r},t;\mathbf{r}',t')$. The potential response is in turn brought about by the density response and to linear order we have:

$$\delta V_{\text{hxc}}^\sigma(\mathbf{r},t) = \sum_\tau \int d^3 r' \int dt' \, f_{\text{hxc}}^{\sigma\tau}(\mathbf{r},t;\mathbf{r}',t')\delta\rho_\tau(\mathbf{r}',t'). \tag{2.32}$$

The response function $f_{\text{hxc}}^{\sigma\tau}(\mathbf{r},t;\mathbf{r}',t')$ must by definition coincide with the first variation of the Kohn-Sham potential, which is the second variation of the energy functional:

$$
\begin{aligned}
f_{\text{hxc}}^{\sigma\tau}(\mathbf{r}',t';\mathbf{r},t) &= \frac{\delta\left(\int d^3 r'' \frac{\rho_\uparrow(r'',t')+\rho_\downarrow(r'',t')}{|\mathbf{r}'-\mathbf{r}''|} + V_{\text{xc}}^\sigma[\rho_\uparrow(\mathbf{r}',t'),\rho_\downarrow(\mathbf{r}',t')]\right)}{\delta\rho_\tau(\mathbf{r},t)} \\
&= \delta(t-t')\left(\frac{1}{|\mathbf{r}-\mathbf{r}'|} + \frac{\delta V_{\text{xc}}^\sigma[\rho_\uparrow(\mathbf{r}',t),\rho_\downarrow(\mathbf{r}',t)]}{\delta\rho_\tau(\mathbf{r},t)}\right).
\end{aligned}
\tag{2.33}
$$

Finally, we introduce the response function $\chi_{\text{KS}}^{\sigma\tau}(\mathbf{r},t;\mathbf{r}',t')$ with respect to changes in the Kohn-Sham Hamiltonian, which we call the Kohn-Sham susceptibility:

$$\delta\rho_\sigma(\mathbf{r},t) = \sum_\tau \int d^3 r' \int dt' \, \chi_{\text{KS}}^{\sigma\tau}(\mathbf{r},t;\mathbf{r}',t')\delta H^\tau(\mathbf{r}',t'). \tag{2.34}$$

Now, substituting eq. 2.30 into eq. 2.34 and equating eqs. 2.32 and 2.34 relates the different response functions:

$$
\begin{aligned}
\chi^{\sigma\tau}(\mathbf{r},t) =& \chi_{\text{KS}}^{\sigma\tau}(\mathbf{r},t;\mathbf{r}',t') \\
&+ \sum_{\sigma'',\tau''} \int d^3 r'' d^3 r''' \int dt'' dt''' \, \chi_{\text{KS}}^{\sigma\sigma''}(\mathbf{r},t;\mathbf{r}'',t'')f_{\text{hxc}}^{\sigma''\tau''}(\mathbf{r}'',t'';\mathbf{r}''',t''')\chi^{\tau''\tau}(\mathbf{r}''',t''';\mathbf{r}',t').
\end{aligned}
\tag{2.35}
$$

This equation states that the linear response of the system is given by the density fluctuation directly due to the external perturbation, the first term on the right hand side, and a response to the change in potential caused by said change in density, the second term on the right. χ_{KS} can

therefore be interpreted as the response of a non-interacting system because without interactions the second term vanishes. It can be readily computed by time-dependent perturbation theory, so that the central problem of TD-DFT becomes to solve eq. 2.35 for the poles of χ. The calculation can be greatly simplified by a change of representation. First, we choose to work with the expansion coefficients P_{st}^{σ} of the one-particle density matrix Γ in the basis of Kohn-Sham orbitals. In the ground state $\Gamma = \sum_{i,\sigma} |\psi_i^{\sigma}\rangle\langle\psi_i^{\sigma}|$, where the sum runs over occupied orbitals, but for the time-dependent case more generally $\Gamma = \sum_{s,t,\sigma} P_{st}^{\sigma} |\psi_s^{\sigma}\rangle\langle\psi_t^{\sigma}|$, where s,t run over all Kohn-Sham orbitals. Then, $\delta\rho_{\sigma}(\mathbf{r},t) = \sum_{s,t} \delta P_{st}^{\sigma}(t)\psi_s(\mathbf{r})\psi_t(\mathbf{r})$ and $\delta H^{\sigma}(\mathbf{r},t) = \sum_{s,t} P_{st}^{\sigma}(t)\langle\psi_s^{\sigma}|\delta H|\psi_t^{\sigma}\rangle\psi_s(\mathbf{r})\psi_t(\mathbf{r}) = \sum_{s,t} P_{st}^{\sigma}(t)\delta H_{st}^{\sigma}\psi_s(\mathbf{r})\psi_t(\mathbf{r})$. Second, we move to frequency space, rather than working in time, by Fourier transformation. Thus, integrals over the time domain are turned into sums. Eq. 2.34 becomes

$$\delta P_{st}^{\sigma}(\omega) = \sum_{u,v,\tau} \chi_{st\sigma,uv\tau}^{\mathrm{KS}} \delta H_{uv\sigma}(\omega), \tag{2.36}$$

with frequency ω. $\chi^{\mathrm{KS}}(\omega)$ can be calculated from first order perturbation theory as [50]

$$\chi_{st\sigma,uv\tau}^{\mathrm{KS}} = \delta_{us}\delta_{vt}\delta_{\tau\sigma}\frac{f_{s\sigma} - f_{t\sigma}}{\omega_{st} - \omega}, \tag{2.37}$$

where $f_{s\sigma}$ is the ground state occupation of Kohn-Sham orbital s with spin σ and $\omega_{st} = \varepsilon_{s\sigma} - \varepsilon_{t\sigma}$, with the Kohn-Sham orbital eigenvalues $\varepsilon_{s\sigma}$. For a closed shell system f can be either 1 (occupied) or 0 (unoccupied). Therefore, χ_{KS} differs from zero only for transitions from occupied to unoccupied orbitals. Let $i,j,...$ label occupied orbitals and $a,b,...$ unoccupied, or virtual, orbitals. With this notation, only density matrix coefficients δP_{ia} and δP_{ai} do not vanish. One customarily writes

$$\begin{aligned} \delta P_{ia}^{\sigma}(\omega) &= X_{ia}^{\sigma}(\omega) \\ \delta P_{ai}^{\sigma}(\omega) &= Y_{ia}^{\sigma}(\omega), \end{aligned} \tag{2.38}$$

and $\delta\rho$ must take the form

$$\delta\rho_{\sigma}(\mathbf{r},\omega) = \sum_{i,a} (X_{ia}^{\sigma}(\omega)\psi_i(\mathbf{r})\psi_a(\mathbf{r}) + Y_{ia}^{\sigma}(\omega)\psi_a(\mathbf{r})\psi_i(\mathbf{r})). \tag{2.39}$$

Likewise, the potential response δV_{hxc} takes the form

$$\begin{aligned} \delta V_{ia\sigma}^{\mathrm{hxc}}(\omega) &= \sum_{u,v,\tau} K_{ia\sigma,uv\tau}\delta P_{uv}^{\tau}(\omega) \\ &= \sum_{j,b,\tau} \left(K_{ia\sigma,jb\tau}X_{jb}^{\tau}(\omega) + K_{ia\sigma,bj\tau}Y_{jb}^{\tau}(\omega) \right), \end{aligned} \tag{2.40}$$

with the response kernel K that is the matrix representation of f_{hxc}:

$$
\begin{aligned}
K_{ia\sigma,jb\tau} &= \int d^3r \, d^3r' \, \psi_{i\sigma}(\mathbf{r}) \psi_{a\sigma}(\mathbf{r}) f_{\text{hxc}}^{\sigma\tau}(\mathbf{r},\mathbf{r}') \psi_{j\tau}(\mathbf{r}') \psi_{b\tau}(\mathbf{r}') \\
&= \frac{\partial H_{ia}^{\sigma}}{\partial P_{jb}^{\tau}},
\end{aligned}
\tag{2.41}
$$

with the Kohn-Sham Hamiltonian H_{ia}^{σ}. Notice how K is symmetric under exchange of indices j, b: $K_{ia\sigma,jb\tau} = K_{ia\sigma,bj\tau}$. This is because K contains only density functional terms and will allow simplifications of the final equations, resulting in the so-called Casida equation. For hybrid or long-range corrected functionals an extra exchange term would be present that violates the symmetry, requiring a different working equation, an issue to be addressed in the chapter on long-range corrected DFTB. Finally, using eqs. 2.30, 2.40, and 2.36 we find:

$$
\left(\begin{pmatrix} \mathbf{A} & \mathbf{B} \\ \mathbf{B} & \mathbf{A} \end{pmatrix} - \omega \begin{pmatrix} \mathbb{1} & 0 \\ 0 & -\mathbb{1} \end{pmatrix} \right) \begin{pmatrix} \mathbf{X} \\ \mathbf{Y} \end{pmatrix} = \delta V_{\text{ext}}(\omega),
\tag{2.42}
$$

where much simplifying notation was introduced. $\mathbf{X} = (X_{ia}^{\sigma})_{i,a,\sigma}$ and $\mathbf{Y} = (Y_{ia}^{\sigma})_{i,a,\sigma}$ are serialized versions of the response density matrix coefficients, and the matrices $\mathbf{A}$, $\mathbf{B}$ are given by

$$
A_{ia\sigma,jb\tau} = \delta_{ij}\delta_{ab}\delta_{\sigma\tau} + K_{ia\sigma,jb\tau},
\tag{2.43}
$$

and

$$
B_{ia\sigma,jb\tau} = K_{ia\sigma,jb\tau}.
\tag{2.44}
$$

The response must be infinite when the frequency hits excitation energies Ω. Therefore, the matrix factor on the right has to vanish and we arrive at the eigenvalue problem

$$
\begin{pmatrix} \mathbf{A} & \mathbf{B} \\ \mathbf{B} & \mathbf{A} \end{pmatrix} \begin{pmatrix} \mathbf{X_I} \\ \mathbf{Y_I} \end{pmatrix} = \Omega_I \begin{pmatrix} \mathbb{1} & 0 \\ 0 & -\mathbb{1} \end{pmatrix} \begin{pmatrix} \mathbf{X_I} \\ \mathbf{Y_I} \end{pmatrix}.
\tag{2.45}
$$

The molecular excitation energies are give by the solutions ω_I of this equation, which therefore constitutes the fundamental problem of linear response TD-DFT. Because it shares the mathematical form of the equations of time-dependent Hartree-Fock theory, it is also known as the Random-Phase-Approximation, or RPA, equation. The dimensionality can be halved by deriving the following expression from eq. 2.45:

$$
(\mathbf{A} - \mathbf{B})(\mathbf{A} + \mathbf{B})(\mathbf{X}_I + \mathbf{Y}_I) = \omega^2(\mathbf{X}_I + \mathbf{Y}_I),
\tag{2.46}
$$

which is another eigenvalue problem in a lower dimensional space. Recall that for LDA and GGA functionals $K_{ia\sigma,jb\tau} = K_{ia\sigma,bj\tau}$. Hence, $\mathbf{A} - \mathbf{B}$ is diagonal and positive definite, allowing for yet another transformation of the RPA equations:

$$(\mathbf{A} - \mathbf{B})^{\frac{1}{2}}(\mathbf{A} + \mathbf{B})(\mathbf{A} - \mathbf{B})^{\frac{1}{2}}\mathbf{F}_I = \omega^2 \mathbf{F}_i, \qquad (2.47)$$

and

$$\mathbf{F}_I = (\mathbf{A} - \mathbf{B})^{-\frac{1}{2}}(\mathbf{X}_I + \mathbf{Y}_I). \qquad (2.48)$$

Because $\mathbf{A} - \mathbf{B}$ is diagonal, evaluation of the matrix square root is trivial. Eq. 2.47 is an Hermitian eigenvalue problem and the equation of choice when there are no exchange terms. It is known as the Casida equation.

2.1.3 The density functional tight-binding method

Albeit DFT is already computationally very efficient compared to most wavefunction based electronic structure methods, there remain many problems that require quantum treatment, but at much lower computational cost. For instance, such problems include simulations of large nanostructures that can contain many thousands of atoms. Given the large and growing importance of nanotechnology, this is of considerable practical relevance, say in the development process of new integrated circuits or molecular motors. Another field in need of fast computation are all sorts of dynamical simulations, stretching from single molecular electronic dynamics for spectroscopy to the simulation of chemical reactions at the active sites of proteins in aqueous solution. There, the relevant time scales can be on the order of nanoseconds, requiring millions of quantum calculations, well beyond the scope of DFT. For such purposes, semi-empirical and approximate methods exist that are far less computationally expensive at the cost of some accuracy. Many of those methods rely strongly on fitting of parameters to reference data, severely limiting their transferability. The density functional tight-binding method (DFTB), on the other hand, is derived and largely parametrized from DFT, lending it a certain robustness. It tends to perform particularly well for organic molecules, as the underlying assumptions are usually satisfied, providing a kind of rigorous foundation that many empirical methods lack. As such molecules are the target systems for the studies presented in this work, we opted for DFTB as the underlying method for further development. DFTB does, however, inherit the shortcomings of the applied density functional approximations. This will be addressed in a later chapter. In this section, we derive and explain the basics of DFTB, discuss its time-dependent extension TD-DFTB, and introduce a recent extension to include long-range corrected functionals.

Derivation

DFTB [52, 53] can be derived from DFT through a series expansion of the DFT energy functional $E[\rho]$ at a reference density ρ_0. Here we expand up to quadratic order, leading to the so-called SCC-DFTB, or DFTB2, method [53] that is the version most commonly used. Early versions only contained first order terms (DFTB1 [52]), and extensions with third order terms (DFTB3 [54]) exist as well. Starting from the energy expression

$$E[\rho] = \sum_i f_i \langle \phi_i | \frac{\mathbf{p}^2}{2} + \int d^3 r' \frac{\rho(\mathbf{r}')}{|\mathbf{r} - \mathbf{r}'|} + V_{\text{ext}}(\mathbf{r}) | \phi_i \rangle + E_{\text{xc}}[\rho] + E_{\text{nuc}}, \qquad (2.49)$$

which is a different way to write eq. 2.10, with Kohn-Sham orbitals $|\phi_i\rangle$, orbital occupations f_i, and the internuclear repulsion $E_{\text{nuc}} = \sum_{A,B} \frac{Z_A Z_B}{|\mathbf{R}_A - \mathbf{R}_B|}$, we expand

$$\begin{aligned} E[\rho] = &\sum_i f_i \langle \phi_i | \frac{1}{2} \mathbf{p}^2 + \int d^3 r' \frac{\rho_0(\mathbf{r}')}{|\mathbf{r} - \mathbf{r}'|} + \frac{\delta E_{\text{xc}}[\rho_0]}{\delta \rho(\mathbf{r})} + V_{\text{ext}}(\mathbf{r}) | \phi_i \rangle \\ &+ \frac{1}{2} \int d^3 r d^3 r' \left(\frac{1}{|\mathbf{r} - \mathbf{r}'|} + \frac{\delta^2 E_{\text{xc}}[\rho_0]}{\delta \rho(\mathbf{r}) \delta \rho(\mathbf{r}')} \right) \delta \rho(\mathbf{r}) \delta \rho(\mathbf{r}') \\ &+ E_{\text{xc}}[\rho_0] + E_{\text{nuc}} - \frac{1}{2} \int d^3 r d^3 r' \frac{\rho_0(\mathbf{r}) \rho_0(\mathbf{r}')}{|\mathbf{r} - \mathbf{r}'|} - \int d^3 r \frac{\delta E_{\text{xc}}[\rho_0]}{\delta \rho(\mathbf{r})} \rho_0(\mathbf{r}) \\ &+ O(\delta \rho^3), \end{aligned} \qquad (2.50)$$

with density fluctuations $\delta \rho$ and the reference density ρ_0 such that $\rho = \rho_0 + \delta \rho$. Now, we group together different terms that will then be further approximated. The first order terms are:

$$\begin{aligned} E^{(1)} &= \sum_i f_i \langle \phi_i | \frac{1}{2} \mathbf{p}^2 + \int d^3 r' \frac{\rho_0(\mathbf{r}')}{|\mathbf{r} - \mathbf{r}'|} + \frac{\delta E_{\text{xc}}[\rho_0]}{\delta \rho(\mathbf{r})} + V_{\text{ext}}(\mathbf{r}) | \phi_i \rangle \\ &= \sum_i f_i \langle \phi_i | H^{(0)}[\rho_0] | \phi_i \rangle, \end{aligned} \qquad (2.51)$$

with the zeroth order Hamiltonian $H^{(0)}$ that depends only on the reference density. The second order terms are given by the Coulomb integral:

$$E^{(2)} = \frac{1}{2} \int d^3 r d^3 r' \left(\frac{1}{|\mathbf{r} - \mathbf{r}'|} + \frac{\delta^2 E_{\text{xc}}[\rho_0]}{\delta \rho(\mathbf{r}) \delta \rho(\mathbf{r}')} \right) \delta \rho(\mathbf{r}) \delta \rho(\mathbf{r}'). \qquad (2.52)$$

Finally, there are zeroth order terms that depend only on the reference density ρ_0 and the nuclear positions:

$$E^{(3)} = E_{\text{xc}}[\rho_0] + E_{\text{nuc}} - \frac{1}{2} \int d^3 r d^3 r' \frac{\rho_0(\mathbf{r}) \rho_0(\mathbf{r}')}{|\mathbf{r} - \mathbf{r}'|} - \int d^3 r \frac{\delta E_{\text{xc}}[\rho_0]}{\delta \rho(\mathbf{r})} \rho_0(\mathbf{r}). \qquad (2.53)$$

All three energy contributions will now be further approximated, after an atom centered basis representation has been introduced:

$$|\phi_i\rangle = \sum_{A,\mu \in A} c_{\mu i} |\chi_\mu\rangle, \tag{2.54}$$

where the upper case Latin index A runs over atoms, Greek index μ over basis functions, and $\mu \in A$ indicates that orbital μ is centered on atom A: $\langle \mathbf{r} | \chi_\mu \rangle = \chi(\mathbf{r} - \mathbf{R}_A)$ for some orbital function χ. The detailed construction of the basis will be discussed later on. Likewise, the reference density ρ_0 is constructed as a sum of atomic densities ρ_A, also centered on the atoms:

$$\rho_0(\mathbf{r}) = \sum_A \rho_A(r). \tag{2.55}$$

It is the fundamental assumption underpinning DFTB that the molecular density ρ is already well described by such a sum of atomic densities, with only modest charge transfer $\delta\rho$. Hence comes the term tight-binding. Within the basis, $E^{(1)}$ can be expanded out as:

$$E^{(1)} = \sum_i \sum_{A,B} \sum_{\mu \in A, \nu \in B} f_i c_{\mu i} c_{\nu i} \langle \chi_m u | H^{(0)}[\rho_0] | \chi_\nu \rangle = \sum_i \sum_{A,B} \sum_{\mu \in A, \nu \in B} f_i c_{\mu i} c_{\nu i} H^{(0)}[\rho_0]_{\mu\nu}. \tag{2.56}$$

In principle, $H^{(0)}[\rho_0]_{\mu\nu}$ depends on the positions of all nuclei. However, the integral is dominated by the density contributions coming from the two atoms on which χ_μ and χ_ν are centered. Hence, we can approximate:

$$H^{(0)}[\rho_0]_{\mu\nu} \approx H^{(0)}[\rho_A + \rho_B]_{\mu\nu} = H^{(0)}_{\mu\nu} \qquad \text{for } \mu \in A \text{ and } \nu \in B, \tag{2.57}$$

where $H^{(0)}_{\mu\nu}$ depends only on the relative positions of atoms A and B, allowing for precalculation. Thus, because $H^{(0)}_{\mu\nu}$ is stored, no integral needs to be evaluated at run-time. As shall be discussed later on, due to symmetry only one rather than three coordinates have to be sampled, reducing memory requirements to a minimum. For $\mu = \nu$ the Hamiltonian element coincides with an orbital eigenvalue of an isolated atom $H^{(0)}_{\mu\mu} = \varepsilon_\mu$. In order to approximate the second order terms $E^{(2)}$, we shall partition the space into disjoint regions V_A of space closest to atom A, such that $\mathbb{R}^3 = \bigcup_A V_A$, and write the density fluctuations $\delta\rho(\mathbf{r})$ as a sum of atomic density fluctuations $\delta\rho(\mathbf{r}) = \sum_A \delta\rho_A(\mathbf{r})$, where $\delta\rho_A$ is non-vanishing only on V_A. Next, we define atomic charge fluctuations as $\Delta q_A = \int_{V_A} d^3r \, \delta\rho(\mathbf{r}) = \int d^3r \, \delta\rho_A(\mathbf{r})$, and express charge fluctuations as

$$\delta\rho_A(\mathbf{r}) = \Delta q_A g_A(\mathbf{r}), \tag{2.58}$$

where $g_A(\mathbf{r})$ is a shape function that must integrate to one. We assume a Gaussian shape for g_A:

$$g_A(\mathbf{r}) = \frac{1}{(2\pi\sigma_A^2)^{\frac{3}{2}}} \exp\left(-\frac{\mathbf{r}^2}{2\sigma_A^2}\right). \tag{2.59}$$

In doing so, we impose spherical symmetry on the charge fluctuations, effectively leading to a monopole approximation. Indeed, multipole expansion results in the same form. The width σ_A of the charge distribution is then the only free parameter at second order. The energy expression reads:

$$E^{(2)} = \frac{1}{2}\sum_{A,B}\Delta q_A \Delta q_B \int d^3r d^3r' \left(\frac{1}{|\mathbf{r}-\mathbf{r}'|} + \frac{\delta^2 E_{xc}[\rho_0]}{\delta\rho(\mathbf{r})\delta\rho(\mathbf{r}')}\right) g_A(\mathbf{r})g_B(\mathbf{r}'). \tag{2.60}$$

Discarding the exchange correlation term, only the Coulomb integral has to be evaluated, which is possible in closed form [53]:

$$\int d^3r d^3r' \frac{g_A(\mathbf{r})g_B(\mathbf{r})}{|\mathbf{r}-\mathbf{r}'|} = \frac{\text{erf}(C_{AB}|\mathbf{R}_A-\mathbf{R}_B|)}{|\mathbf{R}_A-\mathbf{R}_B|} = \gamma_{AB}(|\mathbf{R}_A-\mathbf{R}_B|), \tag{2.61}$$

with

$$C_{AB} = \sqrt{\frac{1}{2}\frac{1}{\sigma_A^2 + \sigma_B^2}} \tag{2.62}$$

fixed by the charge distribution widths. To fix the width parameters, we consider the expansion of the energy of a free atom A in an excess charge Δq_A:

$$E(\Delta q_A) = E(0) + \frac{dE}{dq}\Delta q_A + \frac{1}{2}\frac{d^2E}{dq^2}\Delta q_A^2 + O(\Delta q_A^3) \tag{2.63}$$

In DFT the second order term is given by the so-called Hubbard parameter U and related to the ionization potential IE and electron affinity EA as

$$\frac{d^2E}{dq^2} = U = \text{IE} - \text{EA}. \tag{2.64}$$

The Hubbard parameters can be easily determined from DFT calculations on free atoms. Then, demanding that for free atoms $E^{(2)}$ coincide with $\frac{1}{2}U\Delta q^2$ establishes a connection between the Hubbard parameter U_A of an atom and the width parameter σ_A, hence fixed. In analogy to $\Delta q_A = \int_{V_A} d^3r\,\delta\rho$, we define atomic charges q_A as

$$q_A = \int_{V_A} d^3r\,\rho(\mathbf{r}) = \sum_i f_i \int_{V_A} d^3r\,\phi_i(\mathbf{r})^2 = \sum_i f_i \sum_{\mu,\nu} c_{\mu i}c_{\nu i}\int_{V_A} d^3r\,\chi_\mu(\mathbf{r})\chi_\nu(\mathbf{r}), \tag{2.65}$$

assuming real orbitals. In the tight-binding spirit, we approximate

$$\int_{V_A} d^3r\, \chi_\mu(\mathbf{r})\chi_\nu(\mathbf{r}) \approx \frac{1}{2}\int d^3r\, \chi_\mu(\mathbf{r})\chi_\nu(\mathbf{r}) = \frac{1}{2}S_{\mu\nu},$$

or in other words, the overlap is only non-zero in the atomic regions and can be equally partitioned between both involved atoms. Then q_A simplifies to

$$q_A = \sum_i f_i \sum_{\nu,\mu\in A} c_{\mu i}c_{\nu i}S_{\mu\nu}, \tag{2.66}$$

which is the same as the famous Mulliken charge expression [55]. Δq_A can be computed as $\Delta q_A = q_A - q_A^{(0)}$ with the electronic charge $q_A^{(0)}$ of a neutral atom A. The overlap matrix $S_{\mu\nu}$ can be precalculated, like $H_{\mu\nu}^{(0)}$. Finally, the third order term $E^{(3)}$ remains to be determined. Because $E^{(3)}$ is a function of ρ_0 alone, and in turn ρ_0 is a function of the nuclear positions $\mathbf{R}_A$, $E^{(3)}$ can be written as a function of the $\mathbf{R}_A$. Since most of reference charge interactions happens between atom pairs, with three center contributions smaller, we approximate

$$E^{(3)} = \frac{1}{2}\sum_{A\neq B} V_{AB}(|\mathbf{R}_A - \mathbf{R}_B|). \tag{2.67}$$

The functions V_{AB} are called repulsive potentials. For the functional form of V_{AB} splines or polynomials are employed, where the exact choice does not matter. One function for each pair of elements is used. While in principle V_{AB} could be calculated directly from DFT, usually it is fit to reference data. Hence, empirical corrections to the tight-binding approximation are fit together with the reference as well. Reference data has to be hand-picked to generalize well, and this can be a tedious process, normally the hardest part of the fitting procedure. One part of this work is concerned with a generalization of the repulsive potentials to render the manual selection obsolete by allowing very large data sets to be used. Repulsive potentials will be discussed in more detail at this later point. Eventually, the full DFTB energy reads:

$$E = \sum_i f_i \sum_{\mu\nu} c_{\mu i}c_{\nu i}H_{\mu\nu}^{(0)} + \frac{1}{2}\sum_{AB}\Delta q_A\Delta q_B\gamma_{AB}(|\mathbf{R}_A - \mathbf{R}_B|) + \frac{1}{2}\sum_{A\neq B}V_{AB}(|\mathbf{R}_A - \mathbf{R}_B|). \tag{2.68}$$

Like in full DFT, Kohn-Sham equations follow from energy minimization, constrained to orthonormal orbitals. Thus, we have:

$$\sum_\nu \left(H_{\mu\nu}^{(0)} + \frac{1}{2}S_{\mu\nu}\sum_C(\gamma_{\mu C} + \gamma_{\nu C})\Delta q_C\right)c_{\nu i} = \varepsilon_i \sum_\nu S_{\mu\nu}c_{\nu i}, \tag{2.69}$$

where $\gamma_{\mu C} = \gamma_{AC}$ for $\mu \in A$. The equations have to be solved self-consistently in Δq_A to find the Kohn-Sham orbitals ϕ_i and the energy E. Analytic nuclear gradient expressions $\nabla_\mathbf{R}E$ are

available to calculate forces [53]. Note how the repulsive potentials only appear in the total energy expression, but not in the Kohn-Sham equations. They are important for the description of molecular geometries and absolute energies, but do not affect the electronic structure calculation.

Basis set and reference density

DFTB employs a minimal basis set for the sake of computational efficiency. However, naive minimal basis sets are not usually sufficient for quantum chemical applications because they lead to poor quantitative performance. Therefore, the basis sets used in DFTB are specially optimized. As previously noted, DFTB relies on a tight-binding assumption in which electrons are expected to be largely confined close to the atoms, what is normally the case to a good extent within molecules. In free atoms, on the other hand, electron densities tend to be more diffuse. Accordingly, orbitals coming from free atoms, such as the natural hydrogen s, p, d, ... orbitals, are not a suitable basis set choice. Instead, the basis set is taken from confined free atom orbitals, where a confinement potential $V_{\text{conf}}(\mathbf{r})$ simulates the effect of the molecular environment. More explicitly, the basis functions $\chi_\mu(\mathbf{r})$ centered on atom A are solutions to the modified Kohn-Sham eigenvalue equation

$$\left(\frac{\mathbf{p}^2}{2} + \int d^3 r' \frac{\rho_A(\mathbf{r}')}{|\mathbf{r} - \mathbf{r}'|} + \frac{\delta E_{\text{XC}}[\rho_A]}{\delta \rho(\mathbf{r})} - \frac{Z_A}{|\mathbf{r}|} + V_{\text{conf}}(\mathbf{r}) \right) \chi_\mu(\mathbf{r}) = \varepsilon_\mu \chi_\mu(\mathbf{r}). \tag{2.70}$$

The purpose of Vconf is to compress the density, and consequently V_{conf} should grow with the distance from the nucleus. The by far most common choice is a quadratic potential:

$$V_{\text{conf}}(\mathbf{r}) = \left(\frac{\mathbf{r}}{r_{\text{wf}}} \right)^2, \tag{2.71}$$

albeit some DFTB parametrization have used other potentials, too [21, 56]. The parameter r_{wf} controls the extend of the confinement. DFTB parametrizations usually fine tune r_{wf} for optimal accuracy. The atomic density ρ_A that appears in the Kohn-Sham potential is likewise determined from a self consistent constraint free atom calculation, but with a different constraint parameter r_{d}. ρ_A also serves as atom A's contribution to the reference density ρ_0. Thus, Hamiltonian elements $H_{\mu\nu}^{(0)}$ for atom pairs A and B are calculated and tabulated as $H_{\mu\nu}^{(0)} = \int d^3 r \chi_\mu(\mathbf{r}) H[\rho_A(\mathbf{r}) + \rho_B(\mathbf{r})] \chi_\nu(\mathbf{r})$. Eq. 2.70 is solved in a Slater type orbital basis, that is with exponentially decaying basis functions. Therefore, the DFTB basis is also effectively of Slater type. Because all integrals are precalculated, there is no associated computational extra cost over, say, Gaussian type functions. While the tabulated integrals $H_{\mu\nu}^{(0)}(\mathbf{R}_A - \mathbf{R}_B)$ and $S_{\mu\nu}(\mathbf{R}_A - \mathbf{R}_B)$ do, in principle, depend on three spatial coordinates, only one dimensional tables for different combinations of orbital symmetry – e.g. s-s, s-$p_{x,y,z}$, p_x-p_y, etc. – need to be stored,
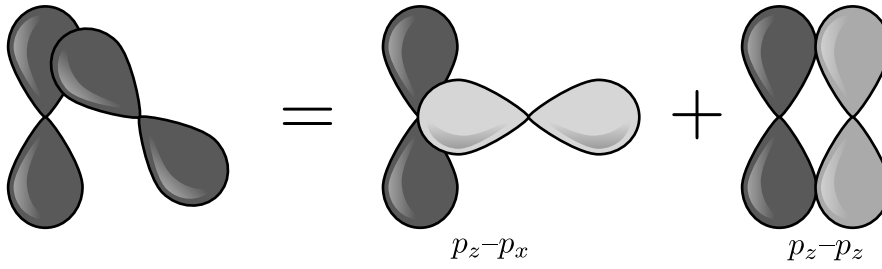
Figure 2.2: The integral involving two arbitrarily oriented *p* orbitals can be reduced to the sum of integrals over orbitals of fixed relative orientation by exploiting that *p* orbitals behave like vectors in $\mathbb{R}^3$ under rotation.

exploiting symmetry and the behavior of the spherical harmonics under rotation. See Fig. 2.2 for a visual explanation.

Long-range corrected DFTB

As introduced earlier, long-range corrected DFT functionals treat exchange at far distances at the Hartree-Fock level and improve the description in many cases that are particularly relevant for this thesis. The traditional DFTB formalism cannot be parametrized from such functionals because it includes no exact exchange terms, nor are there expressions for screened integrals. Therefore, Lutsker and Niehaus extended the formalism to permit long-range corrected functionals [17, 57] (LC-DFTB). This formalism provides the foundation on which the extension of TD-DFTB to long-range corrected functionals (LC-TD-DFTB), one of the developments introduced in this thesis, rests. That merits a thorough introduction to LC-DFTB. First, we move from a representation in terms of orbital coefficients $c_{\mu i}$ and Mulliken charges q_A to one in terms of one-particle density matrix coefficients $P_{\mu\nu} = \sum_i f_i c_{\mu i} c_{\nu i}$, with $\sum_i f_i |\phi_i\rangle\langle\phi_i| = \sum_{\mu,\nu} P_{\mu\nu} |\chi_\mu\rangle\langle\chi_\nu|$. This step will be necessary because the exchange terms depend on the entire density matrix, rather than just its trace, which are the Mulliken charges. We can then rewrite the DFTB energy expression eq. 2.68 as

$$E^{\text{sr}} = \sum_{\mu,\nu} P_{\mu\nu} H_{\mu\nu}^{(0)} + \frac{1}{8} \sum_{\mu,\nu,\alpha,\beta} \Delta P_{\mu\nu} \Delta P_{\alpha\beta} S_{\mu\nu} S_{\alpha\beta} (\gamma_{\mu\alpha} + \gamma_{\mu\beta} + \gamma_{\nu\alpha} + \gamma_{\nu\beta}) + V_{\text{rep}}, \qquad (2.72)$$

where $\gamma_{\mu\nu} = \gamma_{AB}$ for $\mu \in A$ and $\nu \in B$. The tag "sr" has been added to indicate that later these terms will entail the short range contribution. $\Delta P_{\mu\nu} = P_{\mu\nu} - P_{\mu\nu}^{(0)}$ is the deviation of the density matrix from the sum of free atom density matrices $P_{\mu\nu}^{(0)}$, where for free atoms $P_{\mu\nu}^{(0),A} = \delta_{\mu\nu} f_\mu$ with the orbital occupation f_μ. The form of the repulsive potentials V_{rep} is not affected by the extension of the formalism, and we shall be no more concerned with them in this chapter. The long-range corrected functional by Baer, Neuhauser, and Livshitz [58, 59] (BNL) underpins

LC-DFTB. In their approach, the Coulomb interactions is split up with the switching function $e^{-\omega r}$, i.e. $\frac{1}{r} = \frac{e^{-\omega r}}{r} + \frac{1-e^{-\omega r}}{r}$. The range-separation parameter ω controls the distance at which Hartree-Fock exchange is turned on. $\omega = 0$ leads to conventional DFT, $\omega \to \infty$ to Hartree-Fock theory. Short-range exchange-correlation is modeled at the GGA level for correlation and LDA for exchange:

$$E_{xc}^{\omega,\text{DFT}} = E_c^{\text{GGA}} + E_x^{\omega,\text{LDA}}. \tag{2.73}$$

The suffix ω on the LDA energy indicates that it is evaluated for the screened, or Yukawa, interaction, which is possible analytically, while full GGA correlation is included for lack of a long-range correlation term. For LC-DFTB PBE is used as the GGA functional. Remember that, with all long-range corrected functionals, long-range exchange is exactly accounted for by a Hartree-Fock exchange term. The zeroth-order DFTB Hamiltonian $H^{(0)}$ is then calculated with the BNL functional, fixing the terms in E^{sr}. On top of the functional energy long-range exchange

$$\frac{1}{2} \sum_{i,j} \int d^3 r d^3 r' \frac{\phi_i^*(\mathbf{r})\phi_j^*(\mathbf{r})e^{-\omega|\mathbf{r}-\mathbf{r}'|}\phi_i(\mathbf{r}')\phi_j(\mathbf{r}')}{|\mathbf{r}-\mathbf{r}'|} \tag{2.74}$$

is added. Note that the first summand in $1 - e^{-\omega r}$ went into the full-range Coulomb term. Entering this into the DFTB energy approximation, applying the Mulliken approximation $\chi_\mu(\mathbf{r})\chi_\nu(\mathbf{r}) \approx \frac{1}{2}S_{\mu\nu}(\chi_\mu(\mathbf{r})^2 + \chi_\nu(\mathbf{r})^2)$, and expanding in basis functions yields the long-range term:

$$E^{\omega,\text{lr}} = -\frac{1}{16} \sum_{\mu,\nu,\alpha,\beta} \Delta P_{\mu\nu} \Delta P_{\alpha\beta} S_{\mu\alpha} S_{\nu\beta} (\gamma_{\mu\beta}^{\text{lr}} + \gamma_{\mu\nu}^{\text{lr}} + \gamma_{\alpha\nu}^{\text{lr}} + \gamma_{\alpha\beta}^{\text{lr}}), \tag{2.75}$$

where the long-range integrals γ^{lr} appear. They are approximated in the same way as the full-range integrals, assuming charge distributions $g_A(\mathbf{r})$ around atom A:

$$\gamma_{AB}^{\text{lr}} = \int d^3 r d^3 r' \frac{g_A(\mathbf{r})e^{-\omega|\mathbf{r}-\mathbf{r}'|}g_B(\mathbf{r}')}{|\mathbf{r}-\mathbf{r}'|} \tag{2.76}$$

For the Gaussian profile the long-range integral can also be evaluated analytically, with a final form a little more complicated than for full-range [17]. The full energy is then the sum of E^{sr} and E^{lr}:

$$\begin{aligned}
E = \sum_{\mu,\nu} P_{\mu\nu} H_{\mu\nu}^{(0)} + \frac{1}{8} \sum_{\mu,\nu,\alpha,\beta} \Delta P_{\mu\nu} \Delta P_{\alpha\beta} S_{\mu\nu} S_{\alpha\beta} (\gamma_{\mu\alpha} + \gamma_{\mu\beta} + \gamma_{\nu\alpha} + \gamma_{\nu\beta}) \\
- \frac{1}{16} \sum_{\mu,\nu,\alpha,\beta} \Delta P_{\mu\nu} \Delta P_{\alpha\beta} S_{\mu\alpha} S_{\nu\beta} (\gamma_{\mu\beta}^{\text{lr}} + \gamma_{\mu\nu}^{\text{lr}} + \gamma_{\alpha\nu}^{\text{lr}} + \gamma_{\alpha\beta}^{\text{lr}}). \\
+ V_{\text{rep}}
\end{aligned} \tag{2.77}$$

Minimization of eq. 2.77 yields Kohn-Sham equations, which have to be solved self consistently. The Kohn-Sham Hamiltonian reads

$$
\begin{aligned}
H_{\mu\nu} =& H_{\mu\nu}^{(0)} + \frac{1}{4}\sum_{\alpha,\beta}\Delta P_{\alpha\beta}S_{\mu\nu}S_{\alpha\beta}(\gamma_{\mu\alpha} + \gamma_{\mu\beta} + \gamma_{\nu\alpha} + \gamma_{\nu\beta}) \\
& - \frac{1}{8}\sum_{\alpha,\beta}\Delta P_{\alpha\beta}S_{\mu\alpha}S_{\nu\beta}(\gamma_{\mu\beta}^{\mathrm{lr}} + \gamma_{\mu\nu}^{\mathrm{lr}} + \gamma_{\alpha\nu}^{\mathrm{lr}} + \gamma_{\alpha\beta}^{\mathrm{lr}}).
\end{aligned}
$$

$$(2.78)$$

A major difference compared to conventional DFTB is that consistency in the full density matrix, rather than merely in the charges is required. Another intricate point worth mentioning is that the number of terms in the sum of exchange terms scales as $O(N^4)$ with system size N, whereas conventional DFTB scales as $O(N^2)$. Hence, significantly deteriorated computational efficiency could be expected. However, in practice quadratic scaling is restored through a cut-off scheme, where the magnitude of terms is quickly checked with an easily evaluatable estimate, and negligible contributions below a threshold $\varepsilon_{\mathrm{threshold}}$ are discarded. A detailed description of the cut-off procedure can be found in the original work [17].

2.1.4 Force-fields and molecular mechanics

Even the fastest empirical quantum mechanical methods are far too slow to simulate truly large systems of ten thousands to millions of atoms, let alone on the nanosecond time scale and beyond. Yet, such large scale problems appear abundantly. Take for example the folding of proteins in solution, which is one of the preeminent subjects of biophysics and chemistry, or the description of large sections of amorphous or crystalline organic semiconducting materials that are studied in this thesis. Therefore, a faster set of methods is required to study them. The gap is filled by so-called force-field methods. The term "force-field" refers to a fit of some mathematical function $V(\mathbf{R}_1,..)$ of the nuclear coordinates $\mathbf{R}_i$ to a potential energy surface $E(\mathbf{R}_1,...)$, most of the time the ground state, disregarding the other surfaces. Because usually only a small subsection of the potential energy surface is of interest, reasonably simple functions suffice for the fit. In particular, most force-fields do not attempt to describe chemical reactions, only certain molecules. Oftentimes one addresses large scale structural questions, like the secondary structure of proteins that are not overly sensitive to the details of the potential energy surface, so that force-fields are a very adequate manner of description. Indeed, dispersion forces, crucial for the correct description of large scale and intermolecular arrangement, are poorly accounted for by DFT and other fast quantum mechanical methods, which require fitted correction terms akin to force-fields, or else would perform worse.

Force-fields

There are many different force-fields in existence that differ in what reference data they employ for fitting, and the precise functional form used. However, most share a number of basic, dominant, and physically inspired terms. Equilibrium molecular geometries are described by way of equilibrium bond lengths R_b, bond angles θ_b, and dihedral angles ω_d. A series expansion to second order for bonds, and a Fourier expansion for the periodic dihedrals then yields the energetic costs of molecular perturbations. The corresponding bonded terms now read:

$$V_{\text{bond}} = \sum_b \frac{1}{2} k_b (|\mathbf{R}^{(b)}| - R_b)^2, \tag{2.79}$$

$$V_{\text{angle}} = \sum_b \frac{1}{2} k_{\theta b} (\theta^{(b)} - \theta_b)^2, \tag{2.80}$$

and

$$V_{\text{dihedral}} = \sum_d \sum_{n=0}^{N_d} V_{dn} (1 + \cos(n\omega_{dn} - \omega^{(d)})), \tag{2.81}$$

where $\mathbf{R}^{(b)}$, $\theta^{(b)}$, and $\omega^{(d)}$ are the bond lengths and angles, and dihedral angles, calculated at the current geometry, respectively. Non-bonded interactions consist of two contributions: electrostatic Coulomb interaction of atom centered charges q_i and van-der-Waals interaction. The former accounts for charge transfer within molecules or molecular fragments. The associated potential reads:

$$V_{\text{electrostatic}} = \frac{1}{2} \sum_{i \neq j} \frac{q_i q_j}{|\mathbf{R}_i - \mathbf{R}_j|}, \tag{2.82}$$

where i, j run over all atoms. The later entails short-range Pauli repulsion and dispersion interaction. Usually, the potential is approximated as

$$V_{\text{van-der-Waals}} = \frac{1}{2} \sum_{i \neq j} 4\varepsilon_{ij} \left(\left(\frac{\sigma_{ij}}{R_{ij}} \right)^{12} - \left(\frac{\sigma_{ij}}{R_{ij}} \right)^6 \right), \tag{2.83}$$

with interatomic distances R_{ij} and parameters $\varepsilon_{ij}, \sigma_{ij}$. The first summand belongs to Pauli repulsion, and its form is purely empirical. An exponential decay would be more accurate, but costly to evaluate numerically, which is why the $1/R^{12}$ form is chosen instead. The second summand belongs to dispersion interaction. The $1/R^6$ form can be derived from perturbation theory as the first correction to mean-field, Hartree-Fock like electronic interaction. Eventually, bonded and non-bonded contributions together yield the complete force-field energy V:

$$V(\mathbf{R}_1, ...) = V_{\text{bond}}(\mathbf{R}_1, ...) + V_{\text{angle}}(\mathbf{R}_1, ...) + V_{\text{dihedral}}(\mathbf{R}_1, ...) + V_{\text{electrostatic}}(\mathbf{R}_1, ...) + V_{\text{van-der-Waals}}(\mathbf{R}_1, ...) \tag{2.84}$$

The free parameters can be fitted to experimental data or first-principle calculations. The development of good force-fields is difficult. In this thesis, we use different force-field parameters from the literature, except for the bonded parameters k_B and R_b that we fit to equilibrium geometries and normal mode frequencies from first principle calculations. Because there is little interdependence of those and other parameters, such a fit is straightforward and greatly improves the accuracy of the molecular vibrational frequencies that affect intermolecular charge and energy transport.

Molecular dynamics

Most of the time, force-field methods are not used to calculate static properties of single structures, but to sample static and time-dependent properties dependent on the nuclear coordinates and momenta, like thermal expectation values $\langle A(\mathbf{R},\mathbf{P})\rangle$ and time-dependent correlation functions $\langle A(\mathbf{R}(t),\mathbf{P}(t))B(\mathbf{R}(0),\mathbf{P}(0))\rangle$. Here, A and B are classical functions of the positions and momenta, not quantum mechanical operators. Likewise, we consider the positions and momenta as classical phase space variables. Molecular dynamics (MD) considers the time evolution of a classical, many-atom system, described by a Hamiltonian function $H(\mathbf{R}_1,\mathbf{P}_1,...) = T(\mathbf{P}_1,...) + V(\mathbf{R}_1,...)$. $T = \sum_i \frac{\mathbf{P}_i^2}{2M_i}$, with the atomic masses M_i, is the classical kinetic energy; V the potential energy that can come directly from an electronic structure calculation (ab initio MD), but for large systems is usually calculated with a force-field. The system's time evolution follows the classical canonical equations:

$$\frac{d\mathbf{R}_i}{dt} = \frac{\partial H}{\partial \mathbf{P}_i} \tag{2.85}$$

and

$$\frac{d\mathbf{P}_i}{dt} = -\frac{\partial H}{\partial \mathbf{R}_i}. \tag{2.86}$$

In the Cartesian coordinates we use here, eq. 2.86 reduces to $\frac{d\mathbf{R}_i}{dt} = \frac{1}{M_i}\mathbf{P}_i$, yielding after insertion into eq. 2.85:

$$M_i\frac{d^2\mathbf{R}_i}{dt^2} = -\frac{\partial V(\mathbf{R}_1,...)}{\partial \mathbf{R}_i} = \mathbf{F}_i, \tag{2.87}$$

with the forces $\mathbf{F}_i = -\frac{\partial V(\mathbf{R}_1,...)}{\partial \mathbf{R}_i}$. This is the classical Newtonian equation of motion. Most MD codes for chemical applications use Cartesian coordinates and, hence, solve Newton's equation. In this thesis, we use the Gromacs code [60] to integrate eq. 2.87 numerically. Gromacs offers several integration algorithms, of which we opt for the leap-frog algorithm [61]. Leap-frog evaluates positions and velocities $\mathbf{V} = \frac{d\mathbf{R}}{dt}$ at alternating moments in time. First one expands

$$\mathbf{V}_i\left(t + \frac{1}{2}\Delta t\right) \approx \mathbf{V}_i\left(t - \frac{1}{2}\Delta t\right) + \frac{1}{M_i}\mathbf{F}_i(t)\Delta t, \tag{2.88}$$

then

$$\mathbf{R}_i\left(t + \Delta t\right) \approx \mathbf{R}_i(t) + \mathbf{V}_i\left(t + \frac{1}{2}\Delta t\right)\Delta t, \tag{2.89}$$

with the time step Δt, usually on the order of 1 fs. With initial conditions $\mathbf{R}_i(0) = \mathbf{R}_0$ and $\mathbf{V}_i\left(-\frac{\Delta t}{2}\right) = \mathbf{V}_0$ these iterative expressions define the time evolution of the system. Locally the expansion error is of $O(\Delta t^3)$ because quadratic terms cancel, so that globally the error is $O(\Delta t^2)$. Crucially, leap-frog conserves energy on average for small enough time steps, leading to stable and physically meaningful dynamics. The peculiar offset of $\Delta t/2$ between position and momentum evaluations avoids the addition of terms of different order in Δt, which is important for the numerical stability of the simulation.

Thermal and pressure equilibration

The canonical equations lead to energy conserving dynamics $E = T(\mathbf{P}) + V(\mathbf{R}) = \text{const.}$. Thus, naive molecular dynamics simulations sample a microcanonical ensemble in the sense of statistical mechanics. If N is the number of atoms, and V a volume to which the system is confined, we also speak of an NVE ensemble. However, normally the canonical, or NVT, ensemble, where only the expectation value $\langle E \rangle$ of the energy is fixed, corresponds best to experimental conditions that allow energy exchange with the environment. Then, the probability for the system to attain energy E should be $p(E) = e^{-\beta T}/Z$, with $\beta = 1/(k_B T)$, temperature T, and the partition function $Z = \int d^{3N}R d^{3N}P e^{-\beta E(\mathbf{R},\mathbf{P})}$. Canonical energy distribution has to be introduced artificially by suitably altering the dynamics. To this end, there are various ways. One way is to turn Newton's equation into a stochastic differential equation by addition of a random force term, leading to a Langevin equation. In this work, another approach is used. Nosé and Hoover showed that there is a unique deterministic way to enforce a canonical ensemble through the addition of a dummy degree of freedom s. This algorithm is known as the Nosé-Hoover thermostat [62, 63]. s is linked to the rest of the system in the form of a friction term $-s\mathbf{P}/M$, yielding altered equations of motion:

$$M_i \frac{d^2\mathbf{R}_i}{dt^2} = \mathbf{F}_i - s\frac{d\mathbf{R}_i}{dt}. \tag{2.90}$$

s obeys its own equation of motion:

$$\frac{ds}{dt} = \frac{1}{Q}(T - T_0). \tag{2.91}$$

Q is a parameter controlling how strongly the thermostat alters the dynamics of the system. T_0 is the desired temperature, while T is the estimated current temperature of the system. The equipartition theorem is employed to estimate $T = \frac{2}{3Nk_B}\sum_i \frac{\mathbf{P}_i^2}{2M_i}$. Under experimental conditions often the volume of the system may vary, while the pressure P is fixed, leading to an NPT

ensemble. In that case, with a second dummy degree of freedom, dynamics can be altered to achieve the correct average pressure. This Parrinello-Rahman barostat works similarly as the Nosé-Hoover thermostat [64, 65]. Some of the dynamical simulations presented in this thesis are in the NVT, some in the NPT ensemble. Usually, there is little difference for solids, but for liquids effects of pressure coupling are more pronounced.

2.2 Fundamentals of charge and energy transport

This thesis aims to provide new tools for the study of charge and energy transport processes in molecular materials. There is a wide range of materials than can be considered molecular for the purpose of the methods to be introduced, but, specifically, we will think of bulk materials composed of organic molecules that are semiconductors. Organic semiconductors come as amorphous and crystalline materials. Since the latter tend to be particularly effective conductors, a special focus will be on molecular crystals. Organic semiconductors are of significant and growing industrial interest. They feature prominently in three kinds of devices: as organic field effect transistors (OFETs), as organic photovoltaic devices (OPVs), and as organic light emitting diodes (OLEDs). In the light of their usefulness, much theoretical and modeling research has been undertaken. Theory mostly contributes to development in two ways: through a more thorough understanding of the fundamental driving forces, allowing for educated molecular design, and as a tool for fast screening of potential materials in the huge space of chemically feasible molecules. Most of the commonly used models apply in one of two possible limiting cases in which charge or excitations are spatially either highly localized on individual molecules, or fully delocalized throughout the system. In the following, we will review the origin of both regimes and the fundamental ideas behind the methods dealing with them. As far as energy transport is concerned, in this thesis we confine ourselves to energy transport in the form of Frenkel excitons. A Frenkel exciton is a molecular excitation localized on a single molecule, that is, there is no charge transfer from one molecule to another. One can also think of it as an electron-hole pair bound on a single molecule. While the extend of the excitation itself is confined, excitations on different molecules are coupled, so that excitons can move around via the combined excitation and deexcitation of a pair of molecules. Exciton and charge movement then take on the same form and can often be studied on the same footing, albeit arising parameters have different origins. Therefore, many results about charge transport apply to exciton transport as well, and the following discussion is meant to apply to both of them. To simplify language, we may sometimes refer to only one, but mean both. In chapter 4 the Frenkel exciton model is explained in more detail.

One very important property of interest is how easily charges and excitons can move around. For charge transport the corresponding quantity of interest is the charge carrier mobility μ:

$$\mu = \frac{\langle v \rangle}{E}. \tag{2.92}$$

Here, the expectation value of the velocity $v = \frac{dx}{dt}$ is the drift velocity of the charge under the influence of the external electrical field of strength E. In principle, μ is a 2-rank tensor because in anisotropic materials a field applied in a certain direction can cause charges to move in another, but since μ is positive semidefinite, it can be diagonalized and decomposed into three independent one dimensional mobilities. The conductivity σ of a semiconductor is to μ alongside the charge carrier density ρ as $\sigma = \rho_c \mu$. Because the Fermi level lies above the valence band in semiconductors, charge carriers are either electron excited to the conduction band, or the holes in the valence band, which they leave behind, that behave as effective particles with positive charge. μ can depend on the field E, but is constant in the low field limit $E \to 0$. It is related to the diffusion constant D through a fluctuation-dissipation theorem, the Einstein-Smoluchowski relation:

$$\mu = \frac{D}{k_B T}. \tag{2.93}$$

The relation connects the field induced, directed movement with the random, thermally induced movement, where the average distance traveled in time t is

$$\sqrt{\langle (x(t) - x(0))^2 \rangle} \sim \sqrt{Dt}. \tag{2.94}$$

Obviously, because excitons posses no charge, electrical fields cannot cause them to move, and consequently no mobility μ can be defined. They do, however, diffuse through the material and their proneness to move is still quantifiable by the diffusion constant. For example, exciton diffusion is very important in OPVs because phonons are absorbed in the bulk, but charge separation takes place only at interfaces, which the excitons have to reach.

2.2.1 The Holstein model

In this section we explore the Holstein model [66], a simple toy model for an organic crystal. While the model, introduced in 1959, simplifies much of the complex physics of molecular materials, it still offers a useful picture that highlights the essential forces shaping transport processes to large degree. The model is visualized in Fig. 2.3. We consider a one dimensional molecular crystal into which we place a single charge or exciton. The nuclear degrees of freedom of each molecule i are described by a single coordinate x_i, and the molecular potential energy surface is expanded to second order, so that the nuclear potential energy becomes a parabola $E_{nuc} = \sum_i \frac{1}{2} M \omega x_i^2$, with the molecular vibrational frequency ω, and nu-
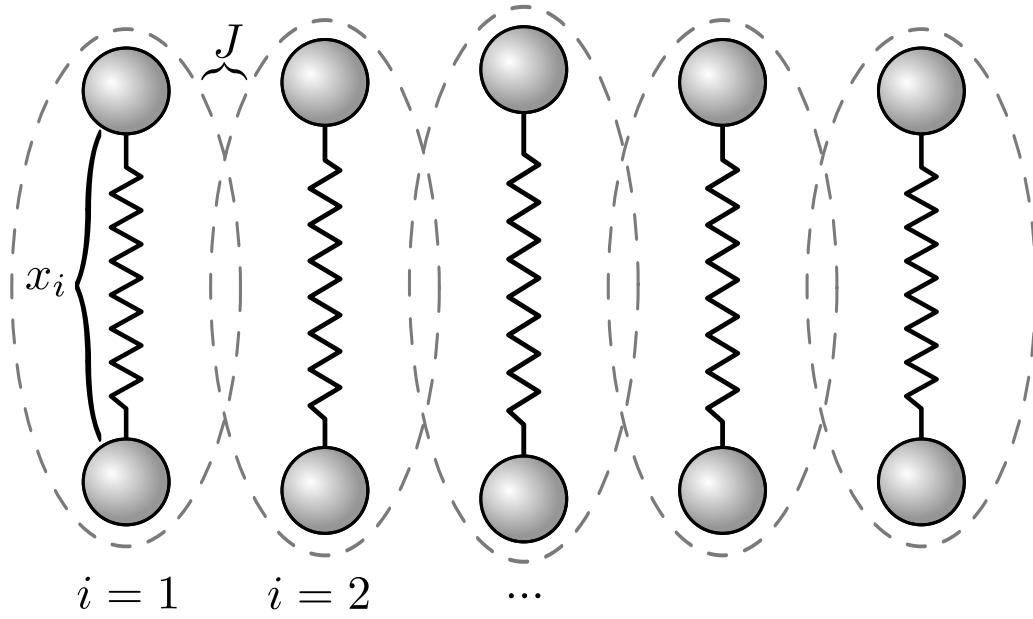
Figure 2.3: The Holstein model for a one dimensional molecular crystal. Molecules are modeled by one nuclear degree of freedom x_i, and one electronic state per site i, coupled to neighboring sites with coupling J.

clear effective mass M. For the wavefunction of the charge we assume only one state per site is necessary to describe it, with identical site energies, all put to zero, and couplings J to nearest neighbors. The corresponding Hamiltonian then takes on a simple tight-binding form $H_{\text{TB}} = J \sum_i \left(a_i^\dagger a_{i+1} + a_{i+1}^\dagger a_i \right)$, where the operator $a_i^\dagger$ creates a charge at site i, and its conjugate a_i destroys it. The ionization or excitation energy, as represented by the site energies, depends on the nuclear conformation x_i. To account for this, the change in energy is expanded to linear order, yielding the electron-phonon interaction energy $E_{\text{int}} = \sum_i \alpha x_i a_i^\dagger a_i$, with coupling constant α and the site occupation $a_i^\dagger a_i$. α is related to the strength of the reaction of a molecule to the presence of a charge. Completing the square, we see for a single molecule $E_{\text{nuc}} + E_{\text{int}} = \frac{1}{2} M x^2 + \alpha x = \frac{1}{2} M \left(x + \frac{\alpha}{M \omega^2} \right)^2 + \frac{1}{2} \frac{\alpha^2}{M \omega^2}$. Therefore, the presence of the charge causes a molecular reorientation, accompanied by an energy change

$$\lambda = \frac{1}{2} \frac{\alpha^2}{M \omega^2}. \tag{2.95}$$

λ is known as the internal reorganization energy of the molecule and has a very strong influence on the transport regime. Eventually, the full electronic Holstein Hamiltonian, as the sum of all terms, reads:

$$H = \sum_i \left(J \left(a_i^\dagger a_{i+1} + a_{i+1}^\dagger a_i \right) + \alpha x_i a_i^\dagger a_i \right) + \sum_i \frac{1}{2} M \omega^2 x_i^2. \tag{2.96}$$

Let $|i\rangle = a_i^\dagger|0\rangle$ be the state in which the charge is localized on a single site. The localized states form a basis in which to expand electronic wavefunctions:

$$|\Psi\rangle = \sum_i c_i|i\rangle, \tag{2.97}$$

with expansion coefficients c_i. In case all nuclear coordinates agree $x_1 = x_2 = ...$ the Holstein model is identical to a simple, one dimensional tight-binding model. Then wavefunctions $c_j \sim e^{ikdj}$, with lattice spacing d and wavenumber k are electronic eigenstates, as is easy to verify by insertion. The energy spectrum for $x_1 = x_2 = ... = 0$ forms a band with dispersion relation

$$E(k) = -2J\cos(kd)$$
$$\approx -2J + Jd^2k^2 \quad \text{for small } k. \tag{2.98}$$

The band is, however, not the ground state, but there are bound states with lower energy. Those states require $x_i \neq 0$, coupling the charge and the nuclei, and forming a bound pair of charge and molecular deformation, known as a polaron. Clearly, the presence of bound states with energies below the band can have a huge impact on charge mobility. When $E(x_1,...)$ is the minimal energy, then $\frac{\partial}{\partial x_i}E(x_1,...) = 0$ for all i. Applying this condition to the electronic eigenvalue problem establishes a connection between the wavefunction and the nuclear coordinates of the polaron:

$$x_i = \frac{\alpha}{M\omega^2}|c_i|^2 = \frac{2\lambda}{\alpha}|c_i|^2. \tag{2.99}$$

Hereupon it is possible to find the minimum in two limiting cases of either very large or small electronic coupling J between sites, relative to the electron-phonon coupling α. In the first case of large J, the wavefunction should still look much like a band solution, and hence be spread out over many sites. Therefore, this limit is known as the large polaron solution. Due to the large extension of the wavefunction, we can assume that i is a continuous index and expand $c_{i+1} = c_i + \frac{\partial c_i}{\partial i} + \frac{1}{2}\frac{\partial^2 c_i}{\partial i^2}$. Substitution into the eigenvalue equation yields the minimum energy

$$E_{lp} = -2J - \frac{1}{48}\frac{1}{J}\left(\frac{\alpha^2}{M\omega^2}\right)^2 = -2J - \frac{1}{48}\frac{\lambda^2}{J}. \tag{2.100}$$

Compared with the minimum energy $E_b = -2J$ of the band, this corresponds to a polaron binding energy of $E_{lp} - E_b = -\frac{1}{48}\frac{\lambda^2}{J}$. Assuming that in the large polaron limit λ is at most on the order of J, and a typical large value of $J \approx 100\,\text{meV}$, the binding energy is on the order of $1\,\text{meV}$. At ambient temperature $T = 300\,\text{K}$ the typical thermal energy is about $k_BT = 26\,\text{meV}$, which is much larger. Thus, as the band is easily thermally accessible, the Holstein model suggests transport behavior in the large polaron limit is largely determined by the band structure of the crystal.

Next, we tend to the other limit where J is small. At $J = 0$ a possible eigenstate is given by $c_i = \delta_{ii_0}$ for some i_0. From this state perturbation theory in J yields the corrected solution:

$$c_i = \delta_{ii_0} + \frac{JM\omega^2}{\alpha^2}\left(\delta_{i(i_0+1)} + \delta_{i(i_0-1)}\right) = \delta_{ii_0} + \frac{J}{2\lambda}\left(\delta_{i(i_0+1)} + \delta_{i(i_0-1)}\right). \tag{2.101}$$

Because λ is much bigger than J, the wavefunction is almost completely localized on one side. Therefore, this solution is known as the small polaron solution. The energy of the small polaron is given by

$$E_{\mathrm{sp}} = -\frac{\alpha^2}{2M\omega^2} = -\lambda. \tag{2.102}$$

The physical picture behind this is the charge localizing on one molecule and by reorganization it creates a potential well of depth λ. The magnitude of the binding energy $E_{\mathrm{sp}} - E_{\mathrm{b}} = -\lambda + 2J$ is much larger than the thermal energy at $T = 300\,\mathrm{K}$. Hence, the small polaron is stable, and in order to move an energy barrier λ has to be overcome by thermal activation. That is a typical scenario for transition state theory, which is, indeed, commonly used in this limit. In the following section, we will elaborate more on how to deal with the two extreme cases predicted by the Holstein model. Part of this thesis is concerned with the intermediate regime in between the extremes. The Holstein model ignores some effects that become important exactly there, such as the fluctuation of the couplings J here assumed to be constant. The extended Holstein-Peierls model [67], which includes coupling fluctuations, is still used for practical, predictive applications [68].

2.2.2 The hopping regime

In this section, we explore the hopping limit of charge and energy transport. As previously established, if the molecular reorganization energy is much larger than the intermolecular electronic coupling J, the charge or exciton becomes localized on a single site, and in order to move to a neighbor it has to overcome an energy barrier. The barrier is higher than the typical thermal energy in the molecule, so to reach the top of the barrier is a random event, driven by molecular vibration,+ that happens only occasionally. When the barrier is overcome through thermal activation, transport happens swiftly before the charge becomes trapped again on the next site. Essentially, the charge moves around by random hopping events, performing a random walk throughout the material bulk. Because the charge usually stays long enough on each site for it to relax and thermally equilibrate to a Boltzmann energy distribution, the charge's random walk is a Markov process. If $p_i(t)$ is the probability to find the charge on site i at time t, the time evolution of the probabilities, and hence the movement of the charge, obeys the master equation:

$$\frac{dp_i(t)}{dt} = \sum_j \left(p_j(t)k_{ji} - p_i(t)k_{ij}\right), \tag{2.103}$$
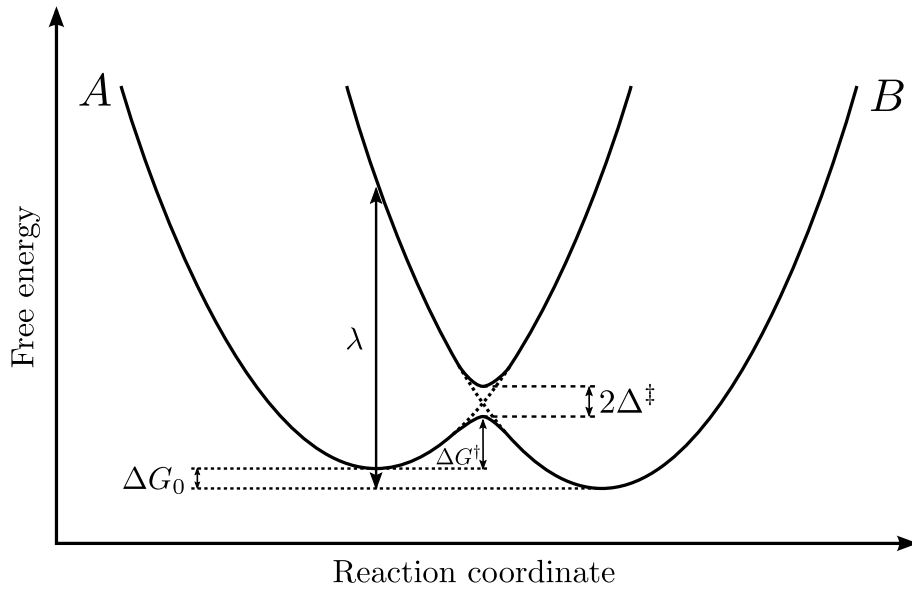
Figure 2.4: Visualization of free energy surface of the transfer process and the important quantities that appear in the rate equation.

where k_{ij} is the rate of transition from site i to j, i.e. the expected number of hops per time interval. Put into words, the change in probability to be on site i is composed of the chance to be on another site and move to i, reduced by the chance to already be on i but to move away to some other site. When an external field E is applied, the charge is more likely to hop into the field's direction, resulting in a drift. The transition rates k_{ij} determine the drift velocity $\langle v \rangle = \sum_{i,j} d_{ij} k_{ij}$, with the distances d_{ij} between sites. The drift may be anisotropic, but we suppress directional indices here for simplicity. The field induced drift is associated with the mobility

$$\mu = \frac{1}{E} \sum_{i,j} d_{ij} k_{ij}. \tag{2.104}$$

One of the fundamental problems of charge and energy transport in the hopping regime has now become to determine the transition rates k_{ij}. Under various assumptions about the nature and conditions of the intersite transfer, different expressions can be derived [69]. Classical transition state theory assumes that transfer only happens in a transition state, which is a well founded approximation if λ is much larger than J. Thus, transition state theory can be applied with the charge localized and relaxed on one site as initial state A, and localized and relaxed on a neighboring site as final state B. After expansion of the initial and final potential energy surfaces to quadratic order the transition state rate equation can be derived as [70, 71]:

$$k_{AB} = \nu_{\text{eff}} \kappa_{\text{el}} e^{-\beta \Delta G^{\dagger}}. \tag{2.105}$$

Here, ν_{eff} is the frequency of the effective mode that drives the transition, i.e. it is related to the curvature of the potential energy surface expanded in the reaction coordinate. A reaction coordinate commonly used for electron transfer processes [72, 73] is the energy gap $\Delta E(\mathbf{R}) = E_B(\mathbf{R}) - E_A(\mathbf{R})$ between the energy of the initial and final state at the nuclear conformation $\mathbf{R}$. κ_{el} is the electronic transmission coefficient, the probability of a transfer to actually happen when the transition state is reached. Assuming a single crossing of energies E_A and E_B, the transfer probability may be derived from the Landau-Zener model [74, 75], which exactly calculates the transition probability P_{LZ} in a two state system where the energy gap varies linearly in time $\Delta E \sim t$ from $-\infty$ to $+\infty$. Then [74, 75],

$$\kappa_{\text{el}} = \frac{2P_{\text{LZ}}}{1 + P_{\text{LZ}}}, \qquad (2.106)$$

with

$$P_{\text{LZ}} = 1 - e^{-2\pi\Gamma},$$
$$2\pi\Gamma = \frac{\pi^{\frac{3}{2}} \langle |H_{AB}|^2 \rangle_{\text{TS}}}{\nu_{\text{eff}} \sqrt{\lambda k_B T}}, \qquad (2.107)$$

where $H_{AB} = \langle A|H|B \rangle$ is the electronic coupling of initial and final state. H_{AB} is the same as J in the Holstein model, but since the coupling may actually fluctuate, the expectation value at the transition state must be taken. The final quantity in the transition state rate expression is the activation free energy $\Delta G^\dagger$, the height of the reaction barrier. For charge and exciton transfer between small molecules the free energy is mostly identical to the energy because entropic contributions are small. $\Delta G^\dagger$ can be decomposed into two contributions:

$$\Delta G^\dagger = \Delta G^\ddagger - \Delta^\ddagger. \qquad (2.108)$$

$\Delta G^\ddagger$ is the diabatic activation energy, the energy of the initial state at the transition geometry. It is determined by the reorganization energy λ and the driving force ΔG_0, the equilibrium energy difference between final and initial state [76]:

$$\Delta G^\ddagger = \frac{(\lambda + \Delta G_0)^2}{4\lambda}. \qquad (2.109)$$

In crystals all sites are equivalent, so that ΔG_0 is entirely brought about by the external field: $\Delta G_0 = \pm E d_{AB}$ for charges or $\Delta G_0 = 0$ for excitons. In amorphous materials different environments, including polarizability, need to be taken into account. $\Delta^\ddagger$ is the lowering of the barrier due to the energy splitting caused by the interaction of initial and final state [76]:

$$\Delta^\ddagger = \langle |H_{AB}|^2 \rangle_{\text{TS}}^{\frac{1}{2}} - \frac{1}{\lambda} \langle |H_{AB}|^2 \rangle_A. \qquad (2.110)$$

The rate expression can be further simplified in the nonadiabatic limit $\Gamma \ll 1$ that assumes very fast transfer at the transition state. Under this assumption $e^{-2\pi\Gamma}$ can be expanded to first order, such that $1 - e^{-2\pi\Gamma} \approx -2\pi\Gamma$, and the rate simplifies to

$$k_{AB} = \frac{2\pi}{\sqrt{4\pi\lambda k_B T}} \langle |H_{AB}|^2 \rangle_{\mathrm{TS}} e^{-\beta \Delta G^{\ddagger}}. \qquad (2.111)$$

Eq. 2.111 is the famous Marcus rate expressions that has found ample use in charge transport simulations [77–80]. It has also been applied to exciton transport [81], although the alternative Förster rate [82] expression is far more popular for energy transport [83].

2.2.3 The band regime

Many high-performance organic semiconductors form crystals. As such they do not differ fundamentally from inorganic semiconductors, except for the usually weaker bond between lattice sites, and the larger electron-phonon coupling due to intramolecular relaxation. As already indicated by the Holstein model, if relaxation is not too strong, the crystalline band structure may prevail. Therefore, the band regime is the second commonly discussed transport regime, on the opposite end from hopping. Note that while band structure is most of the time associated with charge transport, the translational symmetry that leads to electronic bands can also cause excitonic bands to form. The methods for the study of the band transport regime are largely the tools solid-state physics has developed for inorganic semiconductors. The crystal geometry is invariant under translations $\mathbf{R} \to \mathbf{R} + \mathbf{a}$, where a is a multiple of the crystal lattice vectors. Because for that reason the Hamiltonian commutes with translation operators, there is a joint basis of eigenvectors, or in other words, electronic wavefunctions take the form of Bloch waves [84]:

$$\Psi(\mathbf{r}) = e^{i\mathbf{k}\mathbf{r}} u_{\mathbf{k}}(\mathbf{r}), \qquad (2.112)$$

where $u_{\mathbf{k}}(\mathbf{r} + \mathbf{a}) = u_{\mathbf{k}}(\mathbf{r})$ for a multiple $\mathbf{a}$ of the lattice vectors, and the wave number $\mathbf{k}$ is the momentum of state Ψ. Bloch states are spatially delocalized across the entire crystal, and hence the exact opposite of the localized states of hopping transport. The electronic spectrum then consists of a discrete set E_α, $\alpha = 1, 2, ...$ of continuous energy bands $E_\alpha(\mathbf{k})$. In semiconductors the Fermi levels falls in between bands, so that all bands are either fully occupied or vacated. Some charges are thermally excited from the filled valence band to the empty conduction band, resulting in only partially filled bands for electrons and holes. Excitonic bands are also normally only occupied by a few quasi-particles. Therefore, charge and energy carries can usually be modeled as quasi free particles. For a free particle the relation between its momentum k and kinetic energy T is $E(k) = \frac{k^2}{2m}$, with the particle mass m. Then, one of the classical canonical equations reads $\frac{dr}{dt} = \frac{\partial E(k)}{\partial k} = \frac{k}{m}$, relating momentum and velocity. The semiclassical approach to particle dynamics in semiconductors is to assume that the classical canonical equations are
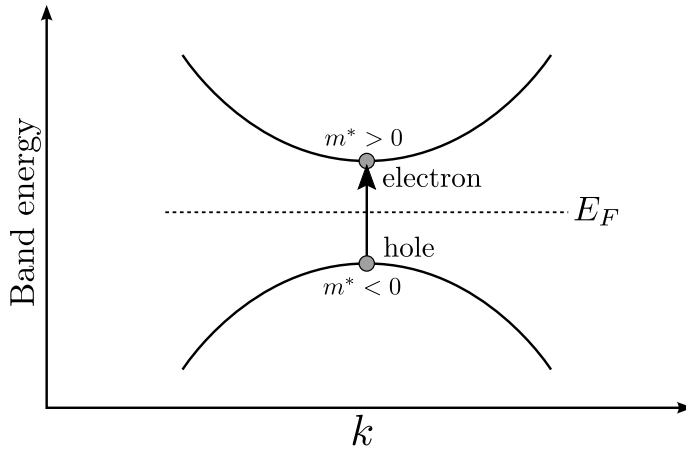
Figure 2.5: A charge is excited from the the valence to the conduction band, leaving behind a hole. The Fermi level E_F falls in between the two bands. The curvature of the bands is related to their effective mass m^* that can be negative.

valid, but the free particle dispersion relation is replaced with the band structure dispersion $E_\alpha(k)$ [85]. The velocity $\frac{d\mathbf{r}}{dt}$ can in this context be interpreted as the group velocity of the wavefunction. Near the band minima and maxima, where $\frac{\partial E_\alpha(k)}{\partial k} = 0$, $E_\alpha(k)$ can be expanded $E_\alpha(k) \approx E_0 + \frac{1}{2}\frac{\partial^2 E_\alpha(k)}{\partial k^2}k^2 = E_0 + \frac{k^2}{2m^*}$, resulting in same form as for the free particle, but with an effective mass m^* given by the band structure:

$$\frac{1}{m^*} = \frac{\partial^2 E_\alpha(k)}{\partial k^2}. \tag{2.113}$$

The effective mass m^* can differ extremely from the real mass of the charge carriers. In fact, m^* can even be negative and is typically anisotropic, although directional indices have been suppressed here for simplicity. Besides the band structure entering into m^*, the interaction of carriers and phonons needs to be accounted for, too. However, in the band limit, we may assume the interaction to take the form of occasional, random scattering events. Let $f(k,r,t)$ be the distribution function of momenta and positions at time t. In thermal equilibrium the time and position independent distribution $f_0(k)$ is given by the Fermi-Dirac or Bose-Einstein distribution:

$$f_0(k,r) = \frac{1}{1 \pm e^{(E_\alpha(k)-\mu)/(k_B T)}}, \tag{2.114}$$

where μ is not the mobility, but the chemical potential, and the sign is positive for fermions like electrons and holes and negative for bosons like singlet and triplet excitons. The time derivative of f excluding interaction with phonons is $\frac{df(k,r,t)}{dt} = \left(\partial_t + \frac{dr}{dt}\partial_r + \frac{dk}{dt}\partial_k\right)f(k,r,t)$ by the chain rule. The derivatives of r and k can be calculated according to the semi-classical equations of motion from above: $\frac{dr}{dt} = \frac{k}{m^*}$, and $\frac{dk}{dt} = \pm E$, in an external electrical field E. For excitons we set

$E = 0$ because they have no charge, and in the following we pick the minus sign of the electron case for simplicity. Hence follows the Boltzmann equation for transport in bands [85]:

$$\left(\partial_t + \frac{k}{m^*} \partial_r - E \partial_k \right) f(k, r, t) = \left(\frac{\partial f}{\partial t} \right)_{\text{coll}}. \tag{2.115}$$

The term $\left(\frac{\partial f}{\partial t} \right)_{\text{coll}}$ is called the collision integral and describes scattering on phonons. At only small deviations from the equilibrium distribution the relaxation time approximation is valid. It assumes that the extend of scattering is proportional to the distance from equilibrium:

$$\left(\frac{\partial f}{\partial t} \right)_{\text{coll}} = -\frac{f(k, r, t) - f_0(k)}{\tau(k)}. \tag{2.116}$$

Here, $\tau(k)$ is the relaxation time, which determines how fast the system relaxes back to equilibrium after a perturbation. τ is available from ab initio electronic structure calculations. One condition for the Boltzmann equation based approach to be valid is that τ is significantly larger than the typical transfer time from one site to the other, since otherwise the random scattering assumption breaks down. In the relaxation time formalism the Boltzmann equation is solvable in closed form, and one obtains for the conductivity σ [85]:

$$\sigma = -\frac{1}{3\pi^2} \int dk \frac{\partial f_0(k)}{\partial k} \frac{k^3}{m^*} \tau(k). \tag{2.117}$$

At small temperatures $\frac{\partial f_0(k)}{\partial k}$ is strongly peaked at the Fermi level: $\frac{\partial f_0(k)}{\partial k} \sim -\delta(k - k_F)$, allowing to approximate further $\sigma \approx \frac{\rho \tau}{m^*}$, with the carrier density ρ and the relaxation time τ at the Fermi level. Then, we directly find the mobility $\mu = \sigma/\rho$:

$$\mu = \frac{\tau}{m^*}. \tag{2.118}$$

This approximate expression for the mobility is known as the Drude form. It tells us that in the band limit the mobility is determined by the band structure and electron-phonon scattering. The former enters through the effective mass m^*, related to the curvature of the band, and the later in the from of the scattering time τ. The mobility increases with τ, that is, less scattering leads to higher mobilities. It decreases with m^*, which means that flat bands lead to lower mobilities.

3 Simulation of charge transport in bulk organic materials

3.1 Introduction

Charge transport in high performance organic semiconducting materials can be an intricate phenomenon. In the context or organic semiconductors, high performance usually means charge carrier mobilities on the order of $\sim 1 \frac{cm^2}{Vs}$ to $10 \frac{cm^2}{Vs}$. Amorphous materials often exhibit mobilities of $0.1 \frac{cm^2}{Vs}$ or less, while in traditional inorganic semiconductors mobilities far in excess of $100 \frac{cm^2}{Vs}$ are observed. In both extreme cases the mechanisms of charge transport are clear. In disordered materials with low mobilities, charges are localized on single molecules or molecular fragments and charge diffusion happens through random hops from one site to the other, brought about by thermal activation. In ordered, inorganic materials, on the other hand, electronic states are spatially extended, with well defined momenta, and form a clear band structure. Charges move around as quasi-free particles with an effective mass m^*, given by the band curvature, and randomly scatter off phonons on a time scale τ that is much larger than the time it takes to move from on atom to the other. However, because many materials such as organic and liquid crystals fall in between, the dominant mechanism is often not clear a priori. In fact, the intermediate may be a distinct regime altogether [10]. That casts doubt on the applicability of methods derived for the extreme cases in this regime. For example, the rate expressions used to calculate transition probabilities in the hopping regime assume thermal equilibration on each site. It has been known for some time that for many materials this is a questionable assumption [86]. Moreover, if states are localized over multiple sites, and localization fluctuates in time, it becomes difficult to define initial and final states among which transition probabilities can be calculated. Coming from the other end of the spectrum, if electron-phonon scattering times τ fall below the transition time from one site to the next, a Boltzmann equation based description of scattering is rendered invalid, and so are many methods from solid state physics. Then,

a different approach is required that explicitly takes into account the interaction of electronic and nuclear degrees of freedom. Obviously, a full solution of the time-dependent Schrödinger equation for both electrons and nuclei would be appropriate, but alas, is entirely untenable for the tremendous computational cost involved. Instead, one requires an approximate description on different levels. The nuclear dynamics can be treated classically, while the electrons have to be treated with quantum mechanics, so that a mixed quantum-classical dynamics scheme has to be used. Further, electronic structure calculations need to be fast, and therefore no high level methods can be used. Some have parametrized simple model Hamiltonians [68], which limits the generality of the model and requires ample preparation of each simulation. Others have used force-field like approaches to calculate electronic parameters [87], which also requires preparation and is somewhat less accurate. In this chapter, we apply a model for charge transport that exploits the molecular structure of a material and uses the approximate DFTB method [52, 53] for electronic calculations, as well as a force-field method for a large bulk of molecules. This method was first developed to simulate charge transport in DNA [88–90], was later applied to proteins [91], and eventually adapted by Heck et al. [14] for organic semiconducting materials. We will focus on the temperature dependence of the hole mobility μ as the property of interest because it is a characteristic reflection of the underlying transport mechanism. Depending on the active mechanism, vastly different trends are observable [92]. In amorphous materials and impure crystals mobility can often be observed to increase with temperature because thermal activation of the underlying hopping mechanism increases. If hopping takes place, there are actually various different transport regimes. Asymptotically for large temperatures, mobility follows a power law with an exponent of $-3/2$: $\mu \sim T^{-3/2}$. If band like transport dominates, mobility uniformly decreases with temperature because of increased electron-phonon scattering. In that case, the mobility universally follows a power law $\mu \sim T^{-n}$, where the exponent n can take on different values, and is not limited to $n = \frac{3}{2}$. Rate equation based approaches can not reproduce this behavior, because possible predictions are limited by the mathematical form of the rate expression that does not entail power law behavior over an extended temperature range with an exponent different from the asymptotical.

In the next section of this chapter, we will describe and explain the multiscale approach that has been used to simulate charge transfer. Then, simulations of hole transfer in an anthracene crystal are presented and results compared to experiment. Finally, we present results for other materials and draw conclusions.

3.2 Methodology

In this section, we introduce the multiscale method that has been used to perform the charge transport simulations. In its form adapted for organic semiconducting materials, it was originally published in Ref. [14], where a detailed derivation and explanation can be found.

We start out with a big bulk system that can contain hundreds of thousands or millions of atoms. If, for example, the system studied is a crystal, this would be a large cut out of the entire crystal, or, in other words, a $k \times m \times n$-fold duplication of the unit-cell, with k, m, n copies, respectively in the different crystal directions. The energy E_{tot} of this system is described at the force-field level. Compared to the cost of the quantum mechanical calculations the cost for the force-field calculations will be negligible, allowing a truly large environment. Partial charges on the atoms provide the electrostatic background. Out of this bulk, we select a subsection for quantum mechanical treatment. The charge will be confined to this region. At this point, we exploit the molecular structure of the problem. Electronic coupling between neighboring molecules in dispersion bound molecular materials is considerably smaller than interatomic coupling in inorganic crystals, held together by covalent interacions. Therefore, the material's electronic structure is well approximated by a composition of the electronic structures of the individual molecules or molecular fragments. For each molecule or fragment, a DFTB single-point calculation is run, either self-consistently (DFTB2) or not (DFTB1). Because there is usually little interatomic charge transfer in unpolar organic molecules, the DFTB1 level is sufficient [14], saving about 5 to 10 self-consistency cycles and an according factor in computational cost. The environment is included in this calculation through the force-field's atomic point charges as QM/MM coupling. If molecular fragments, rather than complete molecules, are present, the fragments are cut-off from the remainder of the molecule by replacing marginal atoms with hydrogen as linking atoms. Note that for fixed molecular size the calculation is naturally linear scaling with the size of the quantum region, and independent DFTB calculations are trivially parallel, permitting efficient parallelization. Hence, for each molecule I we find molecular Kohn-Sham orbitals $|\phi_I^m\rangle$. m labels the relevant molecular orbitals. Here, the next approximation comes into play. We shall consider only the transport of individual, isolated charges. The charge is transported through states that lie close to the Fermi level, and those states, in turn, are composed of molecular states near the HOMO level for holes, or LUMO for electrons. Therefore, depending on the energy gaps between Kohn-Sham orbitals, the index m is confined to HOMO or LUMO and perhaps some orbitals close in energy. The molecular orbitals then provide a small, yet sufficiently complete, basis set to express the charge wavefunction:

$$|\Psi\rangle = \sum_I \sum_m c_{Im} |\phi_I^m\rangle. \tag{3.1}$$

Next, we make use of Janak's theorem [24] that states that the DFT HOMO orbital eigenvalue is the same as the ionization potential of a molecule, and hence the expectation value of the Kohn-Sham Hamiltonian with respect to the HOMO orbital. While true for the exact functional, the statement does not hold as well for practical approximations, in particular GGA functionals. However, we only need to reproduce relative energies of different molecules, which by error cancellation is far more accurate. Then, the energy of the charge is $\pm\langle\Psi|H[\rho]|\Psi\rangle$, with plus for electron transport and minus for hole transport. To maintain simplicity of notation, we shall henceforth assume hole transport and pick the negative sign, as generalization remains straight forward. The full energy of a positively charged system now reads:

$$
\begin{aligned}
E &= E_{\text{tot}} - \langle\Psi|H[\rho]|\Psi\rangle + E_{\text{QM/MM}} \\
&= E_{\text{tot}} - \sum_{I,J}\sum_{m,n} c_{Im}^* c_{Jn}\langle\phi_I^m|H[\rho]|\phi_J^n\rangle + E_{\text{QM/MM}}.
\end{aligned}
\tag{3.2}
$$

$E_{\text{QM/MM}}$ is the Coulomb interaction energy of the charge with the bulk environment described with a force-field. At the DFTB level, the charge can be described by a Mulliken charge on the atoms A:

$$
\Delta q_A = \sum_I\sum_m |c_{Im}|^2 \left(\sum_{\mu\in A,\nu} a_{\mu m}a_{\nu m}S_{\mu\nu}\right),
\tag{3.3}
$$

where the $a_{\mu m}$ are the orbital coefficients, and the sum in braces can be limited to the molecule containing atom A because the overlap $S_{\mu\nu}$ decays exponentially with distance. Then, summing over all atoms $A \in$ QM that belong to the QM region, and the atoms $B \in$ MM that belong to the force-field region and have partial charge q_B, we have:

$$
E_{\text{QM/MM}} = \sum_{A\in\text{QM}}\sum_{B\in\text{MM}} \frac{\Delta q_A q_B}{|\mathbf{R}_A - \mathbf{R}_B|}.
\tag{3.4}
$$

Now, we can derive equations of motion for the electronic wavefunction and the nuclear positions. The wavefunction obeys the time-dependent Schrödinger equation, with the Hamiltonian $H_{mn} = \langle\phi_I^m|H[\rho]|\phi_J^n\rangle$, suppressing the molecular index:

$$
i\partial_t c_m = \sum_n H_{mn}c_m - i\sum_n c_n\langle\phi_m|\partial_t|\phi_n\rangle.
\tag{3.5}
$$

The Hamiltonian can be calculated with the DFTB expressions, which is fast, so that computational cost of this step is lower than the cost of the single molecular calculations. It has been found that while the magnitudes of the Hamiltonian elements calculated for fragments are systematically to small, multiplied with an appropriate correction factor, DFTB predicts very accurate Hamiltonians with an error small compared to other error sources [93, 94]. Such a
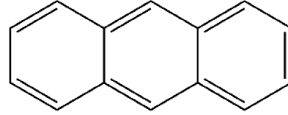
Figure 3.1: Structure of an anthracene molecule. Crystalline anthracene is prototypical for many high-performance organic semiconducting materials.

correction factor is applied. The last term represents the non-adiabatic coupling. The coupling can be rewritten as

$$\langle \phi_m | \partial_t | \phi_n \rangle = \frac{\langle \phi_m | (\partial_t H[\rho]) | \phi_n \rangle}{\varepsilon_m - \varepsilon_n}, \tag{3.6}$$

emphasizing its relationship with the orbital energy gap $\varepsilon_m - \varepsilon_n$. The coupling is low, effectively zero, whenever states are energetically well separated, or when the nominator matrix element is small, which is the case for states located on different molecules. For not too big molecules the energy spacing is usually quite large, so that the couplings are not very important. It becomes infinite when states cross. Here we assume $\langle \phi_m | \partial_t | \phi_n \rangle \sim \delta(\varepsilon_n - \varepsilon_m)$ for states on the same molecule. The nuclei coordinates follow the classical equation of motion:

$$\begin{aligned} M_i \partial_t^2 \mathbf{R}_i &= -\nabla_i E \\ &= -\nabla_i E_{\text{tot}} + \sum_{m,n} c_m^* c_n \nabla_i H_{mn} - \nabla_i E_{\text{QM/MM}}. \end{aligned} \tag{3.7}$$

The first derivative is calculated from the force-field, the final two can be analytically evaluated at the DFTB level. This way of calculating the forces as the derivative of the total energy is equivalent to the Ehrenfest, or mean-field, mixed quantum-classical propagation scheme [95]. Other schemes could be applied as well. In fact, in the next chapter, concerned with energy transport, surface-hopping will be used instead, and this is crucial, as will be addressed there. We find that because molecular relaxation tends to be weaker for charge than for energy transport, Ehrenfest propagation is often sufficient in case of the former.

3.3 Simulation of hole transport in anthracene

In this section, we look at hole transport in an anthracene (see Fig. 3.1) single crystal. Anthracene is an outstanding benchmark system to test methods for the prediction of charge transport properties in high mobility organic materials. First of all, it is a prototypical and simple system, consisting of three completely flat aromatic rings, with well understood electronic structure, and forming a crystal held together by dispersion interactions. Furthermore, high-quality experimental results are available. Because transport properties are extremely sensitive to crystal defects and impurities that can easily reduce mobility hundredfold and alter the transport mechanism, reliable measurements are hard to come by. Karl et. al. provide very detailed

time-of-flight mobility measurements for electrons and holes in ultra pure anthracene crystals [15]. Their measurements are resolved by crystal direction and temperature, allowing insides into the transport mechanism. Finally, for these reasons, many other theoretical studies address anthracene [67, 87, 96, 97], and direct comparison among them is possible.

3.3.1 Simulation setup and computational details

We simulate an anthracene single crystal block of $20 \times 20 \times$ unit-cells. Each unit-cell contains two molecules, leading to a total of 384000 atoms. The well known Herringbone structure of anthracene crystals and initial crystal parameters were adopted from experiment, but later allowed to change during pressure equilibration. We calculated force-field partial charges for the atoms according to the RESP fit procedure [98], where charges are fit to reproduce the molecular electrostatic potential predicted by a quantum chemical calculation. Bonded force-field parameters were assigned to reproduce ab initio predictions at the MP2/6-31G* level of theory. The GAFF force-field [99] is used for non-bonded interactions. GAFF has been found to perform reasonably well for organic crystals [100]. At the molecular mechanics level, we apply periodic boundary conditions, implemented as particle mesh Ewald sums for long-range electrostatic interactions and minimum image convention for short-range van-der-Waals interactions. The classical equations of motion for the nuclei are integrated with the leap-frog scheme [61] and a time step of $\delta t = 1\,\mathrm{fs}$. Version 4.6 of the Gromacs [60] molecular dynamics code performs all classical force calculations and integration of the classical equations of motion. We have implemented the DFTB and quantum dynamics code on top of Gromacs. Within the anthracene block, we have selected sets of 18 sequential molecules in each crystal direction (see Fig. 3.2). Thus, we regard a three dimensional problem as effectively one dimensional. Artificial confinement of the charge to one dimension does, of course, introduce an error, but since the probability to bypass a site in a given direction through entering the others is the probability to take the direct way squared (because two steps, rather than one, are taken), the effect should be small. Each molecule is a site for the purpose of the charge transport calculations. We confine ourselves to hole transport. Because anthracene is an unpolar molecule, there is little charge transfer between atoms, so we found the effect of self-consistency on the DFTB singe-point calculations to be negligible. Therefore, DFTB single-point calculations are carried out non-self-consistent, or, in other words, at the DFTB1 level. A Runge-Kutta (RK) integrator solves the time-dependent Schrödinger equation. Although RK is not unitary, and hence does not exactly preserve the norm of the wavefunction, we can set precision high enough to ensure that to within numerical accuracy the norm is preserved at each step, since computational cost is small compared to the DFTB single-point calculations. Thus, all simulations are numerically stable. We study hole transport at different temperatures to investigate temperature dependence as a proxy for the underlying transport mechanism. Temperature ranges from $T = 150\,\mathrm{K}$ to
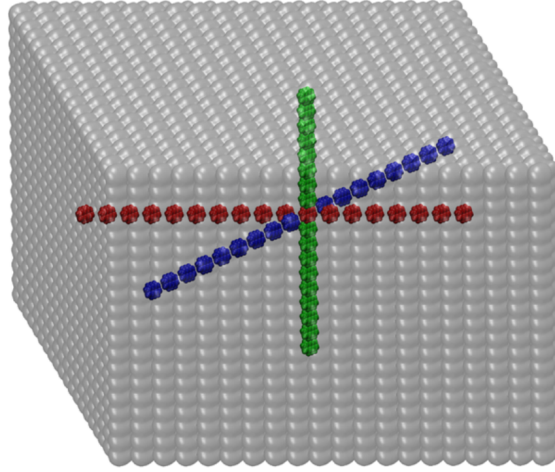
Figure 3.2: A $20 \times 20 \times 20$ block of anthracene. The colored molecules are selected for the DFTB and quantum dynamics calculations. The three crystal directions are: a (red), b (green), and c (blue).

$T = 400\,\text{K}$ in steps of $50\,\text{K}$. The Nosé-Hoover [62, 63] thermostat is used for temperature equilibration, with initial equilibration lasting several nanoseconds. Pressure is equilibrated to $P = 1\,\text{bar}$ with the Parinello-Rahman [64] barostat.

Using 100 uncorrelated, thermalized initial structures, the time evolution $|\Psi(t)\rangle$ of the hole wavefunction is computed, and each simulation lasts for $1\,\text{ps}$. The charge is initially located on a single site at the center of the molecular chain. Because mobilities are only extracted from the asymptotic diffusion of the charge, the initial conditions do not affect the results. At each point in time the position of the charge can be calculated as the expectation value of the position operator $\langle\Psi(t)|x|\Psi(t)\rangle$. Then, the statistical mechanical expectation value $\langle x(t)\rangle$ is the average of the quantum expectation over all trajectories $|\Psi_k(t)\rangle$:

$$\langle x(t)\rangle = \lim_{N\to\infty} \frac{1}{N} \sum_{k=1}^{N} \langle\Psi_k(t)|x|\Psi_k(t)\rangle \approx \frac{1}{N_{\text{sample}}} \sum_{k=1}^{N_{\text{sample}}} \langle\Psi_k(t)|x|\Psi_k(t)\rangle, \tag{3.8}$$

with the number of trajectories $N_{\text{sample}} = 100$. We calculate $\langle\Psi|x|\Psi\rangle$ as

$$\langle\Psi|x|\Psi\rangle = \sum_{I,m,J,n} c_{Im}^* c_{Jn} \langle\phi_I^m|x|\Phi_J^n\rangle \approx \sum_{I,m} |c_{Im}|^2 x_I^{\text{CM}}, \tag{3.9}$$

where x_I^{CM} is the center of mass of molecule I. The approximation holds well given the symmetry of the molecule. The charge performs a random, diffusive motion with diffusion constant D. In one dimension the squared spatial spread $\sigma(t)^2 = \langle x(t)^2 - \langle x(0)\rangle^2\rangle$ of the charge is then:

$$\sigma(t)^2 = \langle x(t)^2 - \langle x(0)\rangle^2\rangle = 2Dt. \tag{3.10}$$
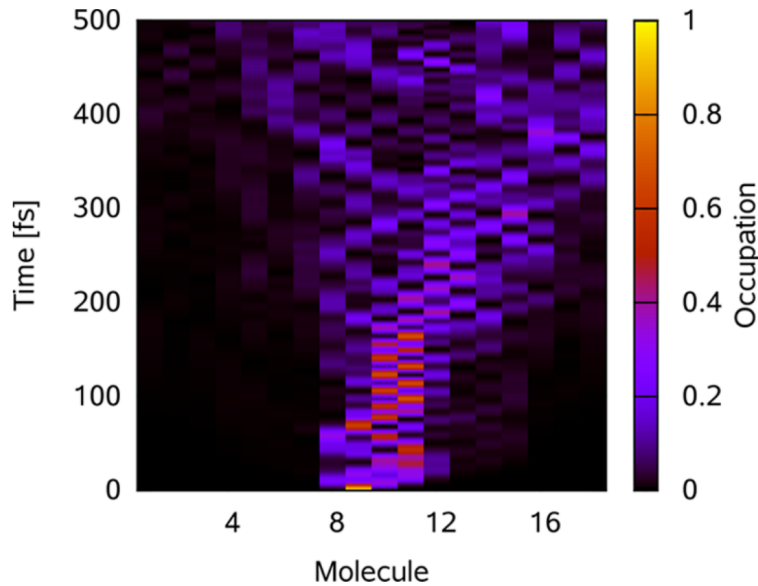
Figure 3.3: Sample trajectory of hole diffusion in anthracene in *b*-direction. The index on the *x*-axis represent the location of the charge.

Hence, we can calculate $\sigma(t)^2$ from the simulations and, in turn, compute D from a linear fit $\sigma(t)^2 = at + b$ with $D = a/2$. For this fit, we cut off the initial, ballistic regime, where $\sigma(t)^2 \sim t^2$. At the other end, simulation time is limited by the time it takes the charge to reach the boundary of the quantum region. We fit over a 500 fs interval in between. Diffusivity and mobility at low external fields are linked by a fluctuation-dissipation theorem, the Einstein relation:

$$\mu = \frac{D}{k_B T}. \tag{3.11}$$

Thus, we obtain mobilities from quantum dynamics simulations. Alternatively, one may directly apply an external field and calculate the drift velocity as a function of field strength. We tried this and found similar results. The alternative approach will, however, not be discussed further.

3.3.2 Results

A sample trajectory that exemplarily demonstrates the time evolution of the hole wavefunction is shown in Fig. 3.3. The charge is bounced around, and eventually the wave packet is broken up by scattering off phonons, whereupon it increasingly delocalizes until it is evenly spread throughout the system. This means, no stable polarons exist on the time scale of the simulations. Quick oscillations between neighboring sites are observable. They should be due to Rabi-like behavior of the charge when the energy levels of neighboring sites cross. The temperature dependent mobilities μ in all three crystal directions as extracted from the simulations are displayed in Fig. 3.4, and in Tab. 3.1 they are compared to experimental results at three different temperatures. We observe uniformly decreasing mobilities, following power-law
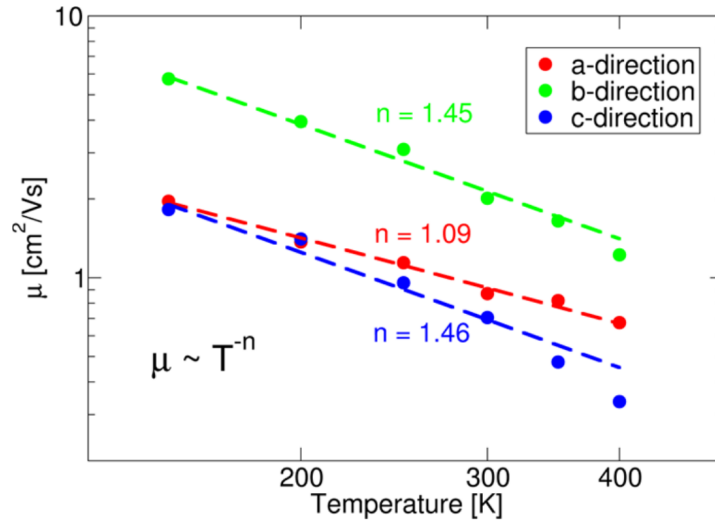
Figure 3.4: Simulated temperature dependence of hole mobility in anthracene in the different crystal directions. Mobilities follow a power-law $\mu \sim T^{-n}$ with different exponents n also shown in the figure.

Temp.	a-direction		b-direction		c-direction	
	sim.	exp.	sim.	exp.	sim.	exp.
200 K	1.37	2.22	3.95	5.05	1.41	1.98
250 K	1.14	1.51	3.09	3.74	0.96	1.2
300 K	0.87	1.14	2.01	2.93	0.7	0.85

Table 3.1: Simulated and experimentally measured [15] hole mobilities $\mu \left[\frac{cm^2}{Vs} \right]$ in anthracene at different temperatures.

	a-direction		b-direction		c-direction	
	sim.	exp.	sim.	exp.	sim.	exp.
Exp. n	1.09	1.5	1.45	1.34	1.46	2.38

Table 3.2: Simulated and experimentally measured [15] power-law exponents n of the temperature dependence $\mu \sim T^{-n}$ of the hole mobility in anthracene.

behavior $\mu \sim T^{-n}$ in all directions, in contrast to predictions by hopping models, but in accordance with experiment [15]. Exponents vary between $n = 1$ to $n = 1.5$. This indicates band-like behavior. Quantitatively, the predicted mobilities fall within a factor of two of experiment. For the formidable task of mobility prediction, such an agreement is very good, as it is often very difficult to even predict the correct order of magnitude. At ambient temperature the anisotropy of transport in different directions is correctly reproduced, although, as the relative temperature dependence is not exactly correct, there must, of course, be a temperature at which the ranking of transport efficiencies in different directions will no longer be correct. The power-law exponents n are reasonably well predicted, but the predicted exponent in c-direction in particular is somewhat too small. Two exponents are overestimated, while one is underestimated, so the error is not systematic.

3.4 Conclusion

By considering the real time evolution of the charge wavefunction, we successfully predicted the power-law form of the temperature dependence of the hole mobility. As has been outlined in the introduction, in order to predict the power-law, a band-like transport mechanism must be reproduced. The real time propagation scheme indeed achieves a description of this mechanism, confirming that it is appropriate in this regime. Visual inspection of the wavefunction time evolution, as in Fig. 3.3, reveals a tendency of the charge to completely delocalize with time. The strong delocalization is likely an artifact of the mean-field coupling of the classical and quantum subsystems. The Ehrenfest mean-field approach fails to account for decoherence. Therefore, once a wave packet gets split in two by scattering off a phonon, the wavefunction always remains in a superposition of the two new wave packets and is never recollapsed unto one. Because the forces exerted on the nuclei by the charge are a weighted average over all charge locations (see eq. 3.7), molecular relaxation due to the charge will decrease with delocalization. Yet, we observe no artificially growing diffusivity over time. This result indicates that not relaxation, but fluctuation of the electronic coupling between molecules controls transport in the band-like regime, as some authors have proposed [10]. Indeed, the molecular relaxation energy of a single anthracene molecule at the mixed force-field/DFTB level is $\lambda = 87\,\mathrm{meV}$ and states tend to be delocated over two molecules, cutting the effective value in half. Then, the relaxation energy is of the same size as the typical intermolecular coupling, a ratio much lower than in amorphous organic semiconductors, where couplings are smaller. The erroneous delocalization caused by mean-field coupling begs the question of what happens in other materials with slower charge transport. Fig. 3.5 lists a set of different materials for which we performed hole transport simulations in analogy to those presented in this chapter for anthracene. Since the focus of this chapter is on the ability of the presented method to correctly describe the band-like regime in anthracene, we will not discuss the details of these simulations at this point. They are

Figure 3.5: Five different materials: a) anthracene; b) α-NPD, an amorphous material; c) P3HT, considering interstrand transport in an order section of the regioregular material; d) HBC-LC, considering transport in the columnar direction of the columnar liquid crystalline material; e) HBC-SAM, modified HBC forming a self assembled monolayer.


Figure 3.6: Simulated temperature dependencies of hole mobilities for the materials listed in Fig. 3.5.

available in the literature [101]. Nevertheless, it is illustrative to briefly compare the results that are displayed in Fig. 3.6. All but one of the studied materials are highly ordered and exhibit the same power-law temperature dependency we found for anthracene. All in all, observed mobilities in the ordered materials vary between $\mu \approx 0.1 \frac{\text{cm}^2}{\text{Vs}}$ and $\mu \approx 10 \frac{\text{cm}^2}{\text{Vs}}$, that is, they stretch over two orders of magnitude. One material, α-NPD, stands out. α-NPD is a typical amorphous material, and we see mobilities a hundred times smaller than in the other materials. Notably, mobility grows with temperature, implying that transport is thermally activated. This is an important results because it strongly suggests that real time propagation can actually describe different regimes, even though in the activated regime hopping based approaches are preferable. It has to be noted that for very long simulation times the mean-field delocalization error does affect α-NPD simulations, but charges remain localized for several picoseconds, long enough to observe charge hops.

Overall, real time propagation for charge transport yields very promising results. Its performance for anthracene and other materials suggests that it can be a valuable addition to the tool box of charge transport study in molecular materials. One important question is the effect of the mean-field quantum-classical coupling. This is a recurring theme that will come up again in the next chapter when energy transport is studied. There plain mean-field is found to be entirely insufficient, and we will turn to surface-hopping and other approaches.

4 Simulation of singlet exciton diffusion in bulk organic materials

4.1 Introduction

Following up on the discussion of charge transfer in the last chapter, this chapter discusses the simulation of singlet exciton transport in anthracene. A new method relying on dynamical propagation of the excitonic wavefunction will be introduced. In such a way, energy transport will be treated in analogy to hole transport in the last chapter.

Exciton migration in organic semiconductors is of great practical interest. Charge separation in organic photovoltaics [102–106] (OPVs), for example, occurs at the interfaces between different materials, but the majority of excitons are created in the bulk, where photons hit with largest probability. Therefore, exciton migration is a crucial step in the energy generation chain, critically influencing the overall performance. A thorough understanding of this process is therefore a prerequisite for an educated device and molecular design [83, 107].

So far, exciton migration in OPVs is mostly modeled by stochastic approaches, where it is assumed that localized excitations migrate via a random hopping process [83, 107]. This is justified when local relaxation energies (exciton-phonon-coupling) are large compared to interaction integrals [108, 109], which applies to many materials. Hopping rates are then obtained from theories such as Förster resonant energy transport theory [82, 110], requiring the determination of the spectral overlap, which can be somewhat cumbersome. Recently, also Marcus rates have been used for exciton transport in molecular crystals [81] bypassing spectral overlaps. In many applications, the fluctuations of couplings are not explicitly incorporated, which implies that one important dimension of exciton migration is missing in the picture. Couplings which appear as parameters in stochastic models may fluctuate strongly, with magnitudes comparable or even larger than average values [11, 12]. Not only rate-based models for incoherent transport are affected by strong fluctuations. The magnitude of the fluctuations rules out analytic approaches near the band-limit, which use re-normalization techniques to account for

polaronic effects as discussed e.g. in Refs. [111, 112]. Furthermore these fluctuations may have contributions on the time scale of intermolecular transport, making it difficult to consider these fluctuations as static disorder or as much faster as any other timescale. This renders many more models inapplicable, such as the Haken-Strobl-Reineker model for fast oscillations [113, 114] or a treatment of the disorder as static [115].

To circumvent these difficulties, we present a computational model which allows a direct simulation of non-adiabatic dynamics based on Frenkel-type excitons in molecular systems. While non-adiabatic simulation of excited states is a common tool e.g. in computational photochemistry, the focus of such approaches tends to be on short time-scales and usually small system sizes, not on transport through the bulk, studying relaxation processes [116–119] or energy transfer between two molecules [120]. To extend this approach to organic materials containing several hundreds of atoms and time-scales in the pico- to nano-second regime, we present here a multiscale-approach in the spirit of our previous work on electron transfer in biological [88, 121, 122] and organic materials [14]. The methodology is based on a combination of a model Hamiltonian with classical force field based molecular dynamics simulations, where both approaches are coupled going beyond standard QM/MM schemes. The QM basis is given by the fast approximated DFTB method [52, 53], and fewest-switches surface-hopping [123], as well as the Boltzmann corrected Ehrenfest methods [124, 125] are applied to couple classical and quantum degrees of freedom. Therefore, although certain approximations are required to establish a computationally efficient methodology, no fundamental assumptions about transport mechanisms have to be made.

The chapter is organized as follows:

First, we introduce the methodology fundamentally based on the TD-DFTB method, which is used to compute excitation energies and Coulomb couplings, which constitute the Frenkel Hamiltonian. This Hamiltonian is combined with the force field description of the entire system using a QM/MM type of approach. Coupled equations of motion for nuclear and electronic degrees of freedom are introduced, which are solved using Ehrenfest and surface-hopping approaches.

In a second step, we test the DFTB based Hamiltonian for excitation energies, excitonic couplings and relaxation effects, also considering the impact of structural fluctuations. The impact of the applied approximations, in particular the use of DFT-GGA functionals and neglect of exchange effects are evaluated.

Third, we apply the methodology to study the exciton diffusion in crystalline anthracene. The use of DFT-GGA functionals for this purpose is critically examined.

4.2 Methodology

4.2.1 QM/MM Approach

For the large systems treated here, we use a combined quantum mechanics/molecular mechanics (QM/MM) approach, where the majority of the atoms are described by a classical force field and only a small subset of molecules is selected for a quantum mechanical treatment and form our QM region, embedded into the classical environment. The QM/MM interaction term contains only non-bonding interactions, the VdW terms are taken from the force field and for the electrostatic interaction atomic point charges are obtained from a RESP fit [98]. For the MM part, we used the GAFF [99] force field, where we adjusted the bonding parameters in order to reproduce DFTB ground state geometries. This is a way to achieve a consistent treatment of ground and excited states geometries within the DFTB framework, since excited states forces and geometries are computed from TD-DFTB, as described below.

4.2.2 Excited states: Frenkel-Hamiltonian

The treatment of excited states is one of the crucial points in this methodology. One of the interesting questions, also determining the mechanism of exciton migration, is that of localization vs. delocalization of the energy carriers [83, 107]. A straightforward approach would be a super-molecular calculation, treating the excited state of the whole system, thereby allowing the excitation to (de-)localize according to energetic criteria. This is, however, not feasible, on the one hand from computational consideration, on the other hand due to errors inherent in many popular QM approaches. In gradient corrected DFT (GGA), for example, the delocalization error leads to a wrong description of charge transfer (CT) states, which would intrude the description of the low lying excitations, as discussed below in more detail. Unfortunately, even the use of range separated functionals is not necessarily of help, since the range separation parameter and the intermolecular distance intervene [126]. The use of a Frenkel-type Hamiltonian [127] circumvents this problem by constructing super-molecular excitations from locally excited states of the monomers. As long as CT states do not play a vital role in the migration process e.g. as trap states [126], this approach can effectively deal with the DFT errors. While such CT excitations with low energies can exist in organic semiconductors, their oscillatory strengths are normally close to zero and they are usually no major contributor to transport, so long as pure Frenkel states exist. Note that the same argument also applies for the description of electron transfer in chapter 3, where the fragmentation of the system effectively circumvents the

DFT delocalization problem [14]. Frenkel states can be expressed as a superposition of single molecular excitations [110]

$$|\Psi\rangle = \sum_I \sum_i c_I^{(i)} \left(\prod_{J<I} |0\rangle_J \right) |i\rangle_I \left(\prod_{J>I} |0\rangle_J \right). \tag{4.1}$$

Here, the states $|\cdot\rangle$ refer to the states of the single molecules whose tensor product forms the state of the system. The index I runs over all molecules, whereas i labels excited states on molecule I, with $i = 0$ being the ground state, $i = 1$ the first excited, $i = 2$ the second excited state, and so on up to, in principle, infinity. In many cases, however, there will be only one, or a few, low lying single molecular excitation of interest; all others can be pragmatically excluded from the description. In the following we will assume this for clarity of presentation and suppress the index i. However, generality is not lost and generalization of all expressions will be obvious. While there is no charge transfer between molecules, excitations on different molecules still couple. This results in the intermolecular Hamiltonian

$$H_{\text{Frenkel}} = \sum_I \Omega_I a_I^\dagger a_I + \sum_{I \neq J} J_{IJ} a_I^\dagger a_J \tag{4.2}$$

with $J_{IJ} = \langle I|H|J \rangle$. Ω_I is the excitation energy and $|I\rangle$ represents the state where the excitation is located on molecule I. The Coulombic contribution to the coupling J_{IJ} can be expressed in terms of transition densities [110]

$$J_{IJ} = \int d^3 r d^3 r' \frac{N_I(\mathbf{r}) N_J(\mathbf{r}')}{|\mathbf{r} - \mathbf{r}'|}, \tag{4.3}$$

which are in turn given by

$$N_I(\mathbf{r}) = \langle 0|_I \hat{n}(\mathbf{r})|i\rangle_I. \tag{4.4}$$

Transition densities are a property available from single molecule TD-DFT response calculations [51, 128] and by extension available from TD-DFTB [129] as well, which we will use in the following. To build the Frenkel-Hamiltonian, we have to perform quantum calculations only for each molecule separately. This leads to an enormous performance gain and to linear-scaling of computing time with the number of molecules. The reason why this expression includes only Coulombic, but not exchange, contributions is that in the ansatz for the Frenkel wavefunction no anti-symmetrization is performed. Had it been done, there would be further integrals contributing, which are not as readily evaluated. Further, we also assume that different molecular wave-functions are orthogonal. Neglecting exchange and overlap is a common approximation and justified for well separated molecules, though this is not necessarily the case in crystalline organic semiconductors, as detailed below. The two approximations are discussed in the literature [11, 130, 131] and have consequences in particular for exciton transfer between molecules,

separated by less than 5 Å, as they appear in organic materials. The assumptions, however, are not easy to drop. The evaluation of couplings using a super-molecular approach in combination with a diabatization scheme (e.g. Ref. [11, 132]) is more time-consuming, less computationally stable (state selection etc.) and does not work with DFT-GGA, because spurious CT states are introduced.

TD-DFT does not provide exact excited-state wavefunctions, even though the Casida-ansatz [128] can serve as an approximate replacement. Within this ansatz, approximate wave-function overlaps can be calculated and the overlap could be determined. The Casida-ansatz has been used before, e.g. to determine non-adiabatic couplings [133].

4.2.3 DFTB & TD-DFTB Method

All our quantum mechanical calculations are based on the semi-empirical method DFTB [52, 53], which results in a speed-up of several orders of magnitude compared to DFT. DFTB has been introduced in the background chapter, see section 2.1.3. The mio parameter set [53], based on the PBE [16] functional, is used.

After a self-consistent DFTB ground-state calculation, we are left with the ground-state density, but are interested in excited states. As detailed in section 2.1.2, within DFT one way to access excited states is via the time-dependent TD-DFT formulation by linear-response theory. One solves for singularities in the linear response to a time-dependent perturbation [128]. The same treatment is possible in TD-DFTB [129], leading, similarly to DFT, to the so called Casida equation

$$\sum_{jt} \left((\varepsilon_s - \varepsilon_i)^2 \delta_{ij} \delta_{st} + 4\sqrt{\varepsilon_s - \varepsilon_i} K_{is,jt} \sqrt{\varepsilon_j - \varepsilon_t} \right) F_{jt} = \Omega^2 F_{is} \tag{4.5}$$

This is a Hermitian eigenvalue problem on the space of orbital excitations. Indices $i, j, \ldots$ label occupied orbitals, while $s, t, \ldots$ refer to unoccupied virtual orbitals. The eigenvalues Ω are the excitation energies. The coupling matrix $K_{is,jt}$ describes the Coulombic interaction between orbital excitations and can be approximated in a DFTB spirit as [129]

$$K_{is,jt} = \sum_{A,B} q_A^{is} q_B^{jt} \gamma_{AB} \tag{4.6}$$

with the Mulliken transition charges

$$q_A^{is} = \sum_{v \in A, \mu} \frac{1}{2} (c_{vi} c_{\mu s} + c_{\mu i} c_{vs}) S_{\mu v}. \tag{4.7}$$

To solve the full eigenvalue problem is costly, as it requires $O((N_{\text{occ.}} \cdot N_{\text{virt.}})^3)$ operations. However, if only low lying eigenvalues are required, algorithms, such as the Davidson algorithm [134], allow to restrict the problem to a much smaller subspace. For the application to exci-

ton transport this is particularly easy. It is sufficient to limit the number of occupied orbitals included in the calculation to the highest $N_{\text{occ. incl.}}$ occupied and the lowest $N_{\text{virt. incl.}}$ virtual orbitals. Because a very similar eigenvalue problem is solved over and over again for different molecules and at each time step, it is possible to verify by inspection whether the number of included orbitals is large enough for the eigenvalues to be converged to the correct value. Thus, no iteration is necessary.

Besides the excitation energies, we also require the transition densities to form the Frenkel-Hamiltonian. In linear-response DFT they are given by

$$N(\mathbf{r}) = \sum_{is} \sqrt{\frac{2(\varepsilon_i - \varepsilon_s)}{\Omega}} F_{is} \phi_i(\mathbf{r}) \phi_s(\mathbf{r}) \tag{4.8}$$

The Frenkel-coupling can then be written directly as [135]

$$J_{IJ} = \sum_{A \in I, B \in J} Q_A Q_B \gamma_{AB}, \tag{4.9}$$

where the many-body transition charges are

$$\sum_{is} \sqrt{\frac{2(\varepsilon_i - \varepsilon_s)}{\Omega}} F_{is} q_A^{is}. \tag{4.10}$$

Note again, that all TD-DFTB calculations are performed for individual molecules. Only in the final calculation of the coupling in eq. 5.15 references to pairs of molecules are made. With the above set of equations the Frenkel-Hamiltonian can be build and is then used to describe the excited states dynamics. Tests for several organic molecules show a good performance of DFTB with respect to full TD-DFT results [135]. DFTB and TD-DFTB provide analytic expressions for the gradients of the energy and excitation energy, which we use to calculate the forces on the nuclei. For the rather complicated expressions, please refer to the original publications [136].

4.2.4 Real-time Propagation

With the Frenkel-Hamiltonian at hand, we can describe the exciton dynamics. The excited state $|\Psi(t)\rangle$ follows the time-dependent Schrödinger equation (TDSE)

$$i\partial_t |\Psi\rangle = H_{\text{Frenkel}} |\Psi\rangle. \tag{4.11}$$

As throughout the rest of this thesis, atomic units are used, so that $\hbar = 1$. Also, henceforth, the Frenkel suffix will be suppressed and the Hamiltonian H will refer to the Frenkel-Hamiltonian. Expanding out the TDSE in the basis of single molecular excitations, the equation becomes

$$i\dot{c}_I = \Omega_I c_I + \sum_{J \neq I} J_{IJ} c_J - i \sum_J c_J \langle I | \partial_t | J \rangle \tag{4.12}$$

The last term contains the non-adiabatic couplings of excitations. For excitations on differ-ent molecules, it is roughly proportional to the change in overlap of the states and small since the overlap of states localized on different molecules is small to begin with. Thus, if there is only one excitation per site, the basis of molecular excitations becomes diabatic upon ne-glect of the non-adiabatic couplings. In an adiabatic basis of eigenstates of the Hamiltonian the non-adiabatic couplings remain a significant contribution. Between excitations on the same molecule on the other hand, non-adiabatic couplings are responsible for photochemical relax-ation processes, e.g. a transition to the ground state. The terms are small as long as the energy gap between the states is large, in this case they can be neglected. In case these couplings become large, the molecules act as traps in the exciton transfer process. To account for these effects, high level quantum chemical methods have to be applied, i.e. these effects can not be treated on the model Hamiltonian level aimed at here. It is, however, possible in principle to account for the relaxation processes by ab initio calculations of these events, and supply a phenomenological rate for the relaxation, i.e. these effects could be fed into eq. 4.12 via a decay parameter determined from these more detailed investigations. We will not take this into account in the present work and therefore neglect the non-adiabatic coupling terms altogether. Therefore, the TDSE as applied simplifies to

$$i\dot{c}_I = \Omega_I c_I + \sum_{J \neq I} J_{IJ} c_J, \tag{4.13}$$

and the basis of localized excitations effectively becomes a diabatic basis.

The nuclei are described classically and follow Newton's law

$$m_i \partial_t^2 \mathbf{R}_i = -\nabla_i V_{\text{FF}} + \mathbf{F}_{\text{QM}}. \tag{4.14}$$

The classical force-field potential V_{FF} gives rise to all ground-state forces. $\mathbf{F}_{\text{QM}}$ is the negative derivative of the excitation energy and represents the difference of atomic forces in the ground and excited states.

The excited state forces are directly computed from TD-DFTB [136] and enter the equations of motion here. Thus, we include the dynamic response of the system to the excitation, which in rate based theories is represented by the reorganization energy. This is usually the factor with the strongest effect in thermally activated transport, because it enters exponentially. These

forces are used for the propagation using Tully's fewest switches surface-hopping [123] and an Ehrenfest type approach.

Fewest switches surface-hopping

In surface-hopping approaches the forces $\mathbf{F}_{QM}$ are calculated from single eigenstates $\mathbf{F}_{QM} = -\nabla E_i$ with $H|\Psi_i\rangle = E_i|\Psi_i\rangle$, where the active state $|\Psi_i\rangle$ used to calculate the forces is chosen stochastically. Recall that the E_i are eigenvalues of the Frenkel-Hamiltonian and thus represent excitation, rather than total, energies. For excitations largely localized on a single molecule I the gradients will be dominated by the gradient of the corresponding excitation energy $\mathbf{F}_{QM} = -\nabla\Omega_I$.

In Tully's fewest switches algorithm the probability $P_{i \to j}$ to hop from one active state to another is given by

$$P_{i \to j} = \delta t_{\text{hop.}} \frac{2\,\text{Re}\,\tilde{c}_i \tilde{c}_j^* \langle \Psi_i | \partial_t | \Psi_j \rangle}{\tilde{c}_i \tilde{c}_i^*}. \tag{4.15}$$

Here, $t_{\text{hop.}}$ is the time step between hopping attempts and the $\tilde{c}_i$ refer to the adiabatic expansion coefficients of $|\Psi\rangle = \sum_I c_i|I\rangle = \sum_i \tilde{c}_i|\Psi_i\rangle$. As we have no analytic expression for the non-adiabatic couplings $\langle \Psi_i | \partial_t | \Psi_j \rangle$, we approximate them with a numerical derivative $\langle \Psi_i | \partial_t | \Psi_j \rangle \approx \langle \Psi_i(t - \delta t_{\text{hop.}}) | \Psi_j(t) \rangle$, $i \neq j$. To ensure correct Boltzmann statistics, we multiply $P_{i \to j}$ with Boltzmann factors for transitions leading to increases in energy [137], rather than rescale velocities. Since we lack analytic expressions for the non-adiabatic couplings, we are barred from properly adjusting velocities of individual modes anyways and may assume immediate thermalization among them.

Usually, decoherence corrections are required with surface-hopping to produce the correct scaling of transfer rates with the coupling elements [138]. We follow Persico [139] and rescale the coefficients of the inactive states with an exponential decay factor

$$\tilde{c}_j \leftarrow \tilde{c}_j e^{-\delta t_{\text{hop.}}/\tau_{ij}}, \tag{4.16}$$

where the decoherence time τ_{ij} for the transition from active state i to state j is calculated with the phenomenological expression of Truhlar [140]

$$\tau_{ij} = \frac{1}{|E_i - E_j|}\left(1 + \frac{C}{E_{\text{kin.}}}\right). \tag{4.17}$$

E_i, E_j are the respective energy eigenvalues, $E_{\text{kin.}}$ is the nuclear kinetic energy and C adaptable parameter. Finally, the modulus of $\tilde{c}_i$ is adjusted to preserve the norm of the wave function.

As it turned out, though, in our study decoherence correction had only a negligible effect on the results, even for minimal values of C, and could be ignored for our test system. Calculations on

model molecular stacks have yielded the same conclusion [141], indicating that for transport in monomolecular organic semiconductors decoherence correction may often be unnecessary.

In extended systems with localized eigenstates, as are many bulk molecular systems at finite temperature, surface-hopping suffers from the trivial crossing problem. When the energies of two states cross, non-adiabatic couplings become very sharply peaked and diverge at precisely the crossing point. To alleviate this problem we take several measures. First, the state is always propagated in the diabatic basis of molecular excitations, where no reference to the non-adiabatic couplings is made and the TDSE is therefore very stable numerically. Even if intermolecular non-adiabatic couplings were not neglected, they would be small and hardly affect the stability of the propagation. Second, we use the flexible surface-hopping approach of Beljonne et al. [142] to reduce the number of crossing that occur. In this method a criterion is introduced based on which diabatic states $|I\rangle$ are dynamically included or ignored in the determination of the adiabatic states, whenever they couple weakly with the active surface $|\Psi_s\rangle$. Formally, molecule I is only included in the calculation, if

$$\frac{|\langle I|H|\Psi_a\rangle|}{|\langle \Psi_s|H|\Psi_s\rangle - \langle I|H|I\rangle|} > R_c, \tag{4.18}$$

where R_c is a parameter adjusting the fractions of molecules included. A reduction in the number of diabatic basis functions leads to less adiabatic states and naturally reduces the number of trivial crossing. Finally, different time steps $\delta t, \delta t_{\text{hop.}}$ and δt_{QM} are used for the propagation of the nuclei, between hopping attempts and for the propagation of the TDSE, respectively. Quantum calculations are performed with an interval of δt, which is chosen short enough to yield a smooth representation of the Hamiltonian and accurate nucleic dynamics. Even if the Hamiltonian varies smoothly, eigenstates may vary quickly near crossings, so we choose $\delta t_{\text{hop.}} < \delta t$ and interpolate the Hamiltonian between times $t - \delta t$ and t

$$H(t') = \left(1 - \frac{t'-t}{\delta t}\right) H(t - \delta t) + \frac{t'-t}{\delta t} H(t), \, t' \in [t - \delta t, t] \tag{4.19}$$

Because the computational effort of handling the Frenkel-Hamiltonian is negligible compared to the DFTB calculations, the hopping time step can be chosen much smaller. The state is propagated between hopping attempts with a time step δt_{QM}, dynamically chosen for desired accuracy.

Boltzmann corrected Ehrenfest method

A straight forward approach to the quantum forces $\mathbf{F}_{\text{QM}}$ is to adopt a mean-field (Ehrenfest) approximation. However, as it turns out, in this approximation $|\Psi(t)\rangle$ artificially delocalizes,

leading to an underestimation of molecular relaxation and hence a massive overestimation of diffusivity. As simple correction of one particular failure of this approach, the so called Boltzmann corrected Ehrenfest method [124, 125], has been suggested, which enforces a correct population of eigenstates. In the Boltzmann corrected Ehrenfest method the forces are also calculated in the mean-field approximation, like in conventional Ehrenfest approach. That means the quantum expectation value is used, but the dynamics themselves are modified. In order to achieve a Boltzmann population of eigenstates, the off-diagonal Hamiltonian elements are rescaled with Boltzmann factors

$$H_{IJ}^{\mathrm{qc}} = \sqrt{\frac{2}{1 + e^{-(\Omega_J - \Omega_k)/(k_B T)}}} H_{IJ} \tag{4.20}$$

$$\tilde{H}_{IJ} = \tilde{H}_{JI} = |c_I| \cdot H_{IJ}^{\mathrm{qc}} - |c_J| \cdot H_{JI}^{\mathrm{qc}}, k > j \tag{4.21}$$

The scaling factor modifies transition probabilities between states so that detailed balance holds and the correct equilibrium distribution is obtained. If non-adiabatic coupling terms (here neglected) are present, they need to be rescaled as well, precisely as the Hamiltonian, in order to achieve correct quantum statistics [125]. Technically rescaling should be performed in the adiabatic basis where actual energies are known. Nevertheless, when diabatic and adiabatic states are similar, it is possible to work in a diabatic basis [124]. In practice it should be verified to what extend this is fulfilled, which can be done readily through examination of the eigenstates from a sample simulation, either manually by visual inspection or quantitatively, for example by considering the inverse participation ratio. Similar adiabatic and diabatic states can be expected whenever there is strong localization, either caused by molecular relaxation or disorder. In the case of clearly coherent transport, adiabatic and diabatic states will likely be very different, albeit in this case the unaltered Ehrenfest method can already be expected to work well because missing decoherence is less important.

The corrected Ehrenfest approach has the advantage of simplicity and also efficiency as it turns out that mean-field calculations need less statistics than surface-hopping simulations. It must be stressed that this method does not include decoherence in a formally correct way. Therefore, it will fail to account for molecular relaxation due to artificial delocalization in the limit of long simulation times in the same way as the conventional Ehrenfest method. For the anthracene test system, however, this effect is mitigated at least for the time scales necessary to compute the relevant observables, as discussed in the results section. As long as the wave-function remains localized, as observed for these time-scales of about 10 ps, the missing decoherence does not seem to affect the dynamics significantly. This finding is also supported by the accurate predictions of charge transfer rates with mean-field methods [141] for a molecular dimer. There, a wave-function is initially localized on one molecule, a similar situation as found in our simulations for the bulk system, where the wave-function initially resides on a single molecule.

Moreover, decoherence corrections appear to have only a weak effect in surface-hopping transport simulation [141]. Our simulations using surface hopping with and without decoherence corrections lead to the same finding, the difference in diffusivity is very small (see results). Exciton transfer dynamics not including decoherence leads to a superposition of eigenstates, which can be spatially delocalized. In surface hopping simulations, this leads in principle to errors in the hopping probabilities, which does not seem to affect the dynamics seriously according to Ref. [141] and our simulations, while the excitation remains on a single adiabatic surface. The latter guarantees the correct evaluation of relaxation effects (λ), which is essential for correct description of diffusivity. In mean-field simulations, however, the artificial spread of the wave function leads to a superposition of adiabatic states, where as a result the relaxation effects are underestimated or practically neglected. And this is the effect which is efficiently suppressed by the Boltzmann weighting.

Generally, localization over sufficiently long time spans can be expected for systems with transfer parameters similar to anthracene, because the rate of delocalization will be about the same. If transport is fully coherent, delocalization is likely to occur too quickly, but then relaxation effects on transport are weak.

4.2.5 Implementation Details

For the molecular dynamics part of the simulation, force-field evaluation, and PME calculation of the electrostatic potential, we use Gromacs 4.6.1 [60]. On top of this, we have built our own implementation of DFTB and TD-DFTB, directly including it into the Gromacs code without making use of the QM/MM interface provided by Gromacs. Such a set-up was used before in our charge-transfer studies [13, 14]. The quantum dynamics methods have been implemented within Gromacs as well. The TDSE is propagated with a Runge-Kutta (RK) scheme. Although RK is not Hermitian and could thus lead to numerical stability issues, we dynamically choose the propagation time-step δt_{QM} such, that the norm is always conserved within numerical precision and, therefore, no problems arise. The time steps δt for propagation of the nuclei and DFTB calculations were 1fs and 0.5fs in Boltzmann corrected Ehrenfest and surface-hopping simulations, respectively. The hopping time step $\delta t_{\text{hop.}}$ was set to $\delta t/10000$. For the parameter R_c in flexible surface-hopping we set a value of $R_c = 50$, which we verified to be large enough to accurately represent relevant eigenstates in our test system anthracene.

4.3 Results

4.3.1 System Set-up

Crystalline anthracene is particularly suited as a test system, since experimental results on singlet exciton diffusion are available [143–145] and the lowest energy excitation is very well

Figure 4.1: Four sequential molecules in *a*-(left) and *b*- (right) direction. The QM regions contained chains of 18 molecules.
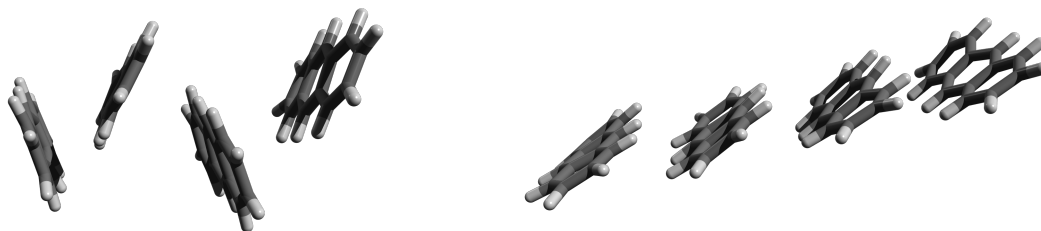
described by a Frenkel-like picture, thus avoiding complications with the electronic structure [146]. Furthermore, exciton couplings in anthracene show strong fluctuations [11], which provide motivation to consider direct dynamics. On the other hand, due to the large molecular relaxation energy of the anthracene molecule, we expect rather localized eigenstates. At first sight, simple hopping models may seem more appropriate, however, as has been pointed out before [11, 12] the time scales of fluctuation and transfer are similar. Further, the large relaxation energy allows us to assess how well we can handle these important effects and thus can be seen as beneficial for a benchmark.

The simulated system consisted of a crystal section made up of $20 \times 20 \times 20$ unit-cells. As the anthracene unit-cell is composed of two molecules, this means 16000 molecules were included overall. The Herringbone crystal structure is known from experiment which also provided initial lattice constants. These were allowed to change in a temperature and pressure equilibration at 300K and 1bar. Equilibration lasted several nanoseconds until temperature and volume had converged, with the Nosé-Hoover thermostat and Parinello-Rahman barostat applied.

We used the GAFF force-field [99] for the molecular mechanics description of the ground state potential energy surface, but adapted the geometry parameters to yield DFTB equilibrium geometries. Partial charges on the atoms were obtained from a RESP fit [98]. GAFF has been shown to work reasonably well for benzene crystals and other organic crystals [100].

In order to investigate exciton diffusion in two different directions, we selected two different QM regions made up of 18 sequentially aligned molecules along axes in the $a-$ and $b-$crystal directions (see Fig. 4.1).

4.3.2 Single-molecular Excitation

In a first step, we have to identify the relevant on-site excitations of which Frenkel-states are composed. We took single anthracene molecules from the equilibrated bulk for which we performed TD-DFTB calculations using our local Gromacs implementation, as well as the TD-DFTB implementation in the DFTB+ program [18] for comparison, showing identical results. Relevant excitations are those low in energy and with a non-vanishing oscillator strength f, meaning transition charges do not vanish. These can be excited by radiation and diffuse through the system, hence contributing to energy transport. We confine ourselves to singlet excitations. Calculations were also performed at the PBE/6-31G(d,p), B3LYP/6-31G(d,p) and ωB97X-D/6-31G(d,p) levels of theory, for comparison. PBE, from which DFTB is parametrized, helps to assess the quality of the tight-binding approximations. B3LYP contains some exchange but is known to underestimate excitation energies of the lowest lying excitations (precisely L_a and L_b) in oligoacenes [147, 148] while the range-separated ωB97X-D functional performs well for molecular dimers [149]. Note, that for higher energy excitations it has been found that hybrid and range-separated functionals actually overestimate excitation energies and local functionals may do better [150].

The calculated excitation spectrum shows that the lowest energy singlet excitation is the only one with a non-vanishing f within an energy range of more than 1eV. For the sample geometry TD-DFTB predicts an excitation energy of 2.72eV and oscillator strength $f = 0.056$ for this excitation. We find that this excitation is of B_u symmetry and is dominated by the transition from HOMO to LUMO (see Fig. 4.2).

PBE yields a very similar spectrum with an excitation energy of 2.79eV and coupling strength of 0.042 for the considered excitation, in good agreement with DFTB. TD-DFTB generally tends to reproduce PBE excitation energies well, including the whole potential energy surface, albeit also sharing its failings [151].

The B3LYP and ωB97X-D spectra are qualitatively similar, but with the relevant excitation energies shifted upwards, as expected. For the HOMO to LUMO excitation the energies and oscillator strengths are 3.037eV with $f = 0.063$ and 3.36eV with $f = 0.096$ for B3LYP and ωB97X-D, respectively. Since the monomer description is not problematic, we evaluate the estimates of the Frenkel couplings in a second step. For this, we perform calculations on a dimer of two neighboring molecules in the b-direction, again extracted from a MD trajectory. B3LYP predicts two low-energy charge-transfer states which, naturally, cannot be reproduced in the Frenkel spectrum. Two states composed of Frenkel excitations are predicted by B3LYP and the Frenkel-Hamiltonian. B3LYP excitation energies are again shifted upwards but the gap matches very well (see Fig. 4.3), since it is determined by relative single-molecular excitation energies and couplings. We did also perform (super-molecular) PBE calculations. PBE adds strong charge-transfer contributions to all excitations, because it underestimates their energies,
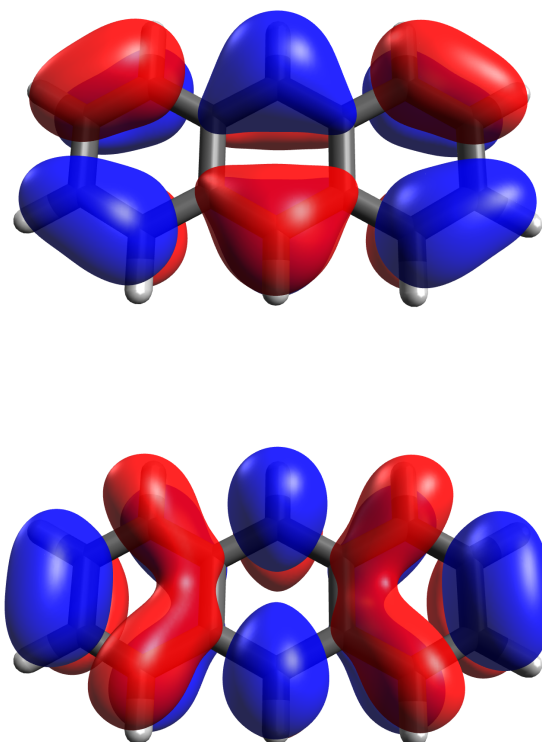
Figure 4.2: HOMO (top) and LUMO (bottom) orbitals of an anthracene. We consider the single-molecule excitation dominated by the transition from HOMO to LUMO.

thereby becoming unsuitable for such calculations. In summary, these tests indicate a reasonable description of exciton couplings using the fast TD-DFTB approach, despite the approximative character as described above.

4.3.3 Coupling Elements J

For a first analysis of the Frenkel couplings J in a- and b-direction we consider their distribution, determined from several hundred picoseconds of simulation. We find roughly normal probability density functions and particularly strong fluctuations in the a-direction (see Fig. 4.4). The average couplings and standard deviations are $\langle J \rangle = 4.7\text{meV}$, $\sigma_J = 10.4\text{meV}$ in the a-direction and $\langle J \rangle = 30.3\text{meV}$, $\sigma_J = 3.8\text{meV}$ in the b-direction (see Table 4.2).

The values of the average and also most probable couplings fall within the range of previously reported values (see Table. 4.1). Variations of values obtained in different studies may not only be due to different electronic structure methods but as well a consequence of somewhat different geometries coming from different force-fields or experiment crystal structures. It can be concluded that Coulombic couplings from TD-DFTB describe the most typical magnitude
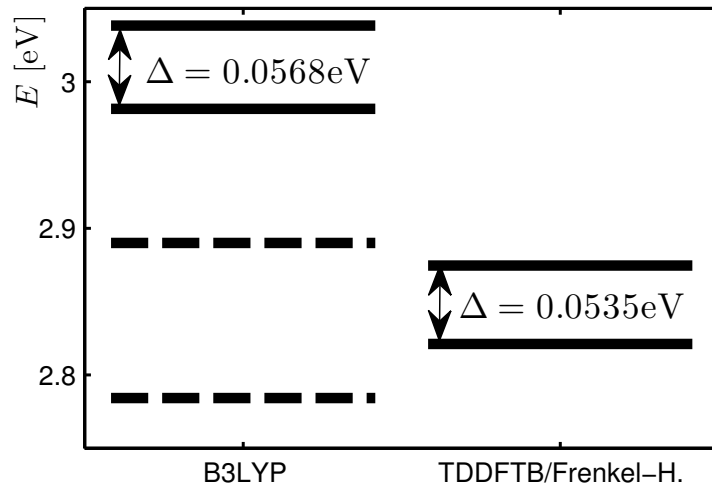
Figure 4.3: Low lying excitations of an anthracene dimer with B3LYP and the Frenkel Hamiltonian parametrized from TD-DFTB. TD-B3LYP predicts two low lying charge-transfer states (dashed line) and generally higher excitation energies. The gap induced by coupling Frenkel states is well reproduced.

Table 4.1: Comparison of average (DFT and DFTB) and static crystal structure (CC2) couplings [meV], obtained with different methods

Direction	TD-DFTB Coulomb	ωB97X-D Coulomb [11]	ωB97X-D supermol. [11]
a	4.7	6	8
b	30.3	23	35

Direction	SCS-CC2 dipole [81]	SCS-CC2 supermol. [81]
b	22	26

Table 4.2: Fluctuations $\sigma = \sqrt{\langle J^2 \rangle - \langle J \rangle^2}$ of the excitonic couplings J in [meV].

Direction	σ TD-DFTB Coulombic	$\frac{\sigma}{\langle J \rangle}$	σ with exchange [11]	$\frac{\sigma}{\langle J \rangle}$
a	10.4	2.21	22	3.1
b	3.8	0.125	10	0.28
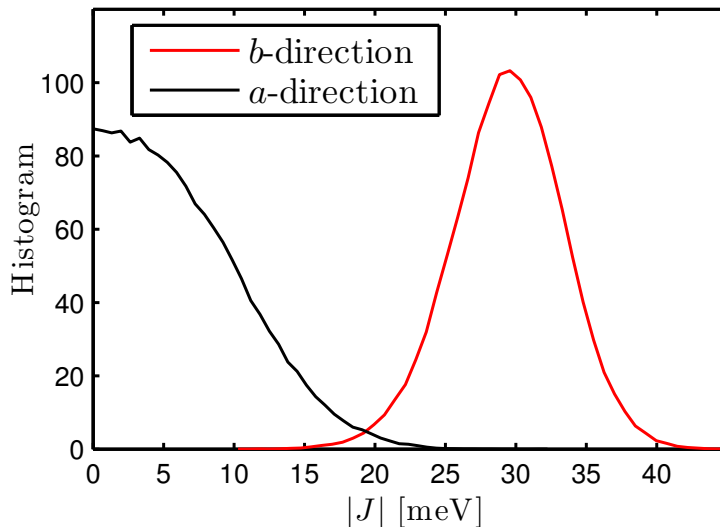
Figure 4.4: Histograms of the magnitudes |*J*| of the excitonic couplings, in the both directions.

quite well.

The couplings in both directions fluctuate around their average values but fluctuations in the *a*-direction are far more pronounced. In particular, because the average coupling value in *a*-direction is very small, the sign can change over time. The ratios $\frac{\langle J \rangle}{\sigma_J}$ between the standard deviations σ_J of the couplings and the average values $\langle J \rangle$ are 2.21 in the *a*-direction and 0.125 in the *b*-direction. That is, in the *a*-direction the fluctuations are much larger than the average value and correspondingly are the dominant contribution to the transport, since the diffusion constant D should be approximately $D \sim \langle J^2 \rangle = \langle J \rangle^2 + \sigma_J^2$. This means, fluctuations σ_J^2 contribute more than 4 times as much to transport as the average $\langle J \rangle^2 < 2^2 \sigma_J^2$. In *b*-direction fluctuations are much less pronounced in relation, yet are still not quite an order of magnitude smaller than the average.

In comparison to reported results, which include exchange effects [11], our fluctuations are smaller by a factor of about 2.5 and 2, in *a*− and *b*−direction respectively. While differences in the force-field description could in principle play a role, it is very likely a result of the neglect of exchange and overlap contributions to the coupling, as has been pointed out before [11], following a comparison of full couplings and Coulomb couplings. Reported distributions of Coulomb couplings (Ref. [11] in Supplementary Information) look very similar to ours. It is noteworthy, that we reproduce average couplings better than the fluctuations. Exchange effects appear to become particularly important at the tails of the coupling distributions, which come from more "extreme" geometrical conformations, such as pairs of molecules brought particularly close together by lattice vibrations.
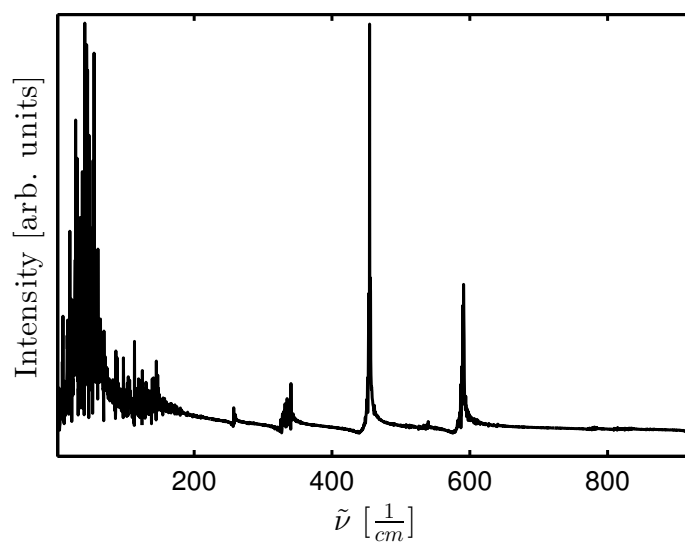
Figure 4.5: Fourier transformed auto-correlation function of J in the a-direction.
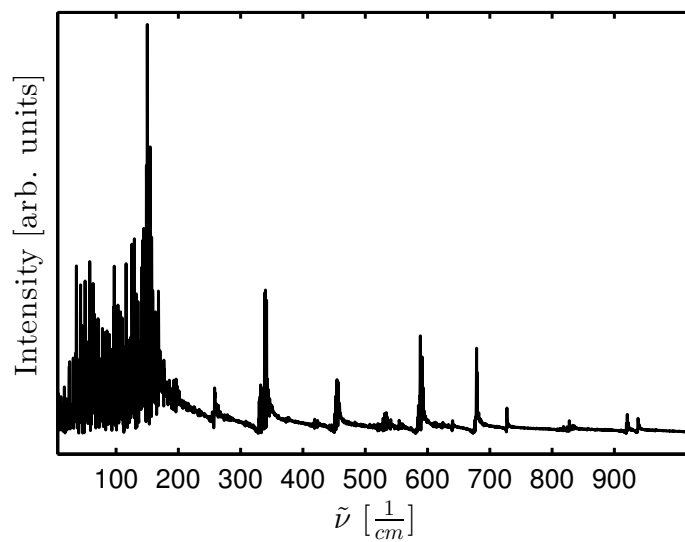
Figure 4.6: Fourier transformed auto-correlation function of J in the b-direction.

To investigate the time-scale of the coupling fluctuations, we calculate their spectra as the Fourier transform of the auto-correlation function $C(t) = \langle (J(t) - \langle J \rangle)(J(0) - \langle J \rangle) \rangle$. The spectra show many slow mode contributions, but also some faster contributions above 300 wavenumbers. The spectra are qualitatively similar to the previously reported ones [11, 12], though frequencies are shifted upwards somewhat. As the slow phonon frequencies are determined by the chosen force-field, it would be interesting to study not only the accuracy of their predicted structures but of the frequencies too.

Because TD-DFTB reproduces the results of of Aragó and Troisi [11, 12] reasonably well, their interpretation holds valid also for our study. The magnitude of fluctuations renders a band description of excitonic motion with phonon coupling inclusion via renormalization techniques impossible, because average couplings and fluctuations are comparably large. The time-scale of the fluctuations further complicates things as they are too slow to apply theories based on a decoupling of nuclear and electronic degrees of freedom, yet about as fast as the transport itself, so that a description as purely static disorder is invalid. Because of this, for transition rate based methods, which should be applicable for anthracene, non-Condon effects should be included.

4.3.4 Relaxation

Exciton-phonon coupling or molecular relaxation in the excited state is an important effect in excitation energy transport in organic semiconductors. Due to large relaxation energies transport tends to become decoherent. In order to study relaxation unbiased by diffusion, we placed a single excitation on a molecule and constrained it there. Molecular relaxation takes place very quickly, with the excitation energy dropping to a new equilibrium value on the time-scale of 10fs (see Fig. 4.7). This is much shorter than the typical intermolecular transport time, thus rendering transport incoherent almost instantly.

For incoherent transport, the relaxation energy $\lambda = E_{\text{exc.}} - E^*_{\text{exc.}}$ is decisive for transport efficiency, because the diffusion constant is related to it exponentially. Here, $E_{\text{exc.}}$ refers to the single-molecule energy in the ground state optimized geometry, whereas $E^*_{\text{exc.}}$ denotes the excitation energy in the geometry optimized in the corresponding excited state. The combination of a force-field description for the ground state and TD-DFTB for the excited state yields $\lambda = 302$meV, in good agreement with the PBE/6-31(d,p) value of $\lambda = 315$meV. However, this is much smaller than the reported value [81] of $\lambda = 533$meV from more accurate coupled-cluster calculations. As TD-HF overestimates the value by about as much as we underestimate it, the self-interaction error of DFT is likely responsible for the poor performance of local functionals and range-separated functionals would be a cure. The diffusion constant, however, is highly sensitive to the chosen functional [81], therefore fine-tuning at this point is the key to quantitative simulations of diffusivity.

The ratio of relaxation energy to typical coupling λ / J is about 10 in $b-$ and 50 in a-direction.
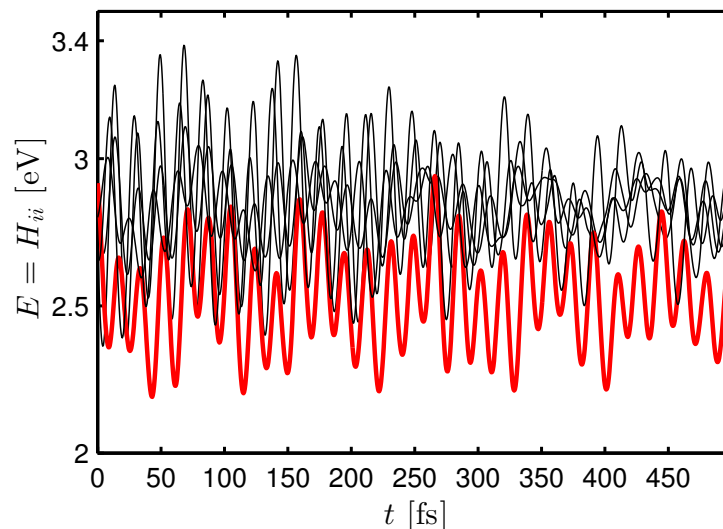
Figure 4.7: The red curve shows the excitation energy of a molecule unto which an excitation has just been placed, while the other curves refer to the excitation energies of un-perturbed sites. The molecule relaxes within 10fs to a new equilibrium level.

In either case this is quite large, predicting incoherent transport. With the coupled-cluster values for λ this becomes even more pronounced.

4.3.5 Diffusion

Ultimately, the objective is to predict transport efficiency by direct simulation of the semi-classical dynamics of the system. We performed simulations in which we excited a single molecule, equilibrated the system for a few hundred fs with the location of the excitation fixed and then evolved the wave-function and nuclear positions in time.

First, we performed simulations neglecting the excited states forces $\mathbf{F}_{QM}$ in eq. 4.14 and using conventional Ehrenfest propagation only. Both approaches reveal themselves as unfit very quickly, because they do not properly account for relaxation (see Fig. 4.8). Without quantum forces, diffusion constants come out on the order of magnitude of $10^{-4}\frac{m^2}{s}$, several orders of magnitude too large. In Ehrenfest simulations the excitation delocalizes rapidly, thus leading to vanishing contributions of the excited states forces, which is effectively the same as if there was no excited states relaxation at all. It is crucial that the simulated transport remains thermally activated. A localized exciton on a single molecule leads to a large structural relaxation, hence creating a potential trap from which escape is suppressed exponentially with a Boltzmann-like factor. The pace of diffusion is thus reduced by orders of magnitude. Therefore, artificial delo-calization invalidates simulations as soon as molecular relaxation does no more occur.

Surface-hopping and BC-Ehrenfest work better than the two simple approaches. In surface-hopping simulations the exciton moves around, strongly localized on single molecules at all

times (see e.g. Fig. 4.9). This means transport is decoherent, and thermally activated via hopping events, as could be expected due to the high reorganization energy and is also well established both experimentally and theoretically [12, 132, 144].It also implies that the assumption of similar adiabatic and diabatic states underlying the BC-Ehrenfest approach is justified. Systematic studies of the surface-hopping approach for charge transport have demonstrated its ability to describe spatial transport in organic crystals [141], even in the hopping regime, and, as exciton transport is formally equivalent and parameters are similar, this justifies the application for this purpose, too. We tried various values for the constant C in the expression for the decoherence time (Eq. 4.17), including the extremes $C = 0$ and $C \to \infty$ (i.e. no decoherence correction). The effect was small. Results changed by no more than 10%, less than the margin of error. Therefore, we report only the results with no decoherence correction. Often the inclusion of decoherence is very important, but it appears to have much less effect on transport in homogeneous molecular crystals, as has been noted before [141]. Further, one may not expect too strong an effect in the first place, because all average couplings exceed 1% of the relaxation energy [138].

BC-Ehrenfest, unlike surface-hopping, must eventually delocalize the wave-function like conventional Ehrenfest, because it still includes no decoherence to re-collapse the wave-functions once it extends over multiple molecules. Nevertheless, by enforcing correct Boltzmann statistics, not normally achieved without correction, we observe that this process becomes so slow, that the wave-function remains localized, and transport thermally activated, over at least 10ps, our longest simulation time. We use the initial regime of activated transport to derive diffusion constants. It has been demonstrated for model systems that mean-field approaches with correct Boltzmann statistics can yield accurate charge transfer rates, and diffusion shows hopping characteristics if the simulation is run for an appropriate time span [141]. The resulting diffusion constants are not exact, but the errors found in the sample study in the temperature range of 200K – 400K were lower than the error expectable from other sources like the crystal structure description and the electronic structure calculations. One particular problem with the cut-off approach is that transport is not described in equilibrium, because equilibrium is reached only after a certain amount of time has passed. Consequently, the values of all derived properties depend on the duration of the simulation with too short and long simulation times leading to poor results, even though we observed little variation with simulation time in the test calculations on anthracene. We derive diffusion constants from linear fits, as detailed below, and the results of such fits are insensitive to the fit range if the fitted data resembles closely a straight line. The extend to which the data dependence on time can actually be considered as linear can be used as a first criterion for the validity of a simulation. Further, to complement the direct analysis of diffusion, we also derive transfer rates from our method and derive diffusion constants from them. Thus, an error estimate can be obtained, whereas otherwise the validity of the results would be unclear.
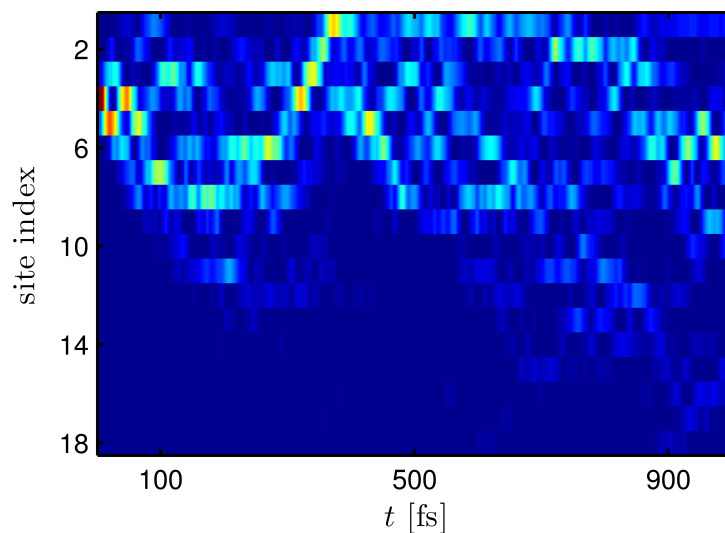
Figure 4.8: Sample trajectory of an exciton from a run with no relaxation forces. The exciton delocalizes almost immediately.
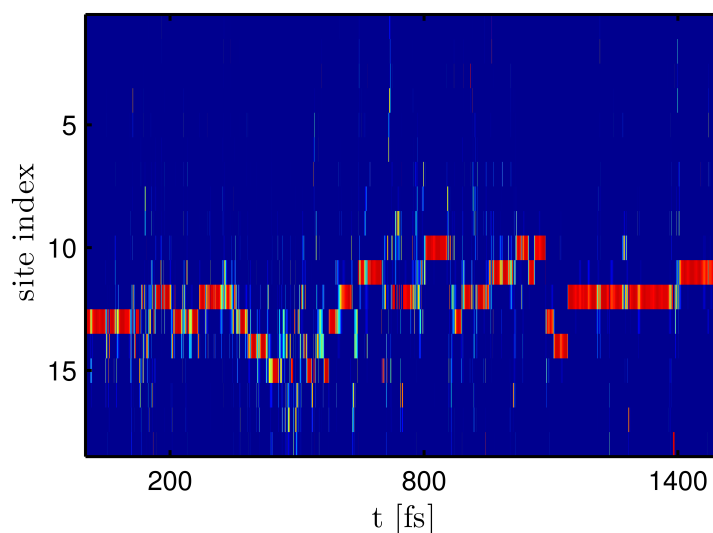

Figure 4.9: Sample surface-hopping trajectory. The exciton remains largely localized on a single molecule, though it is excited to more extended states for short times.

Analysis from direct-dynamics

In order to determine the diffusion coefficient D, quantifying transport efficiency, we consider the time evolution of the exciton location $x(t)$:

$$\sigma(t)^2 = \langle (x(t) - x(0))^2 \rangle \sim 2Dt. \tag{4.22}$$

The average of the square displacement $\sigma^2 = \langle (x(t) - x(0))^2 \rangle$, where x is the position operator in the studied direction, was taken over 160 trajectories, each with different initial conditions.
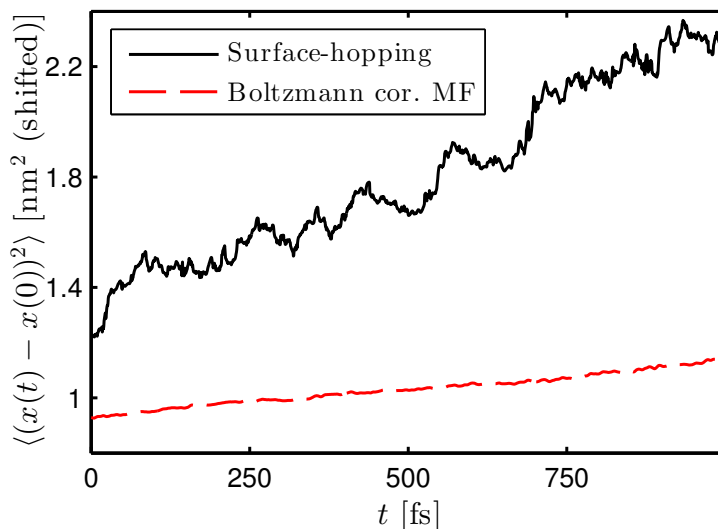
Figure 4.10: Evolution of the average mean square displacement of the exciton in time in the b-crystal direction, calculated with different methods.
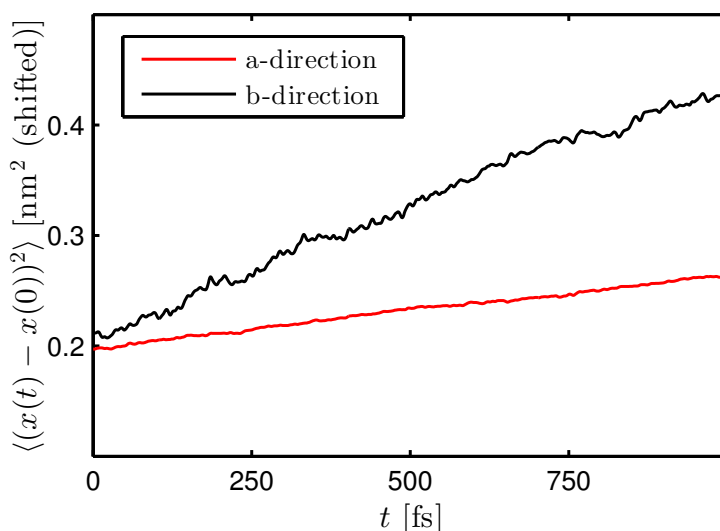
Figure 4.11: Evolution of the average mean square displacement of the exciton in time in the $a-$ and $b-$crystal directions, calculated with the Boltzmann corrected Ehrenfest method. Transport in the $b-$direction is roughly twice as fast.

Each trajectory was recorded over at least 4ps. Initial ballistic regimes were identified as regions with clearly non-linear behavior of the square displacement and cut off from the time series. Figures 4.10 and 4.11 show 1ps of the temporal evolution of $\langle (x(t) - x(0))^2 \rangle$ in the a, b directions for surface-hopping and BC-Ehrenfest. It is apparent by visual inspection that surface-hopping sampling is much worse than BC-Ehrenfest sampling. The latter is a mean-field approach and entails some averaging in each run explaining the smoother curves. In the slower a-direction we only report BC-Ehrenfest results because surface-hopping sampling becomes poorer as diffu-

sion slows down. In fact, the expected hopping rate as estimated a posteriori from the diffusion constant comes out as only a few hopping events per picosecond, meaning long simulations with surface-hopping are required. Many more trajectories could have been computed in principle and simulation times increased, but it did not appear reasonable as the mean-field approach seemed more natural for very slow transport. It may not be entirely correct, but should give the right picture, while the lower need for sampling we observed pays off very much and the assumption of fast thermalization implied in the use of a Boltzmann factor to rescale couplings is justified if the exciton rests on a molecule for many periods of molecular vibrations. The diffusion coefficient is determined from linear fits to the data. We find for surface-hopping and BC-Ehrenfest in b-direction $D_b = (8.4 \pm 4)10^{-7} \frac{m^2}{s}$ and $D_b = (2.4 \pm 0.2)10^{-7} \frac{m^2}{s}$, respectively (see Table 4.3). In a-direction diffusion is slower with $D_a = (5.5 \pm 2.5)10^{-8} \frac{m^2}{s}$ from surface-hopping and $D_a = (7.1 \pm 0.4)10^{-8} \frac{m^2}{s}$ predicted by BC-Ehrenfest. The errors are estimated from the statistical errors for each point $\langle (x(t) - x(0))^2 \rangle$ by the largest slopes compatible with the error bars. Since sampling is considerably worse, the error on the surface-hopping result is much larger. Within error range the values in a-direction agree, while in b-direction surface-hopping predicts somewhat larger diffusivity. From those values, we can also estimate the diffusion length L_D as $L_D = \sqrt{2D\tau}$ with an excitation life-time of $\tau = 10$ns [145]. The resulting diffusion lengths are $L_D = 37.6$nm in $a-$ and $L_D = 69.3$nm in $b-$direction.

Analysis from transfer rates

As explained earlier, the diffusion constants extracted directly from the simulations may not describe the equilibrium transport reliably. Therefore, we also extracted exciton transfer rates k from the trajectories as an extra validation of the BC-Ehrenfest results. Such rates still include fluctuations on time scales of up to about 1ps dynamically, while slower fluctuations are frozen and included as static disorder in the averaging over multiple trajectories. Thus, not all information about fluctuations is lost. In order to determine k, the function $a\exp(-kt) + b$ was fitted to the time evolution of the average population $\langle |c_0(t)|^2 \rangle$ of originally occupied sites

$$\langle |c_0(t)|^2 \rangle \sim a\exp(-kt) + b. \tag{4.23}$$

Eq. 4.23 should hold in the beginning, when only one site is occupied and all others unoccupied. Therefore, we fitted directly from the start of the simulations. The initial linear regime in $\ln\left(\langle |c_0(t)|^2 \rangle\right)$ was identified as the suitable fit range, as it indicates the time span over which eq. 4.23 is valid. With the so obtained transfer rates we performed Kinetic-Monte-Carlo [152] simulations of a random walk to simulate the time evolution of the exciton location. More precisely, at each step the exciton hops to the right with probability $p = \frac{1}{2}$ or to the left otherwise and the time is increased by $\Delta t = \frac{\ln(1/u)}{k}$, where u is random, uniformly distributed in between 0 and 1. Then, with a diffusion analysis identical to the treatment of the trajectories from

quantum-dynamics simulations, we computed the diffusion constants. The results are $D_a = 7.8 \cdot 10^{-8} \frac{\mathrm{m}^2}{\mathrm{s}}$ in a- and $D_b = 2.9 \cdot 10^{-7} \frac{\mathrm{m}^2}{\mathrm{s}}$ in b-direction. These values are slightly, but not significantly, larger than the ones obtained directly and support the use of the method.

Comparison to Marcus theory

For an assessment of the actual relevance of fluctuations we use the previously calculated reorganization energy $\lambda = 302\mathrm{meV}$ predicted by TD-DFTB together with the intermolecular excitonic couplings $J_a = 4.7\mathrm{meV}$, $J_b = 30.3\mathrm{meV}$ at the static, optimized geometry in the Marcus rate expression

$$k_{\mathrm{Marcus}} = J^2 \sqrt{\frac{\pi}{\lambda k_B T}} \exp\left(-\frac{\lambda}{4 k_B T}\right), \tag{4.24}$$

and the rates in Kinetic-Monte-Carlo simulations to yield diffusion constants unaffected by fluctuations. Marcus rates are probably closest in spirit to our semi-classical description, and are, therefore, a good choice. We find $D_a = 9.7 \cdot 10^{-9} \frac{\mathrm{m}^2}{\mathrm{s}}$ in a-direction and $D_b = 5.6 \cdot 10^{-7} \frac{\mathrm{m}^2}{\mathrm{s}}$ in b-direction. The diffusion constant in $b-$direction predicted by Marcus theory falls in between the surface-hopping and BC-Ehrenfest results. The fluctuations of the couplings in this direction are comparatively weak and lead only to a quantitative correction. Our method lacks the precision to accurately discern the subtle impact. On the other hand, in $a-$ direction, where fluctuations dominate the coupling, Marcus theory predicts a results smaller by a factor of five to about one order of magnitude. That is, by inclusion of fluctuations the ratio D_a/D_b increases about tenfold. Then, while transport in b-direction remains more efficient, diffusion lengths in both directions are of the same magnitude; transport appears as a two dimensional process in the ab-plane. Without fluctuations the picture is closer to one dimensional transport in the b-direction only. For the relative transport efficiency in different directions the effect of fluctuations is crucial, whereas the absolute values of diffusion constants may be more affected by effects such as molecular relaxation. An increase in the D_a/D_b ratio by a factor of about 7 after inclusion of fluctuations has been reported previously [12].

Implicit treatment of relaxation effects

As discussed in a previous section the use of DFT-GGA functionals leads to an underestimation of relaxation effects, i.e. to an underestimation of λ. In transition rate expressions, λ usually appears exponentially and therefore a seemingly small error can lead to large discrepancies in rates and hence diffusion constants. This merits a further investigation of the effect the underestimation of λ has on the results of the presented simulations.

So far relaxation was described by direct inclusion of exciton-phonon coupling via the forces $\mathbf{F}_{\mathrm{QM}}$ in eq. 4.14. In our early work on charge-transfer in DNA [90], intra-molecular relaxation was not treated explicitly by including forces like $\mathbf{F}_{\mathrm{QM}}$, but was included implicitly by a pre-
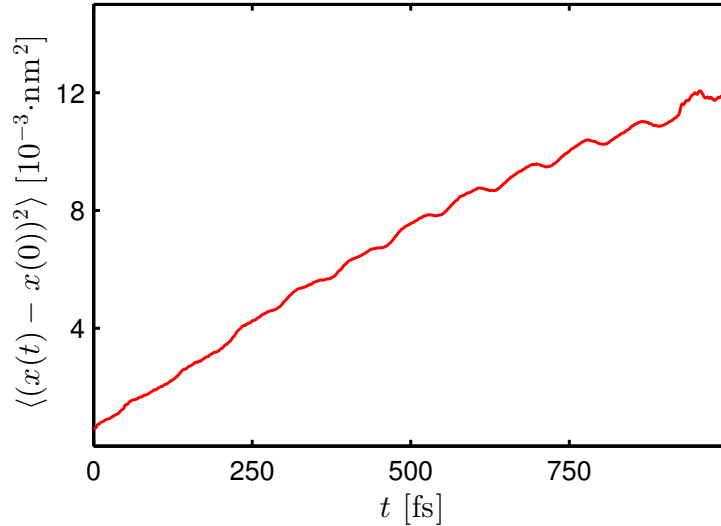
Figure 4.12: Evolution of the mean square displacement if exciton-phonon coupling is treated with a parameter.

calculated parameter, which can be added to the diagonal part of the Hamilton matrix. The same approach can also be used for exciton transfer, i.e. by subtracting the reorganization energy λ from the diagonal part of the Frenkel Hamiltonian. For an accurate estimate of λ, we use the coupled-cluster value $\lambda = 533 \text{meV}$ from Ref. [81]. That is

$$\tilde{H}_{II} = H_{II} - |c_I|^2 \lambda, \qquad (4.25)$$

with c_I the relevant wave-function component. On each site a potential well of depth $|c_I|^2 \lambda$ is created, the same way it would be by molecular relaxation, but with different depth. Thus, the reorganization energy parameter λ simulates molecular relaxation. This approach assumes an immediate relaxation through an infinitely fast mode. Because relaxation is indeed fast, occurring within about 10fs, the approximation should be reasonable. In addition, we also tried this approach with the value of $\lambda = 302 meV$ predicted by TD-DFTB and could reproduce the results with full forces to within an error of less than 5%.

Expecting a strong slow down of diffusion, only calculations with BC-Ehrenfest were performed. The diffusion coefficient in the b-direction reduces by one order of magnitude to $D = (1.09 \pm 0.1)10^{-8} \frac{\text{m}^2}{\text{s}}$. The diffusion length decreases to $L_D = 14.76 \text{nm}$. Precisely, diffusion is slowed down by a factor of 0.05. Marcus transfer rates, for comparison, suggest a slow down in line with this, by a factor of about $\exp\left(-\frac{\lambda_{\text{CC2}} - \lambda_{\text{DFTB}}}{4k_B T}\right) = 0.1$, where λ_{CC2} is the reorganization energy used as a parameter and λ_{DFTB} is the TD-DFTB value effective in the simulations with explicit forces.

Table 4.3: Diffusion constants D [$\frac{m^2}{s}$] from different methods and corresponding diffusion lengths L_D [nm] ($\tau = 10$ ns assumed).

Direction	D (BC-Ehrenfest)	D (surface-hopping)	L_D (BC-Ehrenfest)	L_D (surface-hopping)
a	$7.1 \cdot 10^{-8}$	$5.5 \cdot 10^{-8}$	37.6	33.2
b	$2.4 \cdot 10^{-7}$	$8.4 \cdot 10^{-7}$	69.3	129.6
Direction	D (KMC)	D (Marcus)	L_D (KMC))	L_D (Marcus)
a	$7.8 \cdot 10^{-8}$	$9.7 \cdot 10^{-9}$	39.6	13.93
b	$2.9 \cdot 10^{-7}$	$5.6 \cdot 10^{-7}$	76.1	105.8
Direction	D ($\lambda_I = 302$meV)	L_D ($\lambda_I = 302$meV)	D ($\lambda_I = 533$meV)	L_D ($\lambda_I = 533$meV)
b	$2.5 \cdot 10^{-7}$	70.71	$1.09 \cdot 10^{-8}$	14.8
Direction	L_D (exp. [144])			
a	60			
b	100			

Comparison to previous studies

Experimental values for L_D are $L_D = 60$nm in $a-$ and $L_D = 100$nm in $b-$direction [144]. Direct measurements of the diffusion constants yielded estimates of $D \approx 10^{-8} \frac{m^2}{s}$ or less in $b-$direction [143]. It is important to note that the directly estimated diffusion constants indicate diffusion lengths roughly one order of magnitude smaller than directly measured, and, thus, experiments are not entirely conclusive. All our calculate values fall into the range of experimental values yielding qualitatively correct predictions. With the BC-Ehrenfest predicted diffusion lengths –the most reliable values sampling wise, though not from the theoretical stand point– we find an anisotropy $L_{Da}/L_{Db} = 0.54$ in very good agreement with the experimental estimate $L_{Da}/L_{Db} \approx 0.6$. Generally, all methods which include fluctuations predict lower anisotropy than Marcus theory, in line with experimental results. The prediction of anisotropy may benefit from a cancellation of error not affecting absolute values. Rate expressions suggest a factorization of the transfer rate into a coupling dependent term and some exponential factor stemming from molecular relaxation. Then relaxation cancels from the D_a/D_b ratio and this should hold approximately true for the real-time dynamics as well. Many error contributions, such as the underestimated relaxation energy and erroneous delocalization because of missing decoherence, primarily affect the canceling exponential term. It is difficult to decide which are ultimately the best predictions. The use of a correct λ_I parameter, rather than forces, reduces the diffusion constant and hence brings results closer in agreement with the experiment where diffusion constants have been directly measured, but then diffusion length estimates deviate more

from the measured values.

A comparison to previous theoretical studies may point out a further source of error and help put results into perspective. Investigations of exciton diffusion in anthracene utilizing Marcus rates to calculate the hopping probabilities predicted slower diffusion than studies with rates based on the spectral overlap, but with otherwise similar parameters [81, 132]. The authors attributed the effect to the lack of multiple modes, rather than just one effective mode, in Marcus theory. When λ_I is used as a parameter in our simulations, we find diffusion constants in b-direction (where coupling fluctuations are not as dominant as in a-direction) of similar magnitude as obtained in these studies by Marcus theory. Certainly, though, all modes are included if the full classical dynamics of the nuclei is considered. We believe a classical treatment of all modes, common to our simulations and Marcus theory, is at fault for underestimating diffusion constants. The largest contribution to molecular relaxation in anthracene has been shown to stem from high frequency, quintessentially quantum-mechanical modes [12]. If this is taken into account, effective relaxation energies come out smaller than the actual value [12], further indicating a classical treatment of modes might not be entirely justified, and explaining the lower diffusivity predicted by approaches which treat modes classically. It would then so happen that the underestimated relaxation in a GGA-functional description provides a better classical approximation to the quantum mechanical treatment and, by cancellation of errors, the uncorrected results would be more accurate. Such an argument supports the results with larger diffusion constants, in line with the experimentally measured diffusion lengths .

4.4 Conclusion

In this chapter we introduced an approach where singlet exciton diffusion in anthracene was modeled by direct non-adiabatic coupled quantum-classical simulations. Since long time-scale simulations for relatively large quantum systems are required, a fragmentation approach was used where quantum calculations were performed for individual molecules with the fast TD-DFTB method and Coulomb-couplings were used to build the intermolecular Hamiltonian describing the exciton dynamics in the system. Tully's fewest switches surface-hopping, with adaptions for bulk systems, alongside the Boltzmann corrected Ehrenfest algorithm were applied to combine quantum and classical simulation. The latter has, to our knowledge, not been used before in transport simulations. Results with both algorithms agree reasonably well. We also tried to account for an underestimation of molecular relaxation due to the local functional underlying DFTB, by describing relaxation with a parameter, rather than with actual forces.

Our results for the diffusion constants D and diffusion lengths L_D in two different directions agree qualitatively well with experiment. Because results differ somewhat with different simulation setups and also because of different experimental results, a precise evaluation of the

methodology is difficult at the moment.

As it turned out, there are three issues adversely affecting the performance of the method. One is the failure of local functionals to accurately describe low-energy excited states in oligocenes. This could be remedied by using long-range corrected functionals. In fact, such functionals have recently become available in DFTB [17]. In the next chapter, the ground-state formalism is extended to TD-DFTB, and in future work we plan to combine this method with the exciton transport approach. Another issue is the neglect of exchange and overlap contributions to the excitonic coupling, resulting in too small fluctuations. The common approach to include them is via supermolecular calculations for dimers and diabatization schemes. While performance wise the higher computational cost could be stemmed, incorrect descriptions of non-symmetric dimers with local functionals render this impossible. Again, range-separated functionals in DFTB could solve this in the near future. Finally, the classical description of quantum modes seems to be a source of error. Applying path-integral methods for the nuclear dynamics may address this issue, but it is not clear whether this will provide a solution in quantitative terms. Research along this lines is currently underway in our laboratory.

On the upside, the method is able to make reasonable predictions at a low cost. This may be in part due to an error cancellation of relaxation and nuclear quantum effects. It would be interesting to explore in the future whether this can be used in a systematic way. The method can be used as a black box, while for example the calculation of spectral overlaps can require much human and computational effort. Direct MD trajectories of several picoseconds length with 18 molecules in the QM region can be performed within a day on a single core, making it about a 1000 times faster than the TD-DFT calculations presented in Ref. [11].

Because exciton transport in anthracene is incoherent, it is a challenging regime for real-time propagation methods and hopping models are the most appropriate approach. The current work suggests that this challenge can be met by direct simulations and as a main application, the method should be able to distinguish transport regimes without prior assumption. Materials where coherent transport takes place hold great technological promise and likely there are many borderline cases in between coherent and incoherent, where hopping models will fail. For the study of these systems the presented methodology can be a very useful tool, in particular since it can be used without the need to parametrize model Hamiltonian. Therefore we think that this approach can be a useful tool for the study of exciton diffusion in molecular materials.

5 Time-dependent extension of the long-range corrected DFTB method

5.1 Introduction

The methods presented in chapters 3 and 4 rely heavily on the DFTB method for electronic structure calculations. However, the electronic states relevant for charge and energy transport processes in anthracene and many other typical organic semiconductors are known to be poorly described by the PBE functional underlying DFTB.

A significant drawback of DFTB was the limited lexibility in terms of available exchange-correlation (xc) functionals. Only local and semi-local functionals like the LDA or gradient-corrected functionals could be used in the DFTB framework. This left the important class of functionals that incorporate Hartree-Fock exchange out of reach. On the DFT level, such global hybrid and long-range corrected (LC) functionals are widely and successfully used. Global hybrids, like B3LYP or PBE0, provide a balanced description of electronic and vibrational properties for a wide class of materials [153]. LC functionals effectively minimize the self-interaction error in DFT and overcome the trend for over-delocalization of the electron density typically found in local DFT approaches [154–160].

Through a complete reformulation of the DFTB derivation, the LC-DFTB method, which allows to incorporate arbitrary LC functionals in the DFTB context, has been developed by Niehaus et al. [17]. Benchmark calculations showed that the benefits of self-interaction minimized approaches, like improved quasiparticle energies and electric field response, are also obtained in LC-DFTB at strongly reduced computational cost. This motivates us to also extend the time-dependent (TD) formulation of DFTB, in order to access electronic excited states (LC-TD-DFTB). Beside improving the description of excitations in anthracene and many similar molecules [161], LC functionals are known to remedy the notorious underestimation of charge

transfer excited states in local and gradient-corrected TD-DFT [162]. This problem is especially pronounced for large distance intermolecular transitions but also for intramolecular excited states of extended and therefore large systems. In fact, this is exactly the typical domain of application for the DFTB method and hence there is a need for such a development. Efforts in this direction have already been undertaken by Humeniuk and Mitric [163]. Here we derive the time-dependent response consistently from the LC-DFTB Hamiltonian, which itself was derived directly from the LC-DFT energy functional earlier. The theory can also be seen as an extension of the TD-DFTB method [164], and we will often make reference to this earlier work to keep the presentation short. This section is followed by an extensive benchmark of excitation energy and oscillator strength predictions for a test set of small organic molecules. Then the method's ability to correctly describe charge-transfer excitations is investigated, as well as its description of the L_a, L_B excitations in polyacenes, where, in full DFT, long-range corrected functionals cope better than local or hybrid functionals. The polyacenes include anthracene, which provided the motivation for the extension of TD-DFTB in the context of this work. Finally, we analyze the computational efficiency of the method and close with conclusions.

5.2 Methodology

As discussed in section 2.1.2, electronic excited states and response properties are available in TD-DFT through the RPA equations [50, 165, 166]

$$
\begin{pmatrix} \mathbf{A} & \mathbf{B} \\ \mathbf{B} & \mathbf{A} \end{pmatrix} \begin{pmatrix} \mathbf{X} \\ \mathbf{Y} \end{pmatrix} = \Omega \begin{pmatrix} \mathbb{1} & 0 \\ 0 & -\mathbb{1} \end{pmatrix} \begin{pmatrix} \mathbf{X} \\ \mathbf{Y} \end{pmatrix},
\tag{5.1}
$$

where the eigenvectors $\mathbf{X}, \mathbf{Y}$ determine the transition density and oscillator strength of a certain excited state, while Ω denotes the associated transition energy. In the following we denote general molecular orbitals (MO) with the indices $p, q, \ldots$ occupied orbitals with indices $i, j, \ldots$ and virtual (unoccupied) orbitals with indices $a, b, \ldots$. We also introduce spin indices σ, τ, molecular orbital energies $\varepsilon_{p\sigma}$ and occupations $n_{p\sigma}$. The matrices $\mathbf{A}$ and $\mathbf{B}$ take the form [50]:

$$
\begin{aligned}
A_{ia\sigma,jb\tau} &= \frac{\delta_{ij}\delta_{ab}\delta_{\sigma\tau}\omega_{jb\tau}}{n_{j\tau} - n_{b\tau}} + K_{ia\sigma,jb\tau} \\
B_{ia\sigma,jb\tau} &= K_{ia\sigma,bj\tau},
\end{aligned}
\tag{5.2}
$$

where $\omega_{jb\tau} = \varepsilon_{b\tau} - \varepsilon_{j\tau}$ with $n_{i\sigma} > n_{a\sigma}$ and $n_{j\tau} > n_{b\tau}$. The coupling matrix $K_{ia\sigma,bj\tau}$ quantifies the linear response of the Hamiltonian due to a (electric field) perturbation and is defined as:

$$K_{ia\sigma,jb\tau} := \frac{\partial H_{ia\sigma}}{\partial P_{jb}^{\tau}}. \tag{5.3}$$

In order to assess excited states in the LC-DFTB method it is therefore sufficient to evaluate eq. 5.3 in the LC-DFTB framework. LC-DFTB has been introduced in section 2.1.3, and the most relevant parts are also briefly repeated in the following section. The Coulomb interaction is split as

$$v_C = v_C^{\text{sr}} + v_C^{\text{lr}} = \frac{\exp(-\omega r)}{r} + \frac{1 - \exp(-\omega r)}{r}, \tag{5.4}$$

with the range-separation parameter ω. The BNL functional [58, 59] is used for the short-range component, and non-local Hartree-Fock exchange for the long-range part.

In the LC-DFTB method the BNL energy functional is expanded around a reference density matrix $\mathbf{P}^{0,\sigma}$ up to second order in the fluctuations $\Delta\mathbf{P}^{\sigma} = \mathbf{P}^{\sigma} - \mathbf{P}^{0,\sigma}$, where $\mathbf{P}^{\sigma}$ is the desired solution at self-consistency. We are interested here in the Hamiltonian that arises from the energy expression. To ease the derivation of the coupling matrix, we first reformulate the original closed shell method in a spin-unrestricted form. We obtain (see section 2.1.3 or Refs. [17, 57]):

$$H_{\mu\nu}^{\sigma} = H_{\mu\nu}^{0,\omega} + \sum_{\tau}\sum_{\alpha\beta}\Delta P_{\alpha\beta}^{\tau}(\mu\nu|v_C + f_{\sigma\tau}^{\text{xc},\omega}|\alpha\beta)$$
$$- \frac{1}{2}\sum_{\alpha\beta}\Delta P_{\alpha\beta}^{\sigma}(\mu\alpha|v_C^{\text{lr},\omega}|\beta\nu), \tag{5.5}$$

where the superscript ω indicates a dependence on the range-separation parameter. In eq. 5.5 the Greek indices stand for the Slater type atom-centered basis functions ϕ_{μ} that have been defined in Ref. [17]. The term $H_{\mu\nu}^{0,\omega}$ denotes the zeroth order LC-DFTB Hamiltonian which is obtained by evaluating the BNL Hamiltonian at the reference density $\mathbf{P}^0$ in a two-center approximation [17]. The reference is simply the sum of density matrices at the BNL level of theory for all atoms in the system. In line with the spin-polarized implementation of DFTB [167], we chose the reference to be spin-restricted ($\mathbf{P}^{0,\uparrow} = \mathbf{P}^{0,\downarrow}$). We further introduced the following abbreviation for a general two-electron integral over a kernel $g(\mathbf{r},\mathbf{r}')$:

$$(f|g|h) = \iint f(\mathbf{r})g(\mathbf{r},\mathbf{r}')h(\mathbf{r}')\,d\mathbf{r}d\mathbf{r}', \tag{5.6}$$

where f and h stand for atomic orbital (AO) products, and g corresponds to v_C, v_C^{lr} or the exchange correlation kernel $f_{\sigma\tau}^{xc} = \delta^2 E_{xc}/\delta\rho_{\sigma}\delta\rho_{\tau}$, with ρ the electron density. Transformation

from the set $\{\rho_\uparrow, \rho_\downarrow\}$ to the total density $\rho = \rho_\uparrow + \rho_\downarrow$ and magnetization $m = \rho_\uparrow - \rho_\downarrow$ allows one to write [168]:

$$f^{xc}_{\sigma\tau} = f^{xc} + \delta_\sigma \delta_\tau \tilde{f}^{xc} \tag{5.7}$$

$$f^{xc} = \frac{\delta^2 E_{xc}}{\delta\rho\delta\rho}, \quad \tilde{f}^{xc} = \frac{\delta^2 E_{xc}}{\delta m \delta m}, \tag{5.8}$$

with $\delta_\sigma = 2\delta_{\uparrow\sigma} - 1$. In Ref. [17] expressions for the main required two-electron integrals were derived in the Mulliken approximation. Generally one finds:

$$(\mu\nu|g|\alpha\beta) \approx \frac{1}{4} S_{\mu\nu} S_{\alpha\beta} \left[(\mu\mu|g|\alpha\alpha) + (\mu\mu|g|\beta\beta) + (\nu\nu|g|\alpha\alpha) + (\nu\nu|g|\beta\beta)\right], \tag{5.9}$$

where $\mathbf{S}$ is the overlap matrix. Let l and m denote the angular momentum and magnetic quantum number of AO ϕ_μ, centered on atom A. We then have for $\mu = \{Alm\}$, $\nu = \{Bl'm'\}$:

$$(\mu\mu|v_C + f^{xc,\omega}|\nu\nu) \approx \gamma^{fr}_{Al,Bl'} \tag{5.10}$$

$$(\mu\mu|v^{lr,\omega}_C|\nu\nu) \approx \gamma^{lr}_{Al,Bl'}, \tag{5.11}$$

where $\gamma^{lr/fr}_{Al,Bl'}(|\mathbf{R}_A - \mathbf{R}_B|, U_{Al}, U_{Bl'})$ are functions that depend on the distance between the atoms on which the basis functions μ, ν are located and on the atomic Hubbard parameters U_{Al}. In order to approximate the remaining integral we follow Dominguez et al. [168]:

$$(\mu\mu|\tilde{f}^{xc}|\nu\nu) \approx \delta_{AB} W_{Al,l'}, \tag{5.12}$$

and introduce for later reference

$$\Gamma^{\sigma\tau}_{Al,Bl'} := \gamma^{fr}_{Al,Bl'} + \delta_\sigma \delta_\tau \delta_{AB} W_{Al,l'}, \tag{5.13}$$

with atomic constants $W_{Al,l'}$ that are already used in the conventional DFTB method for spin-polarized systems [167, 169]. These parameters, as well as atomic parameters entering the functions $\gamma^{lr/fr}_{\mu\nu}$, are evaluated using first principles BNL calculations. Note that eq 5.5 reduces to the spin-restricted result of Ref. [17] for closed shell systems. In this case the constants $W_{Al,l'}$ do not influence the ground state and only play a role for triplet excitations, as it will become clearer in the following. The generalized Kohn-Sham equations for spin-unrestricted LC-DFTB finally read:

$$\sum_\nu H^\sigma_{\mu\nu} c^\sigma_{\nu i} = \varepsilon_{i\sigma} \sum_\nu S_{\mu\nu} c^\sigma_{\nu i}. \tag{5.14}$$

Assuming real MO, the density matrix is then given by $P^\sigma_{\mu\nu} = \sum_i n_{i\sigma} c^\sigma_{\mu,i} c^\sigma_{\nu i}$.

Having defined the ground state Hamiltonian of LC-DFTB we are now in the position to derive the coupling matrix. Transforming from the AO to the MO basis by $H_{pq}^{\sigma} = \sum_{\mu\nu} c_{\mu p}^{\sigma} c_{\nu q}^{\sigma}$ we arrive at the central result:

$$K_{ia\sigma,jb\tau} = \sum_{AB}\sum_{ll'}\left(q_{Al}^{ia\sigma}\Gamma_{Al,Bl'}^{\sigma\tau}q_{Bl'}^{jb\tau} - \delta_{\sigma\tau}q_{Al}^{ij\sigma}\gamma_{Al,Bl'}^{\text{lr}}q_{Bl'}^{ab\tau}\right). \tag{5.15}$$

The terms $q_{Al}^{pq\sigma}$ have been denoted transition charges earlier [168, 170] and are evaluated according to

$$q_{Al}^{pq\sigma} = \frac{1}{2}\sum_{\mu\in A,l}\left(c_{\mu p}^{\sigma}\tilde{c}_{\mu q}^{\sigma} + c_{\mu q}^{\sigma}\tilde{c}_{\mu p}^{\sigma}\right), \quad \tilde{\mathbf{c}}_p = \mathbf{c}_p\cdot\mathbf{S}. \tag{5.16}$$

In the limit of a purely local or gradient-corrected functional ($\omega \to 0$) the contribution due to the long-range part in eq. 5.15 vanishes and one recovers the original TD-DFTB method [168, 170]. In the general case however, the long-range part introduces an asymmetry in the coupling matrix (e.g. $K_{ia\sigma,jb\tau} \neq K_{ia\sigma,bj\tau}$) similar to other DFT methods that feature non-local exchange. As a consequence, the eigenvalue problem (eq. 5.1) can not generally be recast into Hermitian form and one has to resort to specialized algorithms as given by Stratmann et al. [171].

After the solution, oscillator strengths f are readily available:

$$f = \frac{2\Omega}{3}\sum_{k=1}^{3}\left|\sum_{ia\sigma}\langle\psi_{i\sigma}|r_k|\psi_{a\sigma}\rangle\sqrt{(n_{i\sigma}-n_{a\sigma})}(X_{ia\sigma}+Y_{ia\sigma})\right|^2, \tag{5.17}$$

where r_k denotes the k-th component of the position operator. Like in conventional TD-DFTB [168, 170], the transition-dipole matrix elements are subjected to a Mulliken approximation:

$$\langle\psi_{i\sigma}|\mathbf{r}|\psi_{a\sigma}\rangle \approx \sum_{A}\mathbf{R}_A\left(\sum_{l}q_{Al}^{ia\sigma}\right). \tag{5.18}$$

5.3 Implementation details

The long-range corrected TD-DFTB method has been implemented in the development branch of the DFTB+ program [18] that already contains the ground-state method with long-range correction. In this section, we concretize some aspects of the method with respect to its actual implementation and focus on the excited state part of the calculation. For detailed information on the implementation of the ground state LC-DFTB method, we refer to the original publication [17].

In the previous section, the method has been introduced in a more general form than currently implemented. As in the original TD-DFTB method [170], we neglect the dependence of Hub-

bard parameters ($U_{Al} = U_A$) and spin constants ($W_{Al,l'} = W_A$) on the orbital angular momentum and evaluate them for the highest occupied atomic orbital only. The resulting coarsened functions γ_{AB} now describe the interactions between total atomic transition densities.

We further confine ourselves to closed-shell ground states, which reduces the dimensionality of the RPA equations by half. The orthogonal transformation through the matrix

$$\mathbf{M} = \frac{1}{\sqrt{2}} \begin{pmatrix} \mathbb{1} & \mathbb{1} \\ \mathbb{1} & -\mathbb{1} \end{pmatrix} \tag{5.19}$$

separates the RPA equations into independent eigenvalue problems for singlet and triplet excitations. With eliminated spin indices, the resulting coupling matrices read

$$K^S_{ia,jb} = K_{ia\uparrow,jb\uparrow} + K_{ia\uparrow,jb\downarrow}, \tag{5.20}$$

$$K^T_{ia,jb} = K_{ia\uparrow,jb\uparrow} - K_{ia\uparrow,jb\downarrow}, \tag{5.21}$$

where S and T refer to singlet and triplet excitations, respectively. The DFTB expressions then simplify to

$$K^S_{ia,jb} = \sum_{AB} \left(2 q^{ia}_A \gamma^{fr}_{AB} q^{jb}_B - q^{ij}_A \gamma^{lr}_{AB} q^{ab}_B \right), \tag{5.22}$$

and

$$K^T_{ia,jb} = 2 \sum_A q^{ia}_A W_A q^{jb}_A - \sum_{AB} q^{ij}_A \gamma^{lr}_{AB} q^{ab}_B, \tag{5.23}$$

with the total transition charges $q^{pq}_A = \sum_l q^{pq\uparrow}_{Al} = \sum_l q^{pq\downarrow}_{Al}$.

At this point, the eigenvalue problems to be solved are of dimension $2N_{occ} \times N_{virt}$, for N_{occ} occupied and N_{virt} virtual molecular orbitals. The form of the equations allows a further reduction of dimensionality by a factor of two. In purely local variants of TD-DFT and TD-DFTB the Casida equation [50] is usually employed:

$$(\mathbf{A} - \mathbf{B})^{1/2} (\mathbf{A} + \mathbf{B})(\mathbf{A} - \mathbf{B})^{1/2} \mathbf{T} = \omega^2 \mathbf{T}, \tag{5.24}$$

where $\mathbf{T} = (\mathbf{A} - \mathbf{B})^{-1/2}(\mathbf{X} + \mathbf{Y})$. This is a Hermitian problem. If the coupling matrix $K_{ia,jb}$ is invariant under exchange of j and b, $(\mathbf{A} - \mathbf{B})$ is diagonal, such that no actual matrix inversion is required. However, because non-local exchange destroys this symmetry, we work instead with the non-Hermitian form:

$$(\mathbf{A} - \mathbf{B})(\mathbf{A} + \mathbf{B})(\mathbf{X} + \mathbf{Y}) = \omega^2 (\mathbf{X} + \mathbf{Y}). \tag{5.25}$$

Usually, only a few low-lying excitations are of interest, not the entire spectrum. Algorithms solving only for a subset of eigenvalues are then typically employed, bypassing a full solution in the large space. For this purpose, we implemented the algorithm of Stratmann et al. [171], details of which can be found in the original publication. The evaluation of products of $(\mathbf{A} + \mathbf{B})$ and $(\mathbf{A} - \mathbf{B})$ with vectors of dimension $N_{virt}N_{occ}$ determines the scaling of the algorithm, implying $O(N_{virt}^2 N_{occ}^2)$ asymptotic scaling for first principles LC-DFT. In contrast, the special structure of the LC-DFTB coupling matrices allows to reduce the computational effort. Here, the matrix products can be written as

$$(\mathbf{A}+\mathbf{B})\mathbf{v} = \omega_{ia}v_{ia} + 4\sum_A q_A^{ia}\left[\sum_B \gamma_{AB}^{\text{fr}}\left[\sum_{jb} q_B^{jb}v_{jb}\right]\right] - \sum_{A,j} q_A^{ij}\left[\sum_B \gamma_{AB}^{\text{lr}}\left[\sum_b q_B^{ab}v_{jb}\right]\right]$$

$$- \sum_{A,b} q_A^{ib}\left[\sum_B \gamma_{AB}^{\text{lr}}\left[\sum_j q_B^{ja}v_{jb}\right]\right] \tag{5.26}$$

for singlets, and analogously for $(A - B)v$ and triplets. If the terms in the square brackets are precalculated and stored, the scaling improves to $O(N_{at} \cdot \max\left\{N_{occ}^2 N_{virt}, N_{virt}^2 N_{occ}\right\})$. This requires the storage of arrays of size $N_{at} \cdot \max\{N_{virt}^2, N_{occ}^2, N_{virt}N_{occ}\}$. For systems with many atoms much memory is required, but on modern computers this will likely only be an issue for very large systems. As an example, a model with thousand atoms requires about 64 GB of memory. In the present implementation the user one can select whether or not to precompute terms. All calculations presented in this work use the precomputation option. Thus, the method should asymptotically scale quartic with system size, whereas the conventional, local variant of TD-DFTB exhibits only cubic scaling.

5.4 Results

In the following, we apply TD-LC-DFTB in various test cases to assess the performance of the method. Electronic parameters (Hamiltonian, overlap and atomic parameters U_A, W_A) were computed with the range-separation parameter ω set to $\omega = 0.3/a_0$. This value provided accurate predictions of ionization energies and band gaps from orbital eigenvalues with the ground state LC-DFTB method [17]. The ground state calculations employ a prescreening with a threshold of $\varepsilon = 10^{-6}$ to decide whether Hamiltonian elements need to be calculated [17]. In DFTB, the density and wave function compression radii r_{d} and r_{wf} determine the shape of the reference density and the basis set, respectively [172]. Given that the range-separation changes both potential and resulting densities, optimal radii for the local and non-local variant of DFTB are not necessarily the same. Indeed, excitation energies turned out to be systematically overestimated if the conventional radii of the well established GGA parameter set *mio-0-1* [173] were

employed. Much better results were obtained by a homogeneous scaling of all radii by a factor of 0.8, independent of the element in question:

$$r_{\text{d/wf}} = 0.8\,r_{\text{d/wf}}^{\text{mio-0-1}}.$$

This scaling factor was chosen because it worked well for some sample molecules, but has not been thoroughly optimized up to now. With the reduced compression radii the gap between the highest occupied molecular orbital (HOMO) and the lowest unoccupied molecular orbital (LUMO) shrinks and orbital eigenvalues are lowered. Hence, predictions of ionization potentials and band gaps computed with the new parameters are slightly worse than reported in the original study [17], although this effect is small with changes of usually less than 5%. It is conceivable that by error cancellation the smaller orbital gaps correct for an underestimation of the response in the TD-DFTB approximations as the magnitudes of these two terms have opposite effects on excitation energies. In any case, it is not surprising that a change in the form of the DFTB Hamiltonian requires adapted parameters. Indeed, the long-range exact exchange contributions considerably increase the magnitude of the Hamiltonian elements. In addition, decreased compression radii correspond to a more compact density and the need for rescaling may be a consequence of a reduced self-interaction due to exact exchange. Ultimately, the method will work best with an adjusted, new parameter set, but this is beyond the scope of the present work and unnecessary for a first benchmark.

5.4.1 Small molecule test set

We benchmarked the accuracy of TD-LC-DFTB for the prediction of singlet excitation energies of typical, medium-sized organic chromophores. For this purpose, we selected the molecules in the benchmark set proposed by Thiel and co-workers [174]. Results for large benchmark sets give a good overall impression of the accuracy of the method. Calculations were performed directly on the geometries provided by Thiel et al., which they optimized at the MP2/6-31G* level. Besides LC-DFTB, we also ran calculations with conventional DFTB (*mio-0-1* parameters), LC-ωPBE [175]/6-31(d,p), and two additional long-range corrected DFT functionals, CAM-B3LYP [176] and ωB97X [177]. Because the latter two functionals and LC-ωPBE gave similar results with relative differences well below the error of LC-DFTB, their results are not presented. The full DFT calculations were carried out with the 09 version of *Gaussian* [178], and we kept the default value of $\omega = 0.4/a_0$ for LC-ωPBE.

We calculated the five lowest singlet excitations with each method and and classified the states according to symmetry in order to account for differing energetical order. DFTB results are not reported if there were no excitations among the five lowest that match the corresponding states predicted by LC-ωPBE. Our own calculations are complemented with CC3/TZVP and best estimates from the literature [174], available for some of the systems. These best estimates are

based on various high-level calculations and molecule specific assessments. Figure 5.1 provides a graphical representation of the results, while several comparisons of the mean average error (MAE) can be found in Tab. 5.1 (a detailed list of all results is found as Tab. A1 in the appendix). The MAE of DFTB based methods compared to LC-ωPBE decreases from 1.01 eV with DFTB to 0.44 eV with LC-DFTB. A steep drop in this error is expected, because LC-DFTB should resemble full DFT with long-range corrected functionals. Nevertheless, even if the tight-binding approximations were perfectly valid, the difference would not vanish as the the underlying functionals are not exactly the same. Compared to the best estimates, both DFTB methods and full DFT perform almost equally well on average, with MAEs of about 0.5 eV. This is due to the known tendency of long-range corrected functionals to overestimate many excitations in the test set [179], so that functionals without exact exchange, such as PBE (and by the same token DFTB) yield better accuracy. To analyze the performance of LC-DFTB in cases where long-range corrected DFT does indeed provide the better description, it is illustrative to look at the MAEs against the best estimates taken only over excitations where LC-ωPBE does at least outperform DFTB. Then we find MAEs of 0.73 eV for DFTB, 0.28 eV for LC-DFTB, and 0.21 eV for LC-ωPBE. Clearly, LC-DFTB yields much better results than DFTB for such excitations. In fact, on average LC-DFTB is almost as accurate as LC-ωPBE. A closer inspection of the individual results relativizes this somewhat. Trends can best be seen in the graphical representation given in Figure 5.1. Compared with LC-ωPBE, LC-DFTB fares worst for the molecules ranging from ethene to norbornadiene. Those are small linear or non-planar cyclic molecules, and higher lying excitations are described worse than lower lying excitations. LC-DFTB tends to underestimate the LC-ωPBE excitation energies, which could be due to the minimal basis set which can hardly describe high-lying and diffuse excited states. On the other hand, LC-ωPBE calculations with small basis sets, such as STO-3G or 3-21G, overestimate the excitation energies, questioning this assumption. In any case, given that LC-ωPBE overestimates the higher excitations, the MAE of LC-DFTB and LC-ωPBE with respect to high-level methods are actually quite similar due to error cancellation.

In contrast, LC-DFTB performs very well for the molecules ranging from benzene to tetrazine, which are planar, cyclic molecules, some containing nitrogen. There the MAE compared to LC-ωPBE is much smaller than the overall error of 0.4 eV. Finally, for the RNA bases cytosine to adenine LC-ωPBE predicts much larger excitation energies than DFTB. The bases are a difficult case for local functionals, with many excitations strongly underestimated by functionals such as PBE [179]. LC-DFTB follows the trend of LC-ωPBE, also predicting much higher values, albeit not reaching quite as high for some excitations.

Besides excitation energies, we also analyzed the oscillator strengths f. The oscillator strengths of the brightest excitation among the five lowest are shown in Figure 5.2 for each molecule in the test set. All oscillator strengths with $f > 0.01$ as calculated with LC-ωPBE, DFTB and LC-DFTB can be found in Tab. A2. Long-range correction usually increases the magnitudes

Figure 5.1: Singlet excitation energies for molecules in the benchmark set as predicted by time-dependent LC-DFTB, conventional DFTB with *mio-0-1* parameters, and other methods. Coupled-cluster results and best estimates are taken from Ref. [174]. Where DFTB values are missing, excitations corresponding to the five lowest states predicted by LC-*ω*PBE were not present. Curves belonging to different excitations have been shifted vertically for better overview.
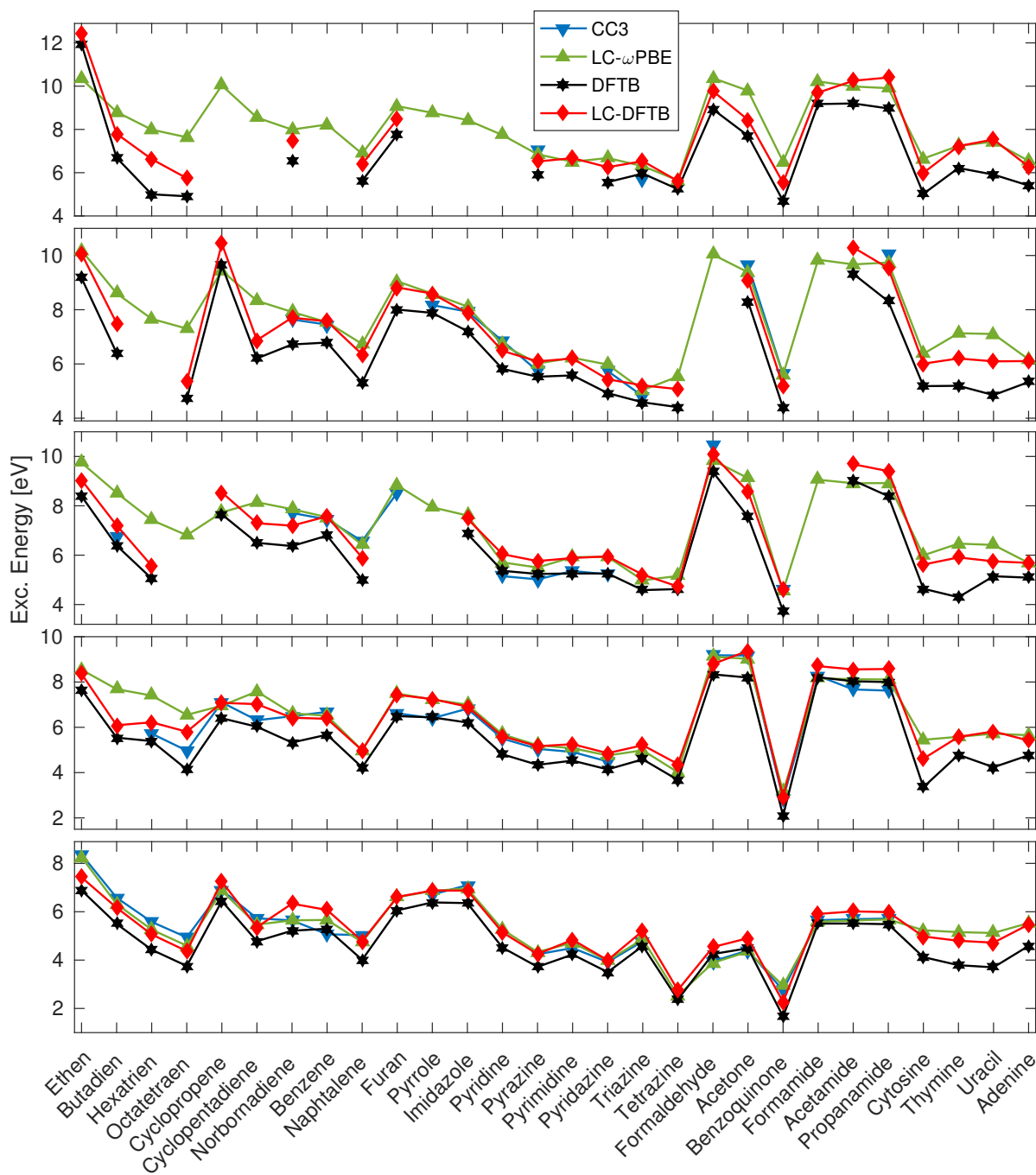
MAE vs. LC-ωPBE	
DFTB	1.01
LC-DFTB	0.44
MAE vs. CC3	
DFTB	0.64
LC-DFTB	0.43
LC-ωPBE	0.33
MAE vs. best est.	
DFTB	0.51
LC-DFTB	0.47
LC-ωPBE	0.46
CC3	0.24
MAE vs. best est. (where error LC-ωPBE < error DFTB)	
DFTB	0.73
LC-DFTB	0.28
LC-ωPBE	0.21
CC3	0.20

Table 5.1: MAE [eV] for the first five excitations (where values present) for different comparisons. CC3 and best estimates from Ref. [174].

of the predicted oscillator strengths and, indeed, LC-DFTB predicts larger values than DFTB for all excitations. LC-DFTB results are generally in very good agreement with LC-ωPBE; most relative errors are below 5%. For the hydrocarbons, furan and benzoquinone, LC-DFTB and LC-ωDFTB oscillator strengths match well, with varying, sometimes large differences to DFTB. This applies also for the small molecules, where excitation energies were often underestimated, even though the bright excitations happen to be the ones were the errors in excitation energy are also rather small. For the aromatic nitrogen compounds all methods predict small oscillator strengths, except for pyrrole, where LC-DFTB and LC-ωPBE are in good agreement. For the RNA bases, LC-ωPBE predicts values about twice as large as DFTB. While LC-DFTB and LC-ω agree well for uracil and adenine, the LC-DFTB results are too small for the other two bases, albeit larger than the DFTB results. Lastly, for all the molecules containing acyl groups, except for benzoquinone, LC-DFTB tends to overestimate the LC-ωPBE oscillator strengths. Noting that even DFTB overestimates the values, this points to a problem either with the tight-binding approximation or the minimal basis set. Overall, averaged over all of the five lowest
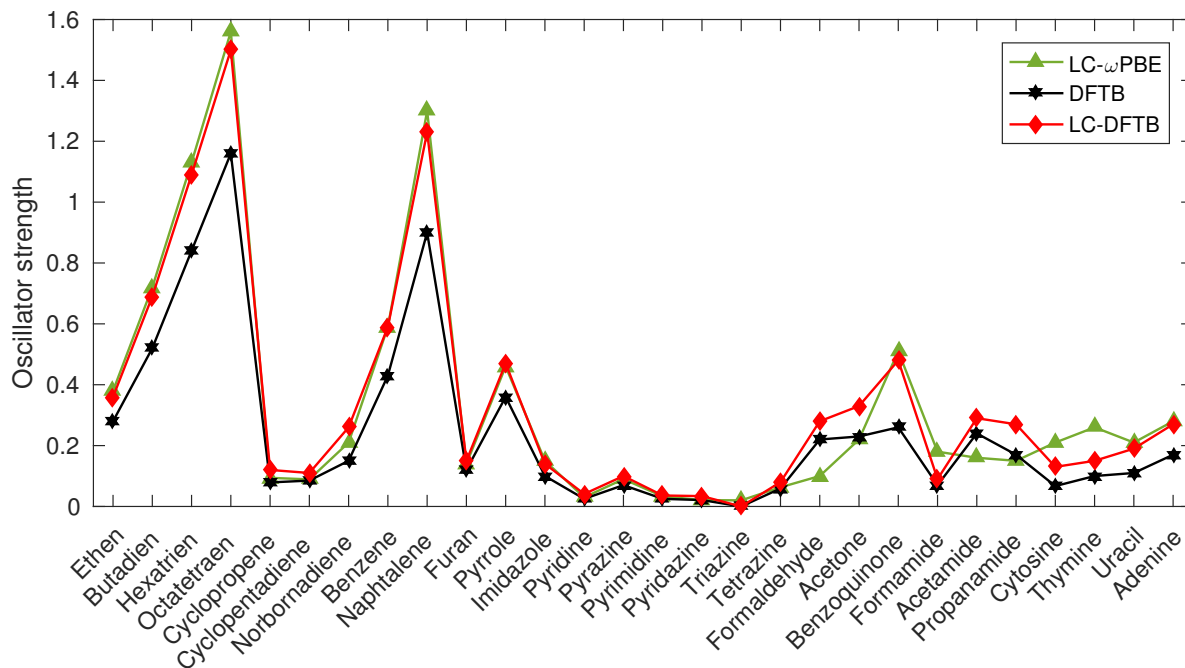
Figure 5.2: Oscillator strengths of the brightest excitation among the five lowest computed for different methods.

excitations and all molecules in the set, the MAE of the oscillation strengths with respect to LC-ωPBE decreases from 0.08 for DFTB to 0.04 for LC-DFTB.

5.4.2 Charge-transfer excitations

One of the most common applications of long-range corrected functionals is the treatment of charge-transfer (CT) excitations, which are wrongly described by functionals containing no or a fixed amount of Hartree-Fock exchange. Naturally, CT excitations are also an important potential application for LC-DFTB. In this section, we investigate whether the method can properly describe such states. A prototypical case of CT excitations can be found in dimeric molecular complexes where both molecules in the dimer are mostly neutral in the ground state, but upon excitation, an electron is transferred from one molecule to the other. For large intermolecular separations R, the excitation energy Ω_{CT} should be [180]

$$\Omega_{CT} = \text{IP(Donor)} - \text{EA(Acceptor)} - \frac{1}{R},$$

where IP is the ionization energy, EA the electron affinity, and the last term is due to the Coulomb interaction of the electron-hole pair. Local/semi-local DFT fails to predict the $-1/R$ term because the response is exchange like, while Hartree-Frock and long-range corrected DFT [181] yield the correct behavior. To test whether LC-DFTB exhibits the correct scaling with distance, we start by considering an ethylene$\cdots$tetrafluorethylene dimer, as proposed by Head-

Gordon et al. [162]. Figure 5.3 shows the dependence of the first excitation energy on the intermolecular distance for LC-DFTB, LC-ωPBE/6-31(d,p), and B3LYP/6-31(d,p). All curves where shifted to coincide at $R = 5\,\text{Å}$. LC-DFTB clearly exhibits the correct $1/R$ behavior, while B3LYP, as expected, does not. Therefore, also in tight-binding approximation the exact exchange term fully cancels the self-interaction in the limit of large separations as it should.

Next, we want to benchmark the quantitative performance of LC-DFTB for CT excitations. We follow Baer et al., who considered CT excitation complexes of tetracyanoethylene (TCNE), which serves as the acceptor, with various organic donor molecules [181]. Their B3LYP/cc-PVDZ optimized structures have been directly used for our computations. Results of the LC-DFTB calculations for the lowest excitations are shown in Figure 5.4 and Tab. A3, alongside experimental references [182, 183]. Tab. 5.2 contains MAEs against experiment over the test set. As theoretical references, we include TD-DFT results obtained with LC-ωPBE/6-31(d,p) and results from Baer et al. computed with B3LYP and a tuned BNL range-separated functional [181]. Within the tuned approach, the range parameter ω is optimized so that the HOMO energy of the TCNE-Benzene complex is as close as possible to its ionization potential value. Additionally, we compare our results to a simplified particle-particle random phase approximation (pp-RPA) formalism using DFTB eigenvalues and eigenfunctions [184]. Pp-RPA has recently proven as a promising tool for the study of CT excitations in atomic and molecular systems [185, 186]. It is based on the pairing matrix fluctuations and uses a $N - 2$ electron single-determinant reference, thus giving access to the ground and excited states of the N electron system through two-electron addition processes. The method describes correctly Rydberg, double and CT excitations and it has a similar computational cost as TD-GGA or TD-LDA. A series of approximations can be applied within the pp-RPA scheme to avoid the on-the-fly computation of two-electron integrals. The combination of these approximations with the DFTB calculation of the $N - 2$ reference leads to a computationally efficient, yet fairly accurate framework for the computation of CT energies. Since this method (so called pp-DFTB) employs DFTB orbitals and energies, as well as contains the same sort of approximations applied in LC-DFTB, it is interesting to include pp-DFTB CT energies here for comparison.

The failure of B3LYP is immediately obvious, as it vastly underestimates most excitations and describes trends incorrectly because the CT nature of the excitations is not accounted for. All other methods, including LC-DFTB and pp-DFTB, yield much better results and correct trends. Much smaller MAEs, on the order of 0.2 to 0.3 eV for LC-ωPBE, LC-DFTB, and pp-DFTB, or 0.1 eV for BNL, reflect this.

LC-DFTB and LC-ωPBE agree well with each other, but tend to systematically overestimate all excitation energies. The overestimation is likely caused by a poorly tuned range parameter ω. The tuned BNL results are closer to experiment and show no systematic deviation. Indeed, fine-tuning was found to be necessary for such good quantitative performance [181] with BNL. To investigate whether LC-DFTB results improve with a better chosen range parameter, we have
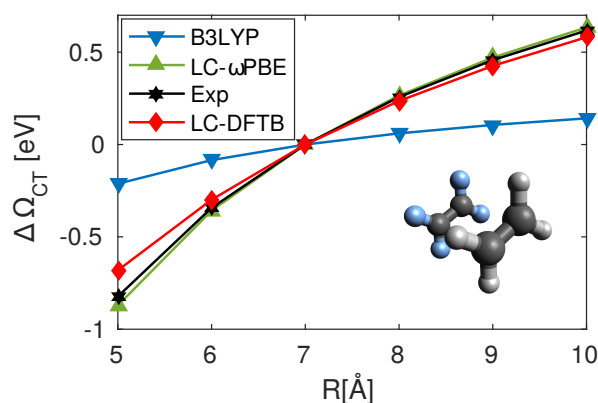
Figure 5.3: CT excitation energies in an ethylene$\cdots$tetrafluoroethylene dimer with various methods. Curves have been shifted to coincide at $R_0 = 7\text{Å}$, that is the quantity $\Delta\Omega_{CT} = \Omega_{CT}(R) - \Omega_{CT}(R_0)$ is shown for each method. LC-ωPBE and LC-DFTB exhibit the correct $-1/R$ scaling with distance, while B3LYP does not.

recalculated the excitation energies with a range parameter of $\omega = 0.25/a_0$, rather than the default $\omega = 0.3/a_0$ used for all other calculations. We did not arrive at that value by fine-tuning, which for lack of spin polarization parameters we can not do at the moment, although it is possible in principle. Rather, we chose the value heuristically, as decreases in ω also lead to decreases in the excitation energies and thus should lower the error. With the changed parameter, LC-DFTB reproduces the experimental results very well. The overestimation is eliminated and the MAE drops to 0.07 eV, the smallest of all methods. Notably, LC-DFTB then predicts very good results for methyl- and dimethylanthracene, whereas BNL overestimates the excitation energies. Seeing that the full DFT methods tend to predict larges values than the corresponding DFTB methods, this suggest that for those to molecules a fortuitous cancellation of error with the error due to the tight-binding approximation improves the results.

The accuracy of pp-DFTB is comparable to that of LC-DFTB without parameter fine-tuning. However, excitation energies tend to be under-, rather than overestimated, lending further support to the suspicion that the overestimation with $\omega = 0.3/a_0$ is caused by the choice of range parameter, not by the tight-binding approximation. The pp-DFTB excitation energies have an outlier at o-xylene that does not appear with LC-DFTB, pointing to a problem with the pp-RPA approximation for this molecule.

Ultimately, the data shows clearly that LC-DFTB can account for the CT nature of excitations and therefore be a tool to study them.

5.4.3 Excitations in polyacenes

Now we look at the much mentioned excitations involving large π states that were brought up as a motivation for the work in this chapter. Many organic semiconducting materials consist of
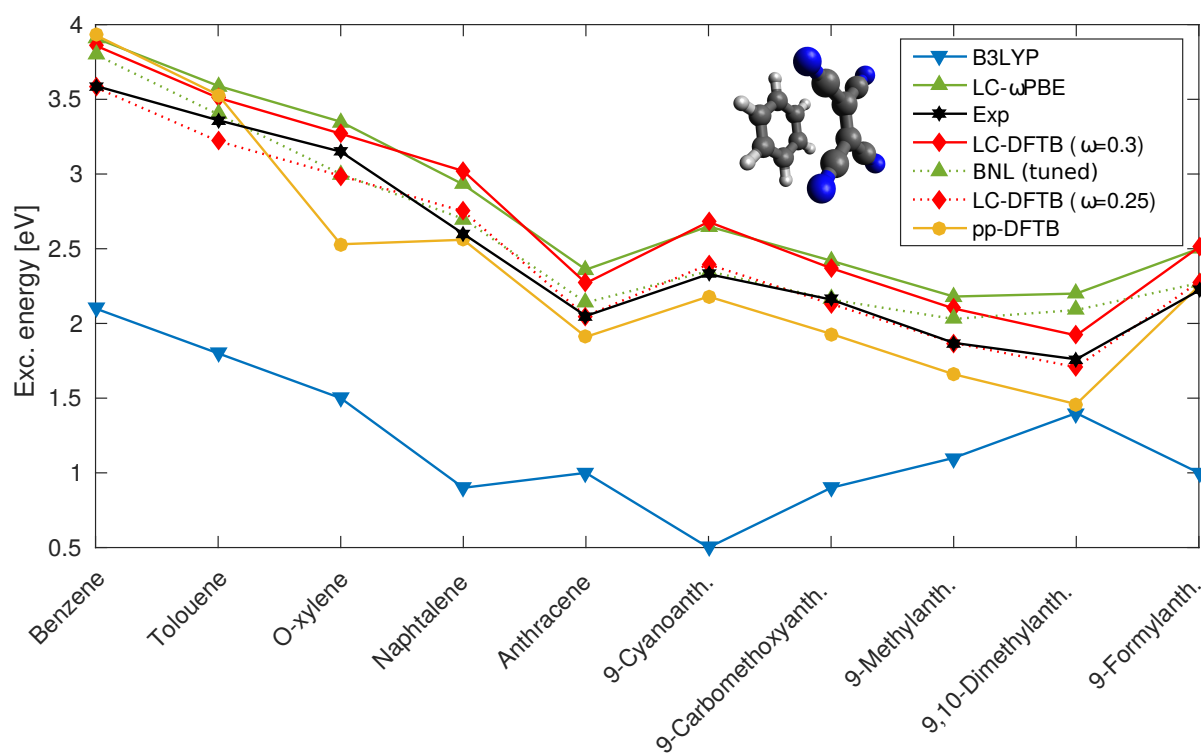
Figure 5.4: CT excitation energies in dimer complexes of TCNE with different molecules. Experimental results (in the liquid phase for the first three molecules and in the gas phase for the rest) have been taken from Refs. [182, 183], B3LYP results from Ref. [181].

	B3LYP [181]	LC-ωPBE	LC-DFTB ($\omega = 0.3$)	LC-DFTB ($\omega = 0.25$)	pp-DFTB	Tuned-BNL
MAE	1.20	0.30	0.24	0.07	0.22	0.12

Table 5.2: MAEs [eV], compared with experiment [182, 183], for the lowest CT excitation energies in dimers of TCNE with various molecules, as computed with different methods.

π-conjugated molecules, which for this reason are of great practical interest for the design of organic semiconducting devices. The polyacenes are an exemplary class of molecules exhibiting conjugation, and in pure crystals, charge mobilities can reach as high as several $cm^2/V \cdot s$ [15, 187], making them interesting for applications and as benchmark systems. The molecule anthracene from the previous chapters is one of the smaller polyacenes, with three rings. As stressed before, the treatment of such molecules is challenging for TD-DFT methods. Specifically, local and hybrid functionals underestimate the L_a excitation [188], the lowest singlet excitation with B_{2u} symmetry. In chapter 4 we saw that DFTB inherits this error from PBE. The error grows with the number of rings, so that progressing through the acenes series true value and prediction diverge further from each other. When the exchange contribution in hybrid functionals is increased, the error decreases, but then the L_b excitation, singlet of B_{3u} symmetry, is described worse. It has been demonstrated that long-range corrected functionals substantially improve the description of both states at the same time. This circumstance has been attributed to "CT excitations in disguise" [161], sharing some characteristics with true CT excitations. To investigate the performance of LC-DFTB in the description of the L_a and L_b excitations, we performed LC-DFTB, LC-ωPBE/6-31(d,p), and B3LYP/6-31(d,p) calculations on the acene molecules from naphtalene to heptacene. The molecular geometries were optimized in the ground state at the DFTB level. The observed trend with growing ring number can be seen in Figure 5.5. LC-DFTB correctly reproduces the full long-range corrected DFT and experimental behavior. Therefore, it can account for the factors rendering the polyacenes a difficult case for DFT methods. Exact values are listed in Tab. A4. The long-range corrected methods overestimate the L_b excitation energies and LC-DFTB slightly more than LC-ωPBE. It is, however, possible to improve the numerical agreement for long-range corrected functionals by fine-tuning the range-separation parameter ω [181]. The same should hold for LC-DFTB since it appears capable of describing the relevant physics.

5.4.4 Computational efficiency

DFTB is chosen over DFT when the computational requirements of a full DFT treatment of the problem at hand become excessive. Accordingly, good computational performance, as offered by the conventional DFTB method, is paramount for the usefulness of LC-DFTB. To benchmark the computational efficiency of the method, we performed calculations on a growing cluster of anthracene molecules in the herringbone arrangement of the bulk crystal. The ten lowest singlet excitation energies were computed for each configuration. Besides our LC-DFTB implementation, calculations were also run with the conventional linear response DFTB implemented in *DFTB+*, and with *NWCHEM* [190] (version 6.6) to perform LC-ωPBE/6-31(d,p) calculations. All jobs ran on a single core of an Intel Xeon E5-2630v3 processor, and except for system processes, no other jobs were active at the same time. Wall times, determined with the UNIX time
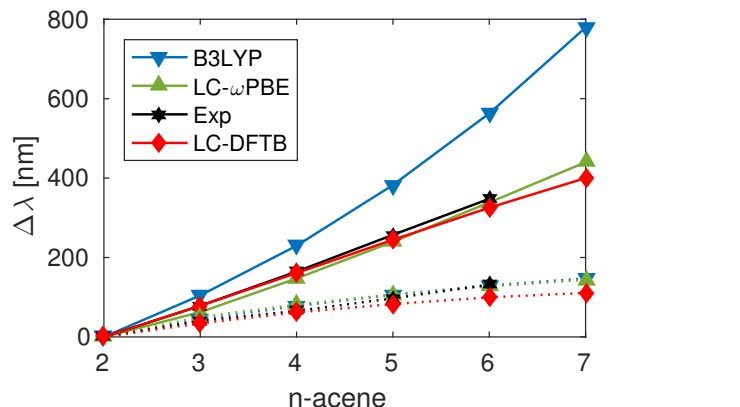
Figure 5.5: Energies of the L_a (solid lines) and L_b (dashed lines) excitations in the acenes series in terms of the wavelength of absorption $\lambda = \frac{hc}{\Omega}$. n-acene contains n benzene rings. Experimental results from Ref. [189]. Curves were shifted vertically to coincide for naphtalene, that is we plot $\Delta\lambda = \lambda_n - \lambda_2$. LC-DFTB and LC-$\omega$PBE reproduce the experimental trend, whereas B3LYP increasingly underestimates the L_a excitation.

utility, are displayed in Tab. A5 and plotted in Figure 5.6. Run times divided by the number of matrix-vector multiplications performed are also included for the DFTB calculations. All DFTB results have been averaged over five runs. Because we only allowed run times of up to two days, no *NWCHEM* results are available beyond a system size of 4 anthracene molecules. Note that for the two largest systems actually 15 excitations had to be computed with conventional DFTB, because the algorithm would not converge for 10, instead requesting a larger number of roots to solve for.

LC-DFTB turns out to be about three orders of magnitude faster than full LC-DFT. Such a speed-up permits the treatment of much larger system sizes, or a greatly increased number of single-point calculations, for example in molecular dynamics simulations. Surprisingly, LC-DFTB also runs almost as fast as conventional DFTB for all system sizes, despite its less favorable nominal scaling (see section section 5.3). Indeed as expected, a single matrix-vector multiplication of the kind of eq 5.26 takes much less time in the local formalism. The observed run time divided by the number of executed matrix-vector multiplications scales as $O(N^3)$ with system size N for conventional DFTB. For LC-DFTB we see a crossover from $O(N^3)$ scaling to the theoretically predicted $O(N^4)$ scaling. The cubic scaling can be attributed to the time required to setup the initial subspace that becomes insignificant for larger systems. While the performance for individual multiplications differs, the overall performance is almost the same. This happens because the conventional DFTB implementation executes about a hundred times more matrix-vector multiplications. Unlike the specific Stratmann algorithm implemented for LC-DFTB, the Arnoldi algorithm [191] currently used in *DFTB+* is generic, and apparently less efficient for the solution of the RPA equations. These results are in full agreement with
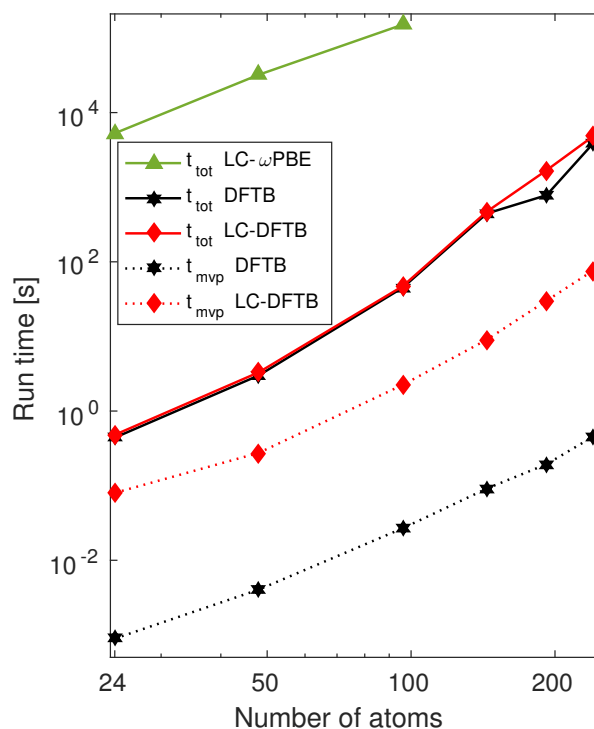
Figure 5.6: Run times (t_{tot}) for the calculation of the ten lowest singlet excitations in a growing anthracene crystal for different methods. For the DFTB based calculations, computation times per matrix-vector product (t_{mvp}) are also given.

the findings of Stratmann et al. [171] at the level of full DFT. In any case, the performance of LC-DFTB for reasonable system sizes turns on par with the current linear response DFTB implementation in *DFTB+*. This means that LC-DFTB should be applicable in most of the fields where DFTB is currently used with out significantly increasing the computational requirements.

5.5 Conclusion

We have presented an implementation of linear response DFTB with an underlying long-range corrected functional. The method builds on top of a fully consistent LC treatment of the ground state. This sets it apart from a previous, more empirical variant of TD-LC-DFTB. [163] Benchmark calculations were presented for various systems in which long-range corrections may be usefully employed. Good quantitative performance was found for molecules in a test set containing small chromophores, particularly for flat, cyclical molecules. It has been demonstrated that the method can treat charge-transfer excitations correctly and handle the L_a, L_b excitations in polyacenes. Therefore, we can expect LC-TD-DFTB to be useful in the context of charge and energy transport simulations based on DFTB. Oscillator strengths were likewise found to be in excellent agreement with full DFT calculations. Hence, also for excited states, LC-DFTB

offers a solution in cases where conventional DFTB fails due to the underlying GGA functional. In terms of computational efficiency, LC-DFTB is slower than DFTB, but as it was revealed, not by much compared to the current implementation in DFTB+. Here the proper choice of an adapted algorithm plays a crucial role.

During this study, we also found that the compression radii for density and wave function that are typically used in DFTB can not directly be taken over to LC-DFTB without compromising the accuracy. In the future, an automatic determination of these parameters along the lines proposed by Heine and co-workers [56] seems to be promising. It will be interesting to see if and to what extent the range-separation parameter ω can be varied without a need to adopt the compression radii, too. Certainly, every change in ω requires a reparametrization of DFTB. Electronic parameters are easy to calculate and sufficient for single point calculations, but refitting repulsive potentials, required for full potential energy surfaces, is more laborious, an aspect addressed in the next chapter.

Finally, it is noteworthy that there is nothing in the formalism and implementation of LC-DFTB that would prevent the inclusion of full-range exact exchange. As the same is true for the ground-state formalism, an extension to hybrid functionals such as B3LYP is straightforward from this point.

6 Generalized DFTB repulsive potentials from unsupervised machine learning

6.1 Introduction

The LC-DFTB method from the previous chapter adds a new parameter, the range-separation parameter ω. ω does in principle depend on the system at hand and should therefore be fine-tuned system specific. However, every new value of ω requires a reparametrization of DFTB. Electronic parameters are straightforward to calculate, but the repulsive potential terms traditionally require much manual effort, handpicking a training set of a few reference data points that generalizes well. In this chapter, we introduce a scheme for automatized repulsive potential paramterization. In doing so, we try be innovative, also tackling other limitations of the existing approach, by combining DFTB with unsupervised machine learning methods.

DFTB in recent years has seen major improvements in accuracy concerning covalent [192–194] and non-bonding interactions [195]. Despite those improvements, it seems the method has reached its limits due to its inherent inflexibility to reflect all chemical situations with its relatively fixed current form. For example, heats of formations and reaction energies for standard test sets show errors of 3-7 kcal/mol, depending on the focus of the parametrization strategy. The repulsive potentials, which are one part of the DFTB total energy, are already determined in a fitting procedure and can be based completely on empirical data or quantum chemical calculations. The other part of the total energy, the electronic terms, can be completely computed from DFT, traditionally using GGA functionals, or long-range corrected functionals for the new LC-DFTB formalism [17] (sec. 2.1.3 and chap. 5). With the availability of large amounts of reference data, data driven approaches become interesting alternatives to physical model potentials and approximate solutions of the Schrödinger equation. Lately, artificial intelligence techniques have become increasingly popular in molecular modeling, quantum chemistry, and condensed matter physics [196–201]. Several applications of machine learning techniques [198, 199] and neural networks [200, 201] to traditional quantum chemical problems show the great promise of this approach. A typical feature of data driven methods is its interpolative nature. Extrapola-

tions beyond the data set are difficult, and convergence beyond a certain accuracy can be slow if poor choices are made among the many representations, similarity and regressor options.

It has been suggested to combine efficient semi-empirical (SE) methods with ML approaches [202, 203], since the former contributes important chemical information "easy" to capture, while the latter may improve on the accuracy, thereby extending the limited flexibility of the SE methods due to their inherent approximations, such as minimal basis sets, integral approximations, or use of atomic charges in the Hamilton. One possibility is to augment SE methods with machine learning corrections in the so-called ΔML [202] method, where results are corrected based on a description of the entire molecule. Alternatively, parameters of an SE Hamiltonian matrix [203] can be trained. Both approaches lead to significant improvements in accuracy.

In this chapter, we combine the semi-empirical DFTB method with ML to improve the prediction of thermochemical data and molecular structures. In doing so, we tackle the problem of repulsive potential fitting and attempt to move forward the method as such. In contrast to other SE methods, the DFTB Hamilton matrix elements are computed in a two-center approximation and are not derived by fitting to experimental or computed data. However, the repulsive potential, which is bond-specific rather than atom or molecule-specific, is fitted to reproduce molecular energies and structures. The machine learning trend exploits ever larger sets of molecular data. So far the DFTB methodology did not benefit from this development, since parameterizations were created manually [173], although progress has been made on automatizing the process [19, 21]. Yet, since the number of free parameters is small, only limited and handpicked data can be included in the fit. ΔML fits corrections globally to reproduce molecular properties. In contrast, DFTB fits bond-specific properties, which requires a different approach for the inclusion of ML corrections.

Targeting bonds with ML has specific advantages: Because the set of possible bond topologies is much smaller than the set of possible molecular conformations, such an approach should have the advantage of lower training data requirements and better expected transferability. For example, the ΔML approach will fail for molecules larger than those included in the training set as it only interpolates between known molecules. A bond based repulsive potential approach, on the other hand, will work for molecules of any size as long as the constituent bonds are known. It has been shown that atom pairwise potentials can be used to predict atomization energies [198]. However, only equilibrium energies can be included since potential energy surfaces would require too much training data, and only a certain accuracy can be achieved. Both limitations can be lifted when combining ML with DFTB: Potential energy surfaces are naturally described by the DFTB repulsive potentials because the mathematical form of the repulsive potentials treats both, equilibrium and deformed molecular geometries, on equal footing. This also opens the path to train for transition state structures. Further, to improve accuracy, information beyond two-body interactions is required, which already is partly contained in the DFTB electronic energy.

In this chapter, we propose a generalization of the DFTB repulsive potentials, which depends on a quantitative notion of the bond topology, rather than on atom types. In the context of machine learning, it may also be understood as an attempt to exploit the hierarchical structure of molecules – built up of atoms, then bonds – in order to create a model that is able to make predictions also for molecules not well represented in the training set. The method is designed to require as little user input as possible. It is meant to scale to arbitrarily large training data sets, hence rendering the growing amount of available data useful for DFTB parameterization. The chapter is structured as follows: We first briefly recapitulate the repulsive potential concept and then introduce the generalized repulsive potentials, for which we provide a proof-of-principle implementation. Then we analyze its performance. Finally, we discuss some technical details necessary for practical implementation and draw conclusions.

6.2 DFTB Background

6.2.1 DFTB

This sections recalls the DFTB formalism very briefly to highlight the different nature of the electronic parameters and the repulsive potentials. The background chapter contains are more in-depth discussion (sec. 2.1.3). The DFTB methodology consists of a series of computational models, which are derived as an approximation to DFT. The total energy $E[\rho]$ is expanded at a reference electron density ρ_0, which is taken as the sum of contracted free atom densities. The expansion may be truncated at the first, second or third order and the corresponding models are known as DFTB1 [52], DFTB2 [53] and DFTB3 [54]. Introducing Kohn-Sham orbitals ϕ_i the energy functional expansion in the DFTB2 case reads:

$$E[\rho] \approx \sum_i f_i \langle \phi_i | -\frac{1}{2}\nabla^2 + \int d^3\mathbf{r}' \frac{\rho_0(\mathbf{r}')}{|\mathbf{r}-\mathbf{r}'|} + \frac{\delta E_{\text{xc}}[\rho_0]}{\delta\rho(\mathbf{r})} + V_{\text{ext}}(\mathbf{r}) | \phi_i \rangle$$
$$+ \frac{1}{2}\int d^3\mathbf{r} d^3\mathbf{r}' \left(\frac{1}{|\mathbf{r}-\mathbf{r}'|} + \frac{\delta^2 E_{\text{xc}}[\rho_0]}{\delta\rho(\mathbf{r})\delta\rho(\mathbf{r}')} \right) \delta\rho(\mathbf{r})\delta\rho(\mathbf{r}')$$
$$+ E_{\text{xc}}[\rho_0] + E_{\text{nuc-nuc}} - \frac{1}{2}\int d^3\mathbf{r} d^3\mathbf{r}' \frac{\rho_0(\mathbf{r})\rho_0(\mathbf{r}')}{|\mathbf{r}-\mathbf{r}'|} - \int d^3\mathbf{r} \frac{\delta E_{\text{xc}}[\rho_0]}{\delta\rho(\mathbf{r})}\rho_0(\mathbf{r}). \tag{6.1}$$

The f_i are orbital occupations, V_{ext} includes electron-nuclei and external field interaction, $E_{\text{nuc-nuc}}$ denotes the inter-nuclear interaction, and E_{xc} refers to the exchange-correlation functional, where DFTB employs the gradient-corrected PBE functional. The terms in the last line depend only on the reference density ρ_0 and the nuclear repulsions, which form the so-called repulsive potential V_{rep}. This is the focal point of our method and will be discussed in more

detail in the next section. The linear and second order terms in eq. 6.1 in the first and second line are further approximated and expressed as:

$$E_{\text{DFTB}}^{(1)} = \sum_{ij} \sum_{\mu\nu} c_{\mu i} c_{\nu j} H_{\mu\nu}^{(0)} \tag{6.2}$$

$$E_{\text{DFTB}}^{(2)} = \frac{1}{2} \sum_{A,B} \Delta q_A \Delta q_B \gamma_{AB}, \tag{6.3}$$

where the Δq_A are the differences between the Mulliken charges of atom A and the corresponding neutral atom, and the $c_{\mu i}$ are the expansion coefficients of the Kohn-Sham orbital $\phi_i = \sum c_{\mu i} \chi_\mu$ in the basis $\{\chi_i\}$ that consists of a minimal basis of Slater-type orbitals confined to the valence shell. The zeroth order Hamiltonian

$$H_{\mu\nu}^{(0)} = \langle \chi_\mu | -\frac{1}{2} \nabla^2 + \int d^3 \mathbf{r}' \frac{\rho_0(\mathbf{r}')}{|\mathbf{r} - \mathbf{r}'|} + \frac{\delta E_{\text{xc}}[\rho_0]}{\delta \rho(\mathbf{r})} + V_{\text{ext}}(\mathbf{r}) | \chi_\nu \rangle$$

is pre-calculated in a two-center approximation, where ρ_0 is the sum of atomic densities around the atoms on which the basis functions χ_μ and χ_ν are centered. At second order, the shape of the local density around atom A is assumed to be well described by a spherical function Φ_A, so that the Coulomb integrals $\gamma_{AB} = \int d^3 \mathbf{r} d^3 \mathbf{r}' \left(\frac{1}{|\mathbf{r}-\mathbf{r}'|} + \frac{\delta^2 E_{\text{xc}}[\rho_0]}{\delta(\mathbf{r})\delta\mathbf{r}'} \right) \Phi_A(\mathbf{r})\Phi_B(\mathbf{r}')$ can be evaluated analytically. In the DFTB3 model, resulting from a third order expansion, eq. 6.1 is augmented by an extra term as follows:

$$E_{\text{DFTB}}^{(3)} = \frac{1}{3} \sum_{AB} \Delta q_A^2 \Delta q_B \Gamma_{AB} \tag{6.4}$$

The off-diagonal terms Γ_{AB} are analytic representations of third order integrals and the diagonal terms can be calculated as atomic hardness derivatives.

Note that the first, second, and third order terms, which make up the set of electronic terms because they appear in the Hamiltonian, are calculated, not fitted to data. They are, therefore, rather rigorous, and we do not want to tamper with with them by adding any fitted, empirical ML correction to them.

6.2.2 Repulsive Potential

The last row of eq. 6.1 contains the core-core repulsion and those energy contributions that depend on the reference density ρ_0 only. They are grouped together into a single term called the repulsive potential V_{rep}, which is approximated as a sum of two-center repulsions,

$$V_{\text{rep}} = \frac{1}{2} \sum_{A,B} V_{AB}(|\mathbf{R}_A - \mathbf{R}_B|). \tag{6.5}$$

These two-body potentials are fitted to the difference of the total energy of a reference calculation and the DFTB electronic energy,

$$V_{\mathrm{rep}}(|\mathbf{R}_A - \mathbf{R}_B|) = E_{\mathrm{ref}}(|\mathbf{R}_A - \mathbf{R}_B|) - E_{\mathrm{DFTB}}(|\mathbf{R}_A - \mathbf{R}_B|),$$

with the energy contributions eqns. 6.2, 6.3 and 6.4,

$$E_{\mathrm{DFTB}} = \sum_i E_{\mathrm{DFTB}}^{(i)}.$$

The DFTB pairwise potentials V_{AB} depend only on the atom types of A and B, in contrast e.g. to force field models, where different bonding environments are encoded by different bonding parameters. Since the terms from eq. 6.1 grouped into the repulsive potential contribution depend on the reference density only, the adaption to different bonding situations is governed by the DFTB electronic energy contributions, in principle.

Atomization and reaction energies can form part of the reference energies, as well as forces, in particular at equilibrium structures [194]. In previous work, the repulsive potential contributions have been fitted to minimize the errors for atomization energies, geometries and vibrational frequencies for the G2/97 reference set.

However, since these terms are subjected to approximations as well, using a minimal basis set, applying a monopole approximation, neglecting three-center contributions, to name only the most prominent ones, the transferability is limited in practice. This shows up, e.g., in an optimization conflict for atomization energies and vibrational frequencies. To reach a reasonable accuracy for both properties, two distinct parameterizations had to be generated [194], which is due to the limited transferability of the parameters between different hybridization states, i.e. single, double and triple bonds. This is due to a number of reasons: (i) For good vibrational frequencies, the repulsive potentials need to have certain curvatures at the equilibrium distances, for atomization energies certain absolute values are needed, and these two conditions can not be fulfilled simultaneously when a certain accuracy is targeted. (ii) Further, a different degree of over-binding is found for single, double and triple bonds, leading to a relative shift of the potentials between the binding regimes, which is not possible to integrate into a single repulsive potential function. (iii) Finally, the repulsive potentials have to vanish before the second neighbour distances in order to avoid spurious long-range effects, which put additional restraints on the optimisation for the bonding properties.

Therefore, entangling theses different issues in a more adaptive repulsive energy scheme should lead to an overall improvement in accuracy.

6.3 Methodology

6.3.1 Generalized repulsive potentials

In the standard DFTB approach only one repulsive potential

$$V_{AB} = V_{t(A)t(B)},$$

is used to connect two atoms A and B of certain atom types, denoted by $t(A)$ and $t(B)$. In contrast, we now introduce a variable number of different potentials

$$V_{AB}(R) = V_{t(A)t(B)}(R) + \Delta V_{b(A,B)}(R), \tag{6.6}$$

called generalized repulsive potentials, which depend also on the bond type $b(A,B)$ to be defined. They are generated automatically and in a scalable way and augment the element pair repulsive potential $V_{t(A)t(B)}(R)$ from an existing DFTB parameterization. In this work, we use the repulsive parameters from 3OB [194, 204], while $\Delta V_{b(A,B)}(R)$ is a correction to this potential that can incorporate environment-specific information not grasped by the electronic parts of DFTB. By fitting corrections, rather than entirely new potentials, the existing potentials continue to serve as a fall-back for very unusual bonds, while for known bonds the correction term will improve the description. As $b(A,B)$ will denote bonds much more specific than the element pair $t(A)t(B)$, there is a chance to encounter bond topologies in applications for which no specific repulsive potential has been fitted yet. For example, it is possible to assign different repulsive potentials to different bond types (e.g. single, double, triple), but also distinguish various chemical environments. A carbon-carbon single bond may be subject to change when, e.g., neighboring electronegative atoms withdraw electrons, compared to the situation in pure hydrocarbons.

For the functional form of $\Delta V(R)$ we chose to use polynomials of degree k:

$$\Delta V_b(R) = \sum_{i=0}^{k} a_i^{(b)} R^i. \tag{6.7}$$

Other forms, such as splines, are possible as well, but at present we find simple polynomials to be sufficient. Note that if the forms of $V_{t(A)t(B)}$ and $\Delta V_{b(A,B)}$ agree, to linearly fit a correction potential ΔV_b is equivalent to fitting parameter corrections $\Delta a_i^{(b)}$. This holds for polynomials, splines, and other models linear in the parameters. Repulsive potentials should be short ranged and therefore tend to zero at large distances. To impose such asymptotic behavior, a cut-off R_c can be introduced at which $\Delta V_b(R)$ is smoothly set to zero. At present, we only run tests on geometries near equilibrium. Therefore, the asymptotic behavior is not relevant in this context.
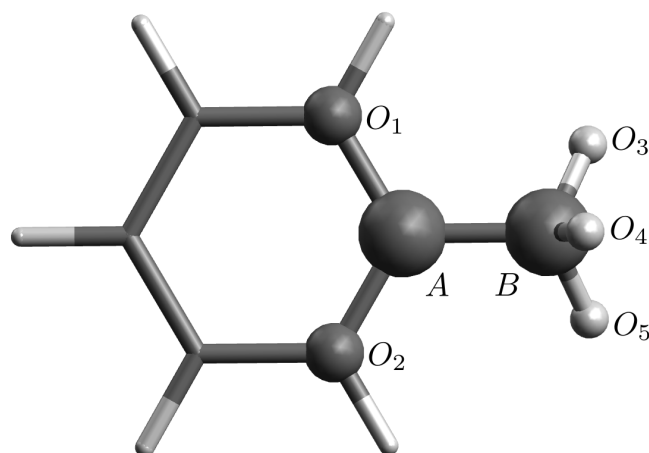
Figure 6.1: Example of a potential bond descriptor. The two large carbon atoms form the bond, all atoms displayed as balls are included in the descriptor. Atoms are labeled as they appear in the descriptor.

Eventually, the full generalized repulsive potential for a given molecular geometry reads

$$V_{\text{rep}} = \frac{1}{2} \sum_{AB} \left(V_{t(A)t(B)}(R_{AB}) + \Delta V_{b(A,B)}(R_{AB}) \right), \qquad (6.8)$$

$R_{AB} = |\mathbf{R}_A - \mathbf{R}_B|$ is the distance between atom A and B and $b(A,B)$ adds corrections for a set of bond types much larger than in traditional DFTB.

6.3.2 Bond descriptor

To determine $b(A,B)$, bond descriptors have to be introduced, which allow the recognition of certain bonds in molecular structures. This information is basically encoded in the geometrical arrangement of atoms in the immediate vicinity of the bond to be fitted. For instance, single and double bonded atoms will have a different number of nearest neighbor contacts, determining their hybridization state. The atom type of the neighbors can indicate certain properties of the local electronic structure (like local electron density). Lately, machine learning techniques for the prediction of molecular properties have become popular and accordingly much research on molecular descriptors has been undertaken, providing many options of varying sophistication, see e.g. Refs. 205, 206. Here, we started out with the rather simple Coulomb matrix descriptor [196], which turns out to work satisfactorily for the purpose of this work. The molecular geometry is represented by a matrix with diagonal terms identifying an atom type and off-diagonal terms are given by the nuclear Coulomb-repulsion of the respective atom pairs. The atoms are ordered unambiguously and the descriptor respects all the important symmetries like translational and rotational invariance of the molecule.

The bond descriptor requires two parameters and is defined as follows: Two atoms A and B are considered bonded for the purpose of the repulsive potentials, if their distance $R_{AB} = |\mathbf{R}_A - \mathbf{R}_B|$ is smaller than an element dependent cut-off $R_{AB} < R^c_{t(A)t(B)}$. A second parameter R^c_b defines a region within which all atoms O are included to specify the chemical environment of the bond between A and B (see Fig. 6.1). Specifically, an atom O is included in the descriptor if

$$\min_{C=A,B} |\mathbf{R}_O - \mathbf{R}_C| < R^c_b. \tag{6.9}$$

Then the bond-descriptor $b(A,B)$ is defined as

$$b(A,B) = \begin{pmatrix} \frac{1}{2}\eta Z_A^{2.4} & \frac{Z_A Z_B}{|\mathbf{R}_A - \mathbf{R}_B|} & \frac{Z_A Z_{O_1}}{|\mathbf{R}_A - \mathbf{R}_{O_1}|} & \cdots \\ \frac{Z_A Z_B}{|\mathbf{R}_A - \mathbf{R}_B|} & \frac{1}{2}\eta Z_B^{2.4} & \frac{Z_B Z_{O_1}}{|\mathbf{R}_B - \mathbf{R}_{O_1}|} & \cdots \\ \frac{Z_{O_1} Z_A}{|\mathbf{R}_{O_1} - \mathbf{R}_A|} & \frac{Z_{O_1} Z_B}{|\mathbf{R}_{O_1} - \mathbf{R}_B|} & \frac{1}{2} Z_{O_1}^{2.4} & \cdots \\ \vdots & \vdots & \vdots & \ddots \end{pmatrix}. \tag{6.10}$$

Attention has to be paid to the order of the atoms to make the descriptor unambiguous. The two atoms of the bond, A and B come first and their order is determined by their norm, that is

$$\left(\frac{1}{2}\eta Z_A^{2.4}\right)^2 + \sum_{C \neq A}\left(\frac{Z_A Z_C}{|\mathbf{R}_A - \mathbf{R}_C|}|\right)^2 \geq \left(\frac{1}{2}\eta Z_B^{2.4}\right)^2 + \sum_{C \neq B}\left(\frac{Z_B Z_C}{|\mathbf{R}_B - \mathbf{R}_C|}\right)^2,$$

where C runs over all atoms in the descriptor. Likewise, the other atoms $O_1, O_2, ...,$ following A, B are ordered by the norms of their rows.

$b(A,B)$ is equal to the Coulomb matrix of the bond environment, except for the special significance of the first two rows that always contain the information about the bonded atoms and the factor η that scales the diagonal entries for atoms A and B. η should be larger than one to give particular weight to the atom types of the bonded atoms and to ensure that bonds involving different elements are always further apart than bonds involving the same elements in the space of bonds spanned by the bond descriptors. There is no sensible dependence on the precise value of η.

Finally, we need to define a notion of distance between two bonds $b^{(1)}$ and $b^{(2)}$. We use the 2-norm

$$d(b^{(1)}, b^{(2)}) = \sqrt{\sum_{ij}\left(b_{ij}^{(1)} - b_{ij}^{(2)}\right)^2}, \tag{6.11}$$

where b_{ij} are the entries of the descriptor matrix. The 2-norm provides the practical advantage that certain libraries can be used directly in the implementation of the method, which do not support the 1-norm that is often used for estimating similarity of structures when using the

Coulomb matrix [196]. However, there is no significant difference between the two choices for our application. All Coulomb matrices need to have the same dimension, and for chemical environments characterized by a smaller number of participating atom the matrix is filled with zeros. The zeros may be thought of as atoms infinitely removed from the bond.

The parameter R_b^c critically affects the specificity of the bond descriptor. If it is smaller than the shortest typical bond length, only the two bonded atoms will be included, and nothing is gained over the existing DFTB repulsive potentials since no information about the environment enters the description. Using values larger than typical bond lengths, the nearest neighbors of the bonding atoms will be included, the minimal representation of the chemical environment, which already leads to very good results. Further increasing the parameter, non-local information can be included as well. Hence, the method can take in ever more information as the amount of training data grows, what is a desired feature of the approach. This can be expanded up to the limit where the entire molecule forms the descriptor and one has a molecule specific fit. Such descriptors are used e.g. in the Δ machine-learning approach [202], i.e. molecule-specific parameters are determined which are used for an interpolation to molecules not present in the training set.

6.3.3 Bond clustering

The next step is the automatic identification, i.e. the clustering, of relevant bond-types from a large training set of molecular structures, based on the descriptor. Every cluster, or bond type, will define one generalized repulsive potential. In each of the molecular structures bonds and their respective environments are identified according to the two cut-off criteria, and the Coulomb-matrices are then set up. Similar bonds yield very similar descriptors, although they are not exactly identical due to slightly varying interatomic distances. Hence, bonds form clusters of a finite, but narrow width in the high dimensional feature space spanned by the bond descriptors, where different clusters correspond to different bond types. The dimension of the feature space is determined by the size of the largest Coulomb matrix and depends on the value of R_b^c. When R_b^c is such that nearest neighbours are included in the descriptor, the dimension is bounded from above by about $8^2 = 64$ because there are 8 atoms in the descriptor of a C-C single bond, and it is not chemically feasible to gather many more atoms in such a small volume. Identifying bond types then becomes a clustering problem. Such a problem is commonplace in unsupervised machine learning [207], and many methods have been proposed for its solution. The choice of an appropriate algorithm, however, turned out to be not completely straight forward. In particular, the highly unbalanced number of data points in different clusters was problematic. Since some bond types are far more abundant than others, the clustering algorithm has to be insensitive to the number of cluster members. For example, the popular k-means [208, 209] algorithm turned out to be unsuitable for this reason, as our training set contained,

among others, far more, C-H than C-F bonds and k-means would only produce a large amount of C-H, but no C-F cluster.

The mean-shift algorithm [210, 211] that was originally developed for image processing applications, in contrast, turned out to work well. Here, we give only brief description of the algorithm; more detail can be found in original literature [210, 211]. Let

$$m(b) = \frac{\sum_i b_i K\left(\frac{d(b,b_i)}{h}\right)}{\sum_i K\left(\frac{d(b,b_i)}{h}\right)} \tag{6.12}$$

be the mean-shift vector at position b. b is a general bond descriptor, the b_i are the bond descriptors in the set to be clustered, the real number $h > 0$ is the kernel width, and the function K is the kernel function. K can be any positive function integrating to one, but for the purpose of this work we adopt a flat kernel:

$$K(x) = \begin{cases} 1 \text{ for } 0 \le x \le 1 \\ 0 \text{ otherwise} \end{cases} \tag{6.13}$$

The flat kernel is a simple choice and performs well for our application. With the mean-shift vector clusters are now identified through the iteration

$$b^{(t+1)} = m(b^{(t)}), t = 0, 1, ... \tag{6.14}$$

that will converge to a value b^*, the centroid of a cluster. One scans sufficiently many initial values $b^{(0)}$ to find all centroids and thus all clusters.

The algorithm in this form appears rather abstract, but it has an intuitive interpretation. If we assume the data points b_i to be samples from a continuous density $\rho(b)$, then with the smoothing kernel function K the smooth density can be approximated as $\rho(b) \approx \frac{1}{Nh^d} \sum_i K\left(\frac{d(b,b_i)}{h}\right)$, where N is the number of samples and exponent d is the dimension. It can be shown that $\nabla\rho(b) \propto m(b)$. Consequently, the mean-shift algorithm can be thought of as steepest-descent to find the local maxima of ρ, and clusters can be identified with blobs in the density. Although the flat kernel is not a smooth one, it can be approximated arbitrarily well by a smooth kernel and, therefore, the argument still holds.

The mean-shift algorithm is available as part of the scikit-learn Python module [212], which we use in our implementation of the method.

The kernel width parameter h is of crucial importance, since it sets the minimal distance of two points to be still regarded as members of the same cluster. Therefore, it also determines the number of different bond types to be identified. Because the number of clusters M is the more tangible quantity, we will classify the resulting repulsive potentials by M, rather than h. Yet,

even when we refer to *M* for clarity, *h* remains the fundamental variable.

The number of clusters *M* can be increased as the amount of training data grows. Hence, the method can scale to large training sets by fitting many different potentials. In the limit of very large sets, every individual bond could be represented by its own fitted potential.

At last, with bond types defined through clustering, any new bond *b* not in the training set must be assigned the cluster or bond type it belongs to. Alternatively, it may also happen that no existing bond type describes *b* well. This case must be recognized, too. A mean field iteration started from *b* will converge to the centroid b^* of the cluster best describing *b*, thus identifying the bond type. For simplicity's sake, we assume $b*$ to be the centroid closest to *b* according to the metric $d(b, b^*)$, an assumption we found well justified. Then, b^* can be identified as

$$b^* = \argmin_{\tilde{b} \in \text{centroids}} d(b, \tilde{b}).$$

To rule out the cases where b^* does not describe *b* well, we demand that the centroid and bond are closer to each other than a certain tolerance distance w^*:

$$d(b, b^*) < w^*.$$

A well chosen value of w^* depends on whether the cluster of b^* is narrow or wide. Therefore, we calculate the cluster width σ^* from the training data:

$$\sigma^* = \sqrt{\sum_{\tilde{b} \text{ belongs to } b^*} d(\tilde{b}, b^*)^2}.$$

The sum runs over all bond descriptors in the training set belonging to centroid b^*. Hence, we set

$$w^* = \tau \cdot \sigma^*,$$

with a tolerance factor τ to be set manually.

6.3.4 Potential fit

In the next step, the repulsive potentials $\Delta V_b(R)$ for all new bond types *b* are fitted in the same way as the standard DFTB repulsive parameters. The $a_i^{(b)}$ in eq. 6.7 are determined in order to minimize a fitness function $f(a_0^{(1)}, a_1^{(1)}, ..., a_0^{(2)}, ...)$, which as target properties contains molec-

ular atomization energies E_{at} and forces $\mathbf{F}$ for a set of equilibrium and perturbed molecular geometries:[1]

$$
\begin{aligned}
f(a_0^{(1)}, a_1^{(1)}, ..., a_0^{(2)}, ...) = &\sum_{m \in \text{equi}} \left(E_{\text{at},m}^{\text{ref}} - E_{\text{at},m}^{\text{DFTB}} - \sum_{b \in m} \Delta V_b(R_b) \right)^2 \\
&+ f_{\text{opt}} \sum_{m \in equi} \frac{1}{3N_{\text{at,m}}} \left(\mathbf{F}_{\text{at},m}^{\text{ref}} - \mathbf{F}_{\text{at},m}^{\text{DFTB}} + \sum_{b \in m} \frac{\mathbf{R}_b}{R_b} \frac{\partial}{\partial R} \Delta V_b(R_b) \right)^2 \\
&+ e_{\text{pert}} \sum_{m \in \text{pert}} \left(E_{\text{at},m}^{\text{ref}} - E_{\text{at},m}^{\text{DFTB}} - \sum_{b \in m} \Delta V_b(R_b) \right)^2 \\
&+ f_{\text{pert}} \sum_{m \in \text{opt}} \frac{1}{3N_{\text{at,m}}} \left(\mathbf{F}_{\text{at},m}^{\text{ref}} - \mathbf{F}_{\text{at},m}^{\text{DFTB}} + \sum_{b \in m} \frac{\mathbf{R}_b}{R_b} \frac{\partial}{\partial R} \Delta V_b(R_b) \right)^2.
\end{aligned}
\tag{6.15}
$$

Perturbed geometries are created from equilibrium geometries through displacement along normal mode coordinates. The fitness function is generated by summing of all equilibrium and perturbed molecular geometries, and by computing the energy and force contributions resulting from the repulsive potentials, which sum over all bond types b. The potentials can be written as

$$
\Delta V_b(R_b) = \left(1\, R_b\, R_b^2 \, ... \right) \cdot \left(a_0^{(b)}\, a_1^{(b)} \, ... \right)^T,
$$

and therefore the optimization procedure is a least squares problem of the form $\min_{\mathbf{x}} |\mathbf{y} - A\mathbf{x}|^2$, with given vector $\mathbf{y}$ and matrix A, where the parameter vector $\mathbf{x}$ has to be determined. Many tools exist to solve this problem. We use the Numpy [213] least-squares function that utilizes a singular value decomposition.

The weight factor $\frac{1}{3N_{\text{at,m}}}$ is added since for each geometry only one energy but $3N_{\text{at},m}$ force conditions have to be fulfilled. In that way energies and forces are given the same initial weight. The additional weight factors $f_{\text{opt}}, e_{\text{pert}}$, and f_{pert} control the relative weights of energies and forces for equilibrium and perturbed geometries, respectively. They must be set manually.

6.4 Application

The approach is applied to a large molecule set, which features structures and energies computed at the B3LYP/6-31G(2df,p) level of theory. For a final reparameterization a higher level of theory is desirable. Therefore, we use these data for a proof-of-concept approach in order to evaluate the procedure suggested in this work.

---

[1]The atomization energy is the difference between the molecular energy and the sum of free atom energies of the atoms constituting the molecule. To the DFTB free atom energies spin polarization terms are added to account for the lack of direct spin polarization [194].

6.4.1 Data set

To test the approach we use a molecular data set created by Ramakrisgnan et al. [214], which provides optimized structures and properties for small organic molecules from the GDB-17 [215] set, containing the elements C, H, O, N, and F with up to nine non-hydrogen atoms. The set contains 133,885 molecules, geometry optimized at the B3LYP/6-31G(2df,p) level of theory [38–40].

The molecule set is separated into a training set of the first 2100 molecules and a test set containing the rest. The training set is supplemented with non-equilibrium geometries generated as follows: Starting from relaxed geometries, all coordinates are displaced in both directions of all those normal modes which change bond lengths. The amount of displacement if chosen such that the energies vary only on the order of $1 \frac{\text{kcal}}{\text{mol}}$ with respect to the equilibrium energy. For the distorted structures, energies and forces are computed using B3LYP/6-31G(2df,p), to be consistent with the other reference data. Eventually the training set contains about 150000 relaxed and unrelaxed structures in total. For every molecule in the test set we run DFTB calculations with 3OB parameters and the full third order formalism [54, 194] that yields the DFTB base-line of electronic and repulsive potential contributions.

6.4.2 Clustering and fit

The cut-off parameters $R^c_{t(A)t(B)}$, that determine atom pairs connected by generalized repulsive potentials are chosen as the cut-off parameters of the 3OB repulsive potentials [194]. The cut-off parameter R^c_b that determines which atoms enter into the Coulomb-matrix descriptor is set to $R^c_b = 1.8\,\text{Å}$. For the molecular structures considered here, this includes nearest neighbors of the bonded atoms. The parameter η, which gives special weight to the bonded atoms, is chosen as $\eta = 5$ and selective tests show that the results are not very sensitive to the precise value of η once $\eta > 2$. Lastly, the tolerance factor τ is put to $\tau = 3$, and again results are not very sensitive to the precise value of the parameter within reasonable bounds. Mean-shift clustering is performed on the set of all the bonds found in the equilibrium geometries of the training set molecules for these parameter values. As a precaution, to prevent over-fitting, we drop bond types that are not present in at least three different molecules. Especially when two bonds occur only once and in the same molecule, their potentials can cancel each other and therefore assume arbitrary values. To solve this problem, one can simply generate more data from geometry perturbations for bonds that do not occur often enough, but we refrained from doing so at the present exploratory stage.

Hence, sets with $M = 10, 25, 42, 84, 111, 200$, and 259 different bond types are created. Tab. 6.1 gives values of h for each M for reproducibility. M does not vary continuously with h, but tends to jump, so there is no exact one-to-one correspondence.

M	10	25	42	84	111	200	259
h	93.26	75.525	58.627	43.402	36.089	27.130	23.4
q	15%	9%	5%	3%	2%	1.3%	-

Table 6.1: Values for the Kernel width h resulting in certain numbers of potentials M. Most widths h were in terms calculated as the qth percentile of pairwise distances of data points, explaining their odd values. The percentiles q are then also given.

Varying numbers of generalized repulsive potentials allow us to investigate whether the performance of the method indeed improves with growing numbers, and at what point performance saturates.

For each set of bond types, we fit generalized repulsive potentials $\Delta V_b(R)$ as polynomials of degree $k = 6$, that is with 7 free parameters. The weight of equilibrium forces f_{opt} is set to $f_{opt} = 100$, non-equilibrium force weight is put to $f_{pert} = 1$, and non-equilibrium atomization energies carry weight $e_{pert} = 1$. We found those values by trial and error. They have not been properly optimized, yet.

6.4.3 Results

First, we investigate the clustering step that is pivotal for the method, which stands and falls with the meaningful identification of bond types for the generalized repulsive potentials. Fig. 6.2 shows two dimensional projections of all the bond descriptors in the training set, generated by a principle component analysis [216, 217] (PCA). PCA identifies the two dimensional subspace in which the variance of the data is maximal. Various clusters of different sizes appear already in two dimensions that in higher dimensions in terms decompose into more, smaller clusters. Clusters correspond to different kinds of bonds, many of which are indicated in the figure. Also displayed in Fig. 6.2 are the centroids of the clustering with $M = 200$ clusters. For every centroid there is one generalized repulsive potential. All clusters are covered with centroids, and the large clusters carry many centroids because of the many smaller clusters they contain, but small, isolated clusters are covered too. This is important, and, for example, k-means failed to achieve this. Altogether, Fig. 6.2 shows a reasonable clustering according to bond topology and supports that the Coulomb matrix based bond descriptor, together with mean-shift clustering, can indeed identify meaningful bond types.

Next, we examine the fitted potentials ΔV. Higher order polynomials can oscillate significantly in the case of over-fitting. By visual inspection the potentials are confirmed to be well behaved. Fig. 6.3 shows two representative sample potentials for a single and double C-C bond. Position, slope and curvature of the repulsive potentials are altered, but the functions remain monotonously decaying without spurious behavior. Of course, because no boundary conditions were applied, this is only true for distances sufficiently close to the respective bond lengths,
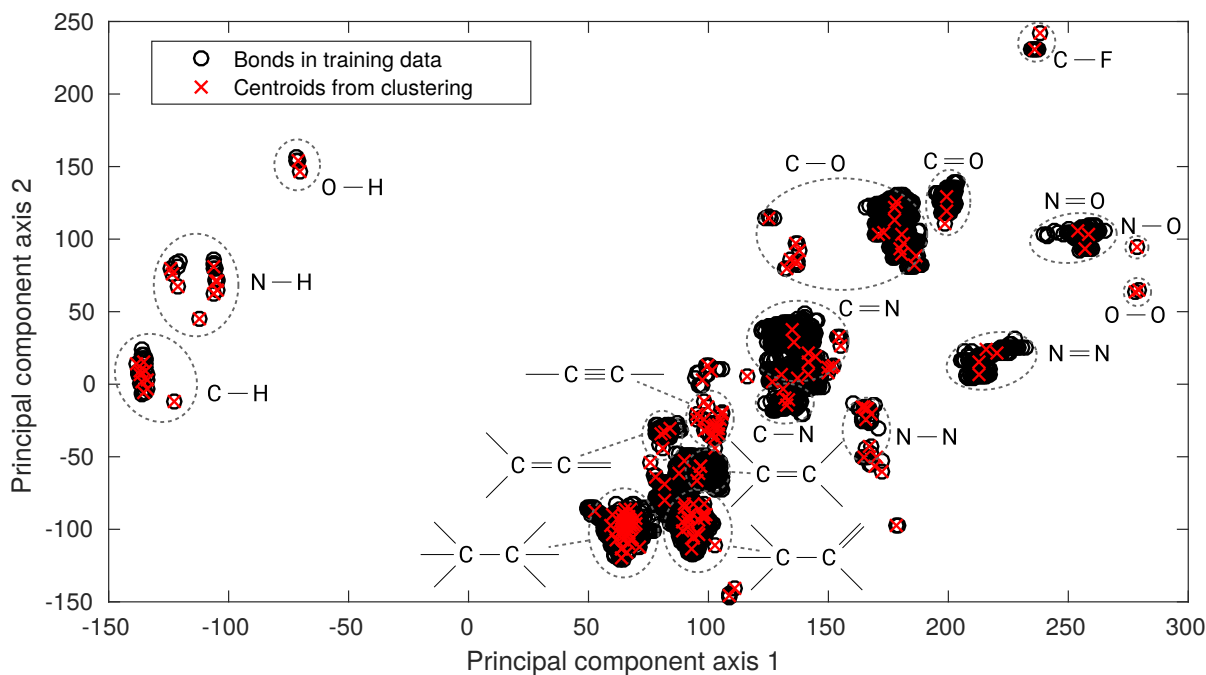
Figure 6.2: Visualization of the bond descriptors from the training set and $M = 200$ centroids from mean-shift clustering in two dimensions. The high dimensional descriptor space has been projected to two dimensions by a principle component analysis [216, 217]. Note that the large clusters decompose into many smaller clusters corresponding to different chemical environments. The mean-shift algorithm covers all clusters well regardless of the number of data points in them.
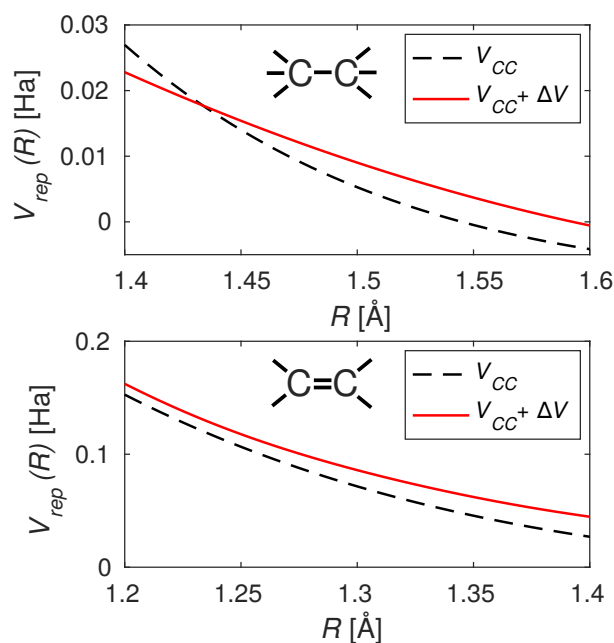
Figure 6.3: Sample repulsive potentials for a C-C single and double bond with $M = 111$ generalized repulsive potentials. Magnitude, slope and curvature are altered by the potential corrections.
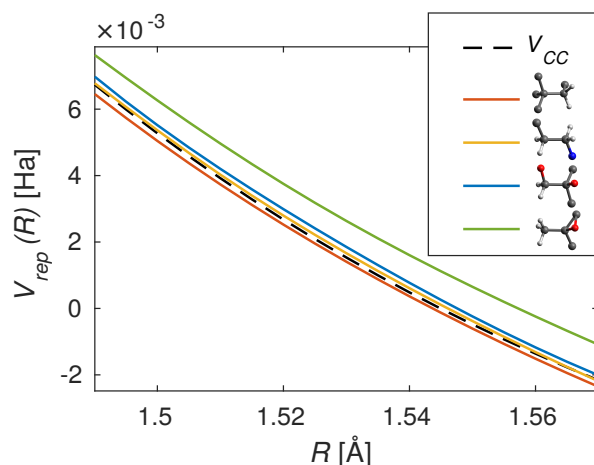
Figure 6.4: Generalized repulsive potentials for different types of C-C single bonds. The atoms that make up the descriptor are displayed in the legend. Potentials differ, particularly by a vertical displacement, with slopes more similar.
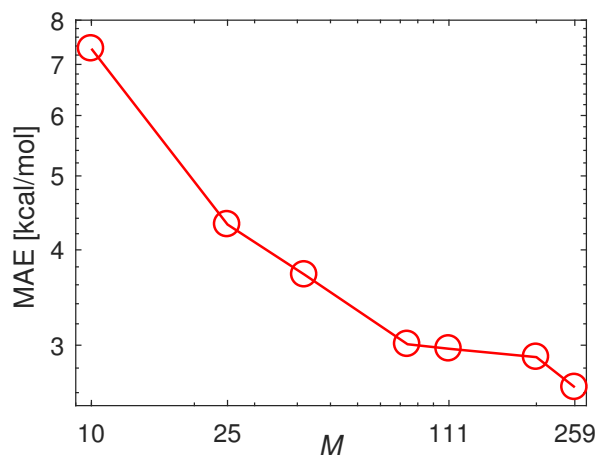
Figure 6.5: Mean absolute error in atomization energy for the molecules in the test set for a growing number M of generalized repulsive potentials. As the number of potentials grows, the error decreases quickly and significantly, demonstrating that increasing the number of repulsive potentials indeed improves the method.

but in the present study we only work with such geometries. It is also interesting to see how different potentials for the same bond topology, like e.g. C-C single bonds, can occur. Fig. 6.4 shows various potentials for C-C single bonds. While most of them remain close to the uncorrected potential V_{CC}, there is a considerable variation for some of them. They appear to be up- and down-shifted, slopes remain similar. For chemical environments with more electronegative substituents on the bonded atoms, the potentials are shifted up.

Ultimately, the method's usefulness is determined by its quantitative performance. For a benchmark, we applied it to all of the $\sim 130,000$ molecules in the test set. Fig. 6.5 shows the mean absolute errors (MAEs) in atomization energy with varying numbers of generalized repulsive potentials; Tab. 6.2 displays MAEs and root mean squared errors (RMSE). The MAEs

M	0	10	25	42	84	111	200	259
MAE [kcal/mol]	7.38	7.34	4.32	3.71	3.01	2.97	2.89	2.64
RMSE [kcal/mol]	9.31	9.74	5.65	5.46	3.94	3.95	4.00	3.82

Table 6.2: Mean absolute (MAE) and root mean squared (RMSE) error in atomization energy taken over all test set molecules.
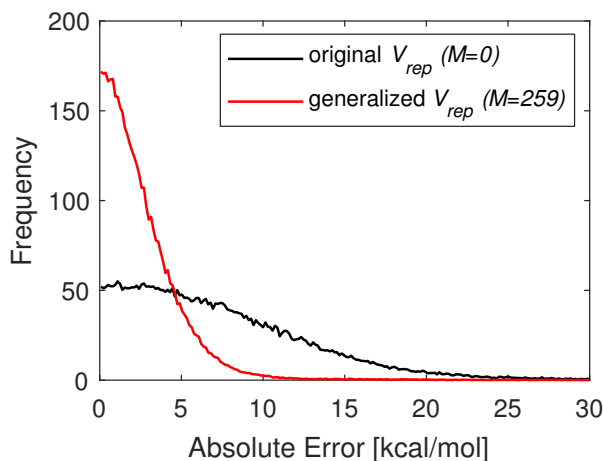
Figure 6.6: Normalized histogram of absolute errors in atomization energy for the ~ 130000 molecules in the test set with $M = 259$ generalized repulsive potentials.

monotonously decay with a growing number of potentials. The first step is very small, then the error decreases rapidly. The improvement brought about by the addition of generalized potentials is clear. With $M = 259$ generalized repulsive potentials the remaining error is $\Delta E_{259} = 2.64 \frac{\text{kcal}}{\text{mol}}$, down from $\Delta E_0 = 7.34 \frac{\text{kcal}}{\text{mol}}$ with the original 3OB repulsive potentials. Therefore, the error is significantly reduced to about a third of the original error. Figs. 6.6 and 6.7 show
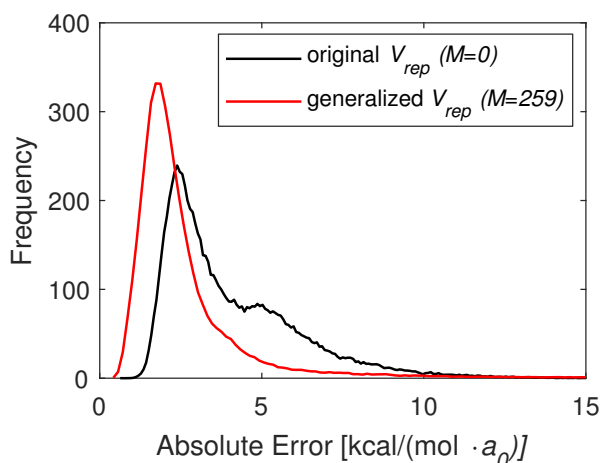
Figure 6.7: Normalized histogram of the magnitudes of errors in force per atom for the molecules in the test set with $M = 259$ generalized repulsive potentials.
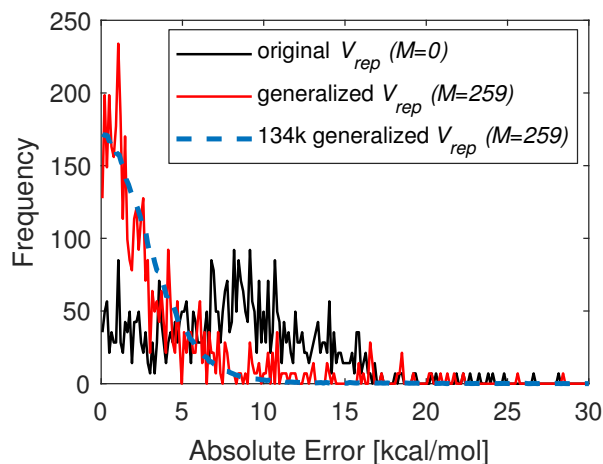
Figure 6.8: Normalized histogram of absolute errors in atomization energy for the 622 molecules in the Jorgsen test set with $M = 259$ generalized repulsive potentials. The histogram for the large test set is also shown for comparison.

histograms of absolute errors in atomization energies and force per atom, respectively. The distribution of errors in the atomization energy becomes significantly more narrow, demonstrating a systematic improvement, already reflected in the lower MAEs. Forces improve too. Initially the histogram shows two peaks, a large and a much smaller one at a higher error. The second peak indicates a small, systematic error in the predicted geometries, and this is removed after the addition of generalized repulsive potentials. However, the large peak is hardly moved. DFTB already predicts geometries well, and most of the error is in the bond angles, not lengths. Because repulsive potentials only yield forces along bond axes, the generalized potentials cannot reduce those errors.

Overall, a clear improvement of the performance of the method by the addition of generalized repulsive potentials is apparent.

We have also analyzed MAEs for molecules from a smaller test set introduced by Jorgsen et al. [218] that has been previously used to benchmark DFTB [194]. The set contains 622 molecules containing C, H, N, and O. Most molecules of the Jorgsen set are contained in the large test set, but the smaller set has been used often for quantum chemistry benchmarks, and therefore it is illustrative to compare performance on the well known subset with the whole. For a fair assessment we did not use results reported in the literature, but rather created data at our own reference level of theory, B3LYP/6-31G(2df,p). Fig. 6.8 shows error histograms with and without generalized repulsive potentials. A clear improvement is visible. Results look very similar to the large test set results, albeit more oscillatory due to sparcity of data. The MAEs of $\Delta E_0 = 8.26 \frac{\text{kcal}}{\text{mol}}$ with the original DFTB and $\Delta E_{259} = 3.64 \frac{\text{kcal}}{\text{mol}}$ are somewhat larger because of a few outliers, which are less frequent in the large set. That may be regarded as an example that good performance on average not necessarily implies good performance for every problem.

Finally, in Tab. 6.3 we investigate the effects of training set size. A clustering and fit was

training set size	M	h	MAE [$\frac{\text{kcal}}{\text{mol}}$]	RMSE [$\frac{\text{kcal}}{\text{mol}}$]
2100	200	27.13	2.89	4.0
2100	111	36.09	2.97	3.95
1000	156	24.71	3.52	5.52

Table 6.3: Comparison of errors in atomization energies for ~ 130k molecules with results obtained from smaller training sets.

performed with only 1000, rather than 2100, molecules in the training set. MAEs of atomization energies are about $1/2 \frac{\text{kcal}}{\text{mol}}$ larger than for comparable parameterizations with the larger training set. A training set of 1000 molecules is already large enough to be useful, but there is still clear improvement with training set size.

6.5 Conclusion

We have introduced generalized repulsive potentials for the DFTB method, where the traditional atom-type potentials are substituted by bond-type potentials. Bond types are determined by automatic clustering, leading to a description which reflects the chemical environment. Due to the automatic bond identification, repulsive potentials can be parametrized to fit large data sets and are not limited by the number of parameters, which can be scaled up as required. This brings DFTB into the age of data driven approaches. We presented a preliminary implementation of the method that clearly demonstrates its potential, offering significantly improved quantitative performance.

Since the present work only reports a proof of concept, further developments are required before routine application to quantum chemical problems:

(i) The reference data should be computed using a higher level method than used here. Now that the principle functionality of the method has been established, a smaller test set for verification can be applied, which allows to compute using higher level approaches.

(ii) Using better reference data, a test of different descriptors should be performed in order to evaluate whether the final performance can be improved. The literature offers a rich choice of options, and in future work we will try to identify the best solution.

(iii) Finally, a smooth switching between different bond-potentials is required, in particular when this scheme is to be applied for molecular dynamics simulations. Up to now, hard cut-offs

are assigned, which have to be substituted by switching functions f. The generalized repulsive potential becomes

$$\Delta V_{AB}(R_{AB}) = \sum_{\tilde{b}} f(d(b(A,B),\tilde{b}))\Delta V_{\tilde{b}}(R_{AB}),$$

where $\tilde{b}$ runs over all bond types and f interpolates smoothly between $f(0) = 1$ and $f(\infty) = 0$. One possibility would be the use of an error-function, which is often used in such contexts.

(iv) Further, the description of chemical reactions can be improved by adding transition state geometries to the training set.

7 Outlook

Throughout this work several new methodologies have been introduced that open paths for future research and development.

In chapters 3 and 4 mixed quantum-classical, nonadiabatic dynamics of charge and energy carriers in bulk materials were simulated. The use of nonadiabatic dynamics based methods for the study of transport phenomena is becoming more popular, with other groups going in the same direction [87, 219, 220]. We have already seen in chapter 4 that the choice of quantum-classical coupling – mean-field Ehrenfest, a surface-hopping method, or something different – affects the prediction and can even have a qualitative effect. Since, despite many attempts, hitherto quantum-classical dynamics methods can usually not be derived rigorously, but are proposed on heuristic arguments, the choice of the correct algorithm is very non-trivial. And as one of the primary incentives to use such methods over less costly and often simpler approaches, such as transition rate based methods, is that in principle they allow precise quantitative predictions in cases where it can be shown that other methods will not be exact, uncertainty over the choice of algorithm seems hardly acceptable. So far, systematic benchmarks of different quantum-classical dynamics schemes for spatial transport applications are still missing and appear a logical next step. This would shed more light on what effects are important and how to best incorporate them, removing some uncertainty over the choice of algorithm.

Another problematic aspect mentioned in chapter 4 is the presence of high frequency molecular vibrations coupling to excitons and charges. Such vibrational modes are quintessentially quantum mechanical in nature, but so far treated classically. We have already experimented with path-integral based methods along the lines of Ref. [221], but lacking rigorous foundations, have not yet reached any conclusions. Future research in this direction might lead to a solid way to deal with quantum modes. Certainly, it is worthwhile to investigate their role in more detail.

While the method for charge transport simulations in chapter 3 was originally developed for application to biomolecules in solutions, the newly presented method for exciton dynamics has so far not been applied in other contexts. In the light of the complex movement of molecules in solution and the large interest in exciton dynamics in such systems [222, 223], it seems promis-

ing to apply the method to those problems, too. Up to now, Förster rate based models still feature most prominently, even though it is known that, for example, solvent fluctuation can be very important [224], just as in charge transfer.

We constructed the LC-TD-DFTB method because GGA functionals perform poorly for extended π-electron systems, ubiquitously occurring in organic semiconductors. Of course, the next step is to replace TD-DFTB by LC-TD-DFTB within the exciton transport method. Charge transport may also profit when LC-DFTB is used for ground state calculations. Moreover, with underlying long-range corrected functionals we can try to calculate excitonic couplings from dimer calculations and diabatization, rather than as mere Coulomb couplings. Without long-range correction this is not possible because along molecular dynamics trajectories the involved molecules are not equivalent, and then local functionals admix spurious charge transfer states. The LC-TD-DFTB method is also likely to be useful for many other applications. For instance, DFTB is often used for QM/MM molecular dynamics simulations of biomolecules in solution. Because of the polar environment, charge transfer excitations are very common in this setting and cause problems for DFTB. LC-DFTB should perform much better in such situations.

Finally, we have already pointed out in chapter 6 that the generalized repulsive potential method is still in a development stage. The first results, however, demonstrate that data driven methods work successfully with DFTB, and this may be a path for DFTB to take. To make the method more practical, the potentials need to be next extended to full potential energy surfaces, as explained in the respective chapter. Machine learning and data science in molecular modeling is growing fast, and the pace of evolution is still high. Likewise, the amount of data is ever increasing. For example, Ref. [225] uses training data very similar to ours, but with much more complete potential energy surface scans. If such data was publicly available, and in the future it likely will be, there would be much room for improvement. It is well conceivable that the final model for a data derived DFTB framework will follow the general development and look different from what it looks like right now.

In conclusion, in this thesis we have introduced three new methods, and tested one, that will hopefully be useful in the future, either for direct application to intriguing problems or as a foundation for further development. Charge and energy transport are often intriguing phenomena, whose full understanding requires clever ideas and therefore will continue to inspire methodological development with reach far beyond.

A Extensive LC-TD-DFTB benchmark data

Table A1: Excitation energies for a set of small organic molecules as proposed by Thiel et al.[174].

Molecule	Symmetry	LC-ωPBE	best est.[174]	CC3[174]	DFTB	LC-DFTB
Ethen	B_{1u}	8.2536	7.8	8.37	6.884	7.424
	B_{1g}	8.5419			7.666	8.358
	B_{2G}	9.746			8.389	9.045
	B_{3u}	10.186			9.169	10.067
	B_{1g}	10.335			11.935	12.467
Butadien	B_u	6.3199	6.18	6.58	5.498	6.167
	A_u	7.685			5.543	6.091
	A_g	8.526	6.55	6.77	6.389	7.211
	A_u	8.603			6.403	7.503
	A_g	8.808			6.691	7.801
Hexatriene	B_u	5.26	5.1	5.58	4.429	5.06
	A_g	7.4	5.09	5.72	5.391	6.22
	B_g	7.424			5.053	5.569
	A_g	7.662				

Molecule	Symmetry	LC-PBE	best est.	CC3	DFTB	LC-DFTB
	A_u	7.99			5	6.627
Octatetraen	B_u	4.596	4.66	4.94	3.756	4.372
	A_g	6.548	4.47	4.97	4.14	5.805
	A_g	6.807				
	A_u	7.304			4.706	5.34
	B_g	7.638			4.91	5.746
Cyclopropene	B_1	6.861	6.76	6.9	6.442	7.244
	B_2	6.954	7.06	7.1	6.399	7.079
	A_2	7.735			7.652	8.543
	A_2	9.436			9.629	10.438
	B_1	10.034				
Cyclopentadiene	B_2	5.467	5.55	5.73	4.781	5.363
	A_1	7.582	6.61	6.31	6.025	7.023
	A_2	8.145			6.5	7.294
	B_1	8.329			6.204	6.876
	B_1	8.549				
Norbornadiene	A_2	5.645	5.34	5.64	5.215	6.335
	B_2	6.616	6.11	6.49	5.328	6.422
	A_2	7.864		7.71	6.369	7.196
	B_2	7.918		7.64	6.718	7.707
	B_1	7.992			6.545	7.485

Molecule	Symmetry	LC-PBE	best est.	CC3	DFTB	LC-DFTB
Benzene	B_{2u}	5.66	5.08	5.07	5.297	6.074
	B_{1u}	6.51	6.54	6.68	5.673	6.376
	E_{1u}	7.54	7.13	7.45	6.79	7.571
		7.54	7.13	7.13	6.79	7.571
	E_{2g}	8.227				
Naphtalene	B_{2u}	4.747	4.77	5.03	4.011	4.789
	B_{1u}	4.986			4.228	4.98
	B_{2u}	6.419	6.33	6.57	5.0108	5.899
	B_{1u}	6.736			5.308	6.352
	B_{3g}	6.875			5.625	6.387
Furan	B_2	6.602			6.058	6.614
	A_1	7.489	6.57	6.62	6.494	7.433
	A_1	8.829	8.13	8.53		
	A_2	9.049			8.006	8.823
	B_1	9.078			7.755	8.47
Pyrrolle	B_2	6.8587	6.57	6.71	6.386	6.877
	A_1	7.23	6.37	6.4	6.438	7.246
	A_2	7.94				
	A_1	8.595	7.91	8.17	7.884	8.594
	B_1	8.768				
Imidazole	A'	6.968	6.93	7.1	6.357	6.875

Molecule	Symmetry	LC-PBE	best est.	CC3	DFTB	LC-DFTB
	A''	7.001	6.81	6.82	6.211	6.914
	A'	7.607			6.863	7.478
	A''	8.118		7.93	7.207	7.879
	A''	8.434				
Pyridine	B_1	5.265			4.518	5.146
	A_2	5.687	5.11	5.5	4.808	5.604
	B_2	5.707	4.85	5.15	5.366	6.041
	A_1	6.71	6.26	6.85	5.818	6.482
	B_2	7.74	7.27			
Pyrazine	B_{2u}	4.3353	3.95	4.24	3.721	4.249
	A_u	5.21	4.81	5.05	4.343	5.165
	B_{2u}	5.501	4.64	5.02	5.24	5.76
	B_{2g}	6.018	5.56	5.74	5.529	6.095
	B_{1u}	6.848	6.58	7.07	5.908	6.517
Pyrimidine	B_1	4.717	4.55	4.5	4.23	4.842
	A_2	5.077	4.93	4.91	4.528	5.255
	B_2	5.922	5.44	5.36	5.259	5.886
	A_2	6.227			5.578	6.201
	B_1	6.505				6.674
Pyridazine	B_1	3.977	3.78	3.92	3.502	3.996
	A_2	4.757	4.31	4.49	4.141	4.858

Molecule	Symmetry	LC-PBE	best est.	CC3	DFTB	LC-DFTB
	A_1	5.93	5.18	5.22	5.259	5.95
	A_2	5.978	5.77	5.74	4.924	5.434
	B_1	6.678	6.41		5.564	6.254
Triazine		4.864	4.6	4.78	4.585	5.209
		4.9826			4.585	5.209
		4.9826			4.585	5.209
		5.037	4.7	4.81	4.585	5.209
		6.304	5.79	5.71	5.961	6.534
Tetrazine	B_{3u}	2.531	2.29		2.367	2.758
	A_u	4.016	3.51		3.677	4.379
	B_{1g}	5.157	4.73		4.626	4.732
	A_u	5.534	5.5		4.407	5.073
	B_{2u}	5.65	4.93		5.238	5.614
Formaldehyde	A_2	3.888	3.88	3.95	4.251	4.54
	B_1	9.115	9.1	9.18	8.337	8.795
	A_1	9.847	9.3	10.45	9.368	10.068
	B_2	10.032				
	A_2	10.374			8.931	9.771
Aceton	A_2	4.3482	4.4	4.4	4.49	4.906
	B_1	9.0245	9.1	9.17	8.196	9.376
	A_2	9.119			7.556	8.579

Molecule	Symmetry	LC-PBE	best est.	CC3	DFTB	LC-DFTB
	A_1	9.381	9.4	9.65	8.308	9.099
	B_2	9.793			7.712	8.443
Benzoquinone	B_{1g}	2.942	2.76	2.75	1.666	2.271
	A_u	3.148	2.77	2.85	2.1	2.921
	B_{3g}	4.556	4.26	4.59	3.743	4.586
	B_{1u}	5.603	5.28	5.62	4.383	5.187
	B_{1g}	6.511			4.696	5.532
Formamide	A''	5.59	5.63	5.65	5.51	5.909
	A'	8.1618	7.39	8.27	8.211	8.7
	A''	9.057				
	A''	9.8443				
	A'	10.22			9.172	9.701
Acetamide	A''	5.635	5.69	5.69	5.513	6.014
	A'	8.123	7.27	7.67	8.031	8.556
	A''	8.914			9.03	9.685
	A'	9.671			9.326	10.299
	A''	9.985			9.201	10.25
Propanamide	A''	5.685	5.72	5.72	5.485	5.985
	A'	8.111	7.2	7.62	7.998	8.574
	A''	8.921			8.391	9.405
	A'	9.74		10.06	8.309	9.531

Molecule	Symmetry	LC-PBE	best est.	CC3	DFTB	LC-DFTB
	A''	9.908			8.971	10.399
Cytosine	A'	5.235	4.66		4.124	4.977
	A''	5.449	4.87		3.357	4.613
	A''	5.995	5.26		4.64	5.62
	A'	6.374	5.62		5.182	6.011
	A''	6.6521			5.022	5.993
Thymine	A''	5.156	4.82		3.789	4.799
	A'	5.581	5.2		4.787	5.578
	A''	6.468	6.16		4.297	5.908
	A'	7.133	6.27		5.194	6.202
	A'	7.237	6.53		6.216	7.228
Uracil	A''	5.122			3.701	4.722
	A'	5.718			4.238	5.817
	A''	6.414			5.147	5.75
	A'	7.104			4.852	6.096
	A'	7.436			5.912	7.535
Adenine	A''	5.532			4.586	5.471
	A'	5.65			4.765	5.415
	A'	5.688			5.088	5.688
	A''	6.17			5.332	6.106
	A''	6.546			5.405	6.279

Table A2: Oscillator strengths of the bright exciations among the five lowest exciations of the molecules in the test set.

Method		LC-ωPBE	DFTB	LC-DFTB
Molecule	Symmetry			
Ethen	B_{1u}	0.38	0.28	0.36
Butadien	B_u	0.72	0.52	0.69
Hexatriene	B_u	1.13	0.84	1.09
Octatetraen	B_u	1.56	1.16	1.5
Cyclopropene	B_2	0.094	0.079	0.12
Cyclopentadiene	B_2	0.089	0.085	0.11
	A_1	0.048	0.058	0.13
Norbornadiene	B_2	0.05	0.01	0.04
	B_2	0.21	0.15	0.26
	B_1	0.01	0.04	0.034
Benzene	E_{1u}	0.59	0.43	0.59
Naphtalene	B_{1u}	0.09	0.012	0.021
	B_{2u}	1.3	0.9	1.23
Furan	B_2	0.14	0.12	0.15
Pyrrole	B_2	0.15	0.11	0.14

Method		LC-ωPBE	DFTB	LC-DFTB
Molecule	Symmetry			
	A_1	0.01	0.01	0.026
	A_1	0.46	0.36	0.47
Imidazole	A'	0.15	0.1	0.14
Pyridine	B_2	0.03	0.025	0.041
	A_1	0.02	0.01	0.0093
Pyrazine	B_{2u}	0.09	0.07	0.1
	B_{1u}	0.072	0.034	0.03
Pyrimidine	B_2	0.033	0.025	0.036
Pyridazine	A_1	0.021	0.021	0.034
Triazine		0.02	0	0
Tetrazine	B_{2u}	0.063	0.059	0.08
Formaldehyde	A_1	0.1	0.22	0.28
Aceton	A_1	0.22	0.23	0.33
	B_2	0.01	0.008	0.00086
Benzoquinone	B_{1u}	0.51	0.26	0.48
Formamide	A'	0.18	0.3	0.35
	A'	0.18	0.07	0.09
Acetamide	A'	0.16	0.24	0.29
	A'	0.097	0.16	0.2
Propanamide	A'	0.15	0.17	0.27

Method		LC-ωPBE	DFTB	LC-DFTB
Molecule	Symmetry			
	A'	0.09	0.097	0.093
Cytosine	A'	0.07	0.015	0.039
	A'	0.21	0.067	0.13
Thymine	A'	0.22	0.078	0.23
	A'	0.062	0.09	0.052
	A'	0.26	0.1	0.15
Uracil	A'	0.21	0.11	0.19
	A'	0.06	0.02	0.05
	A'	0.19	0.09	0.13
Adenine	A'	0.042	0.018	0.009
	A'	0.28	0.17	0.27

Table A3: Energy of the lowest excitation [eV] in a dimer complexes of TCNE and another molecule.

TCNE $\cdots$	exp. [182, 183]	B3LYP [181]	LC-DFTB ($\omega = 0.3$)	LC-ωPBE	pp-DFTB [184]	LC-DFTB ($\omega = 0.25$)	Tuned-BNL [181]
benzene	3.59	2.10	3.86	3.91	3.93	3.58	3.80
toluene	3.36	1.80	3.51	3.59	3.53	3.22	3.40
o-xylene	3.15	1.50	3.27	3.35	2.53	2.988	3
naphthalene	2.6	0.90	3.02	2.93	2.56	2.75	2.7
antracene (anth.)	2.05	1.00	2.27	2.36	1.91	2.05	2.14
9-cyanoanth.	2.33	0.50	2.68	2.65	2.18	2.395	2.35
9-carbo-methoxyanth.	2.16	0.90	2.37	2.42	1.93	2.131	2.16
9-methylanth.	1.87	1.10	2.10	2.18	1.66	1.87	2.03
9,10-dimethylanth.	1.76	1.40	1.92	2.2	1.46	1.707	2.09
9-formylanth.	2.22	1.00	2.51	2.5	2.25	2.278	2.27

L_a	Naphtalene	Anthracene	Tetracene	Pentacene	Hexacene	Heptacene
B3LYP	4.42	3.22	2.43	1.87	1.47	1.17
LC-ωPBE	4.76	3.84	3.04	2.48	2.07	1.77
LC-DFTB	4.78	3.67	2.95	2.46	2.12	1.88
exp.[189]	4.66	3.60	2.88	2.37	2.02	
L_b	Naphtalene	Anthracene	Tetracene	Pentacene	Hexacene	Heptacene
B3LYP	4.52	3.90	3.52	3.26	3.07	2.94
LC-ωPBE	4.99	4.15	3.76	3.49	3.30	3.16
LC-DFTB	4.95	4.35	3.97	3.72	3.54	3.43
exp.[189]	4.13	3.64	3.39	3.12	2.87	

Table A4: L_a and L_b excitation energies [eV] in the polyacenes.

Num. of unit-cells	0.5	1	2	3	4	5
Num. of atoms N_{at}	24	48	96	144	192	240
DFTB (DFTB+)	0.44	3	44.9	444	781	3820
TD-DFTB (DFTB+)	0.48	3.3	47	470	1685	4785
LC-ωPBE/6-31(d,p) (NWCHEM)	5280	32130	150733			

Table A5: Run times [s] of LC-TD-DFTB in DFTB+ and other methods and programs for the calculation the ten lowest singlet excitations in clusters of anthracene molecules of various sizes.

List of Figures

List of Tables

Bibliography

[1] S. R. Forrest. The path to ubiquitous and low-cost organic electronic appliances on plastic. *Nature*, 428(6986):911–918, 2004.

[2] D. J. Gundlach. Organic electronics: Low power, high impact. *Nat. Mater.*, 6(3):173–174, 2007.

[3] E. Stavrinidou, R. Gabrielsson, E. Gomez, X. Crispin, O. Nilsson, D. T. Simon, and M. Berggren. Electronic plants. *Sci. Adv.*, 1(10):e1501136, 2015.

[4] Huanli Dong, Xiaolong Fu, Jie Liu, Zongrui Wang, and Wenping Hu. 25th anniversary article: Key points for high-mobility organic field-effect transistors. *Adv. Mater.*, 25(43): 6158–6183, 2013.

[5] M. E. Gershenson, V. Podzorov, and A. F. Morpurgo. Colloquium: Electronic transport in single-crystal organic transistors. *Rev. Mod. Phys.*, 78(3):973, 2006.

[6] F. So, J. Kido, and P. Burrows. Organic light-emitting devices for solid-state lighting. *MRS Bull.*, 33(7):663–669, 2008.

[7] S. Reineke, F. Lindner, G. Schwartz, N. Seidler, K. Walzer, B. Lussem, and K. Leo. White organic light-emitting diodes with fluorescent tube efficiency. *Nature*, 459(7244): 234–238, 2009.

[8] Y.-J. Cheng, S.-H. Yang, and C.-S. Hsu. Synthesis of conjugated polymers for organic solar cell applications. *Chem. Rev.*, 109(11):5868–5923, 2009.

[9] Y. Sun, G. C. Welch, W. L. Leong, C. J. Takacs, G. C. Bazan, and A. J. Heeger. Solution-processed small-molecule solar cells with 6.7% efficiency. *Nat. Mater.*, 11(1):44–48, 2012.

[10] S. Ciuchi, S. Fratini, and D. Mayou. Transient localization in crystalline organic semi-conductors. *Phys. Rev. B*, 83(8):081202, 2011.

[11] J. Arago and A. Troisi. Dynamics of the excitonic coupling in organic crystals. *Phys. Rev. Lett.*, 114(2):026402, 2015.

[12] J. Arago and A. Troisi. Regimes of exciton transport in molecular crystals in the presence of dynamic disorder. *Adv. Funct. Mater.*, 2015.

[13] T. Kubar and M. Elstner. Coarse-grained time-dependent density functional simulation of charge transfer in complex systems: application to hole transfer in dna. *J. Phys. Chem. B*, 114(34):11221–11240, 2010.

[14] A. Heck, J. J. Kranz, T. Kubar, and M. Elstner. Multi-scale approach to non-adiabatic charge transport in high-mobility organic semiconductors. *J. Chem. Theory Comput.*, 11 (11):5068–5082, 2015.

[15] N. Karl and J. Marktanner. Electron and hole mobilities in high purity anthracene single crystals. *Mol. Cryst. Liq. Cryst.*, 355(1):149–173, 2001.

[16] J. P. Perdew, K. Burke, and M. Ernzerhof. Generalized gradient approximation made simple. *Phys. Rev. Lett.*, 77(18):3865, 1996.

[17] V. Lutsker, B. Aradi, and T. A. Niehaus. Implementation and benchmark of a long-range corrected functional in the density functional based tight-binding method. *J. Chem. Phys.*, 143(18):184107, 2015.

[18] B. Aradi, B. Hourahine, and T. Frauenheim. Dftb+, a sparse matrix-based implementation of the dftb method. *J. Phys. Chem. A*, 111(26):5678–5684, 2007.

[19] J. M. Knaup, B. Hourahine, and T. Frauenheim. Initial steps toward automating the fitting of dftb $e_{rep}(r)$. *J. Phys. Chem. A*, 111(26):5637–5641, 2007.

[20] M. Gaus, C.-P. Chou, H. Witek, and M. Elstner. Automatized parametrization of scc-dftb repulsive potentials: Application to hydrocarbons. *J. Phys. Chem. A*, 113(43):11866–11881, 2009.

[21] C.-P. Chou, Y. Nishimura, C.-C. Fan, G. Mazur, S. Irle, and H. A. Witek. Automatized parameterization of dftb using particle swarm optimization. *J. Chem. Theory Comput.*, 12(1):53–64, 2015.

[22] P. Hohenberg and W. Kohn. Inhomogeneous electron gas. *Phys. Rev.*, 136(3B):B864, 1964.

[23] E. H. Lieb. Density functionals for coulomb systems. *Int. J. Quant. Chem.*, 24(3):243–277, 1983.

[24] J. F. Janak. Proof that $\frac{\partial e}{\partial n_i} = \varepsilon$ in density-functional theory. *Phys. Rev. B*, 18(12):7165, 1978.

[25] R. Stowasser and R. Hoffmann. What do the kohn-sham orbitals and eigenvalues mean? *J. Am. Chem. Soc.*, 121(14):3414–3420, 1999.

[26] L. H. Thomas. The calculation of atomic fields. In *Math. Proc. Cambridge Philos. Soc.*, volume 23, pages 542–548. Cambridge University Press, 1927.

[27] E. Fermi. Un metodo statistico per la determinazione di alcune priorieta dell'atome. *Rend. Accad. Naz. Lincei*, 6(602-607):32, 1927.

[28] R. Van Noorden, B. Maher, and R. Nuzzo. The top 100 papers. *Nature*, 514(7524):550, 2014.

[29] W. Kohn and L. J. Sham. Self-consistent equations including exchange and correlation effects. *Phys. Rev.*, 140(4A):A1133, 1965.

[30] P. A. M. Dirac. Note on exchange phenomena in the thomas atom. In *Mathematical Proceedings of the Cambridge Philosophical Society*, volume 26, pages 376–385. Cambridge University Press, 1930.

[31] D. M. Ceperley and B. J. Alder. Ground state of the electron gas by a stochastic method. *Phys. Rev. Lett.*, 45(7):566, 1980.

[32] S. H. Vosko, L. Wilk, and M. Nusair. Accurate spin-dependent electron liquid correlation energies for local spin density calculations: a critical analysis. *Canadian J. Phys.*, 58(8): 1200–1211, 1980.

[33] J. P. Perdew and A. Zunger. Self-interaction correction to density-functional approximations for many-electron systems. *Phys. Rev. B*, 23(10):5048, 1981.

[34] J. P. Perdew and Y. Wang. Accurate and simple analytic representation of the electron-gas correlation energy. *Phys. Rev. B*, 45(23):13244, 1992.

[35] J. P. Perdew, R. G. Parr, M. Levy, and J. L. Balduz Jr. Density-functional theory for fractional particle number: derivative discontinuities of the energy. *Phys. Rev. Lett.*, 49 (23):1691, 1982.

[36] J. P. Perdew, M. Ernzerhof, and K. Burke. Rationale for mixing exact exchange with density functional approximations. *J. Chem. Phys.*, 105(22):9982–9985, 1996.

[37] C. Adamo and V. Barone. Toward reliable density functional methods without adjustable parameters: The pbe0 model. *J. Chem. Phys.*, 110:6158, 1999.

[38] C. Lee, W. Yang, and R. G. Parr. Development of the colle-salvetti correlation-energy formula into a functional of the electron density. *Phys. Rev. B*, 37(2):785, 1988.

[39] A. D. Becke. Density-functional exchange-energy approximation with correct asymptotic behavior. *Phys. Rev. A*, 38(6):3098, 1988.

[40] P. J. Stephens, F. J. Devlin, C. F. Chabalowski, and M. J. Frisch. Ab initio calculation of vibrational absorption and circular dichroism spectra using density functional force fields. *J. Phys. Chem.*, 98(45):11623–11627, 1994.

[41] E. Engel, J. A. Chevary, L. D. Macdonald, and S. H. Vosko. Asymptotic properties of the exchange energy density and the exchange potential of finite systems: relevance for generalized gradient approximations. *Z. Phys. At. Mol. Clust.*, 23(1):7–14, 1992.

[42] H. Sekino, Y. Maeda, and M. Kamiya. Influence of the long-range exchange effect on dynamic polarizability. *Mol. Phys.*, 103(15-16):2183–2189, 2005.

[43] M. Kamiya, H. Sekino, T. Tsuneda, and K. Hirao. Nonlinear optical property calculations by the long-range-corrected coupled-perturbed kohn–sham method. *J. Chem. Phys.*, 122 (23):234111, 2005.

[44] H. Sekino, Y. Maeda, M. Kamiya, and K. Hirao. Polarizability and second hyperpolarizability evaluation of long molecules by the density functional theory with long-range correction. *J. Chem. Phys.*, 126(1):014107, 2007.

[45] S. Refaely-Abramson, S. Sharifzadeh, N. Govind, J. Autschbach, J. B. Neaton, R. Baer, and L. Kronik. Quasiparticle spectra from a nonempirical optimally tuned range-separated hybrid density functional. *Phys. Rev. Lett.*, 109:226405, 2012.

[46] T. Korzdorfer, R. M. Parrish, J. S. Sears, C. D. Sherrill, and J.-L. Bredas. On the relationship between bond-length alternation and many-electron self-interaction error. *J. Chem. Phys.*, 137(12):124305, 2012.

[47] B. G. Levine, C. Ko, J. Quenneville, and T. J. Martinez. Conical intersections and double excitations in time-dependent density functional theory. *Mol. Phys.*, 104(5-7):1039–1051, 2006.

[48] F. Cordova, L. J. Doriol, A. Ipatov, M. E. Casida, C. Filippi, and A. Vela. Troubleshooting time-dependent density-functional theory for photochemical applications: Oxirane. *J. Chem. Phys.*, 127(16):164111, 2007.

[49] M. E. Casida and M. Huix-Rotllant. Progress in time-dependent density-functional theory. *Annu. Rev. Phys. Chem.*, 63:287, 2012.

[50] M. E. Casida. *Recent Advances in Density Functional Methods, Part I*, chapter Time-dependent Density Functional Response Theory for Molecules, pages 155–192. World Scientific, Singapore, 1995.

[51] F. Furche and R. Ahlrichs. Adiabatic time-dependent density functional methods for excited state properties. *J. Chem. Phys.*, 117(16):7433–7447, 2002.

[52] D. Porezag, T. Frauenheim, T. Koehler, G. Seifert, and R. Kaschner. Construction of tight-binding-like potentials on the basis of density-functional theory: Application to carbon. *Phys. Rev. B*, 51(19):12947, 1995.

[53] M. Elstner, D. Porezag, G. Jungnickel, J. Elsner, M. Haugk, T. Frauenheim, S. Suhai, and G. Seifert. Self-consistent-charge density-functional tight-binding method for simulations of complex materials properties. *Phys. Rev. B*, 58(11):7260, 1998.

[54] M. Gaus, Q. Cui, and M. Elstner. Dftb3: extension of the self-consistent-charge density-functional tight-binding method (scc-dftb). *J. Chem. Theory Comput.*, 7(4):931–948, 2011.

[55] R. S. Mulliken. Electronic population analysis on lcao–mo molecular wave functions. i. *J. Chem. Phys.*, 23(10):1833–1840, 1955.

[56] M. Wahiduzzaman, A. F. Oliveira, P. Philipsen, L. Zhechkov, E. Van Lenthe, H. A. Witek, and T. Heine. Dftb parameters for the periodic table: Part 1, electronic structure. *J. Chem. Theory Comput.*, 9(9):4006–4017, 2013.

[57] T. A. Niehaus and F. Della Sala. Range separated functionals in the density functional based tight-binding method: Formalism. *Phys. Status Solidi B*, 249:237, 2012.

[58] R. Baer and D. Neuhauser. Density functional theory with correct long-range asymptotic behavior. *Phys. Rev. Lett.*, 94:043002, 2005.

[59] E. Livshits and R. Baer. A well-tempered density functional theory of electrons in molecules. *Phys. Chem. Chem. Phys.*, 9:2932–2941, 2007.

[60] B. Hess, C. Kutzner, D. Van Der Spoel, and E. Lindahl. Gromacs 4: algorithms for highly efficient, load-balanced, and scalable molecular simulation. *J. Chem. Theory Comput.*, 4 (3):435–447, 2008.

[61] R. W. Hockney, S. P. Goel, and J. W. Eastwood. Quiet high-resolution computer models of a plasma. *J. Comput. Phys.*, 14(2):148–158, 1974.

[62] S. Nose. A molecular dynamics method for simulations in the canonical ensemble. *Mol. Phys.*, 52(2):255–268, 1984.

145

[63] W. G. Hoover. Canonical dynamics: equilibrium phase-space distributions. *Phys. Rev. A*, 31(3):1695, 1985.

[64] M. Parrinello and A. Rahman. Polymorphic transitions in single crystals: A new molecular dynamics method. *J. Appl. Phys.*, 52(12):7182–7190, 1981.

[65] S. Nose and M. L. Klein. Constant pressure molecular dynamics for molecular systems. *Mol. Phys.*, 50(5):1055–1076, 1983.

[66] T. Holstein. Studies of polaron motion: Part i. the molecular-crystal model. *Ann. Phys.*, 8(3):325–342, 1959.

[67] K. Hannewald, V. M. Stojanovic, J. M. T. Schellekens, P. A. Bobbert, G. Kresse, and J. Hafner. Theory of polaron bandwidth narrowing in organic molecular crystals. *Phys. Rev. B*, 69(7):075211, 2004.

[68] A. Troisi. Prediction of the absolute charge mobility of molecular semiconductors: the case of rubrene. *Adv. Mat.*, 19(15):2000–2004, 2007.

[69] R. P. Fornari, J. Arago, and A. Troisi. A very general rate expression for charge hopping in semiconducting polymers. *J. Chem. Phys.*, 142(18):184105, 2015.

[70] M. D. Newton and N. Sutin. Electron transfer reactions in condensed phases. *Ann. Rev. Phys. Chem.*, 35(1):437–480, 1984.

[71] B. S. Brunschwig, J. Logan, M. D. Newton, and N. Sutin. A semiclassical treatment of electron-exchange reactions. application to the hexaaquoiron (ii)-hexaaquoiron (iii) system. *J. Am. Chem. Soc.*, 102(18):5798–5809, 1980.

[72] L. D. Zusman. Outer-sphere electron transfer in polar solvents. *Chem. Phys.*, 49(2):295–304, 1980.

[73] A. Warshel. Dynamics of reactions in polar solvents. semiclassical trajectory studies of electron-transfer and proton-transfer reactions. *J. Phys. Chem.*, 86(12):2218–2224, 1982.

[74] L. D. Landau. Zur theorie der energieubertragung. ii. *Phys. Z. Sowjetunion*, 2(46):1–13, 1932.

[75] C. Zener. Non-adiabatic crossing of energy levels. In *Proc. Royal Soc. London A*, volume 137, pages 696–702. The Royal Society, 1932.

[76] J. Spencer, L. Scalfi, A. Carof, and J. Blumberger. Confronting surface hopping molecular dynamics with marcus theory for a molecular donor–acceptor system. *Faraday disc.*, 195:215–236, 2017.

[77] J. J. Kwiatkowski, J. Nelson, H. Li, J. L. Bredas, W. Wenzel, and C. Lennartz. Simulating charge transport in tris (8-hydroxyquinoline) aluminium (alq 3). *Phys. Chem. Chem. Phys.*, 10(14):1852–1858, 2008.

[78] P. Friederich, V. Meded, A. Poschlad, T. Neumann, V. Rodin, V. Stehr, F. Symalla, D. Danilov, G. Ludemann, R. F. Fink, et al. Molecular origin of the charge carrier mobility in small molecule organic semiconductors. *Adv. Mat.*, 26(31):5757–5763, 2016.

[79] V. Ruhle, A. Lukyanov, F. May, M. Schrader, T. Vehoff, J. Kirkpatrick, B. Baumeier, and D. Andrienko. Microscopic simulations of charge transport in disordered organic semiconductors. *J. Chem. Theory Comput.*, 7(10):3335, 2011.

[80] P. Kordt, J. J. M. Van der Holst, M. Al Helwi, W. Kowalsky, F. May, A. Badinski, C. Lennartz, and D. Andrienko. Modeling of organic light emitting diodes: From molecular to device properties. *Adv. Mat.*, 25(13):1955–1971, 2015.

[81] V. Stehr, R. F. Fink, B. Engels, J. Pflaum, and C. Deibel. Singlet exciton diffusion in organic crystals based on marcus transfer rates. *J. Chem. Theory Comput.*, 10(3):1242–1255, 2014.

[82] T. Foerster. Zwischenmolekulare energiewanderung und fluoreszenz. *Ann. Phys.*, 437 (1-2):55–75, 1948.

[83] O. V. Mikhnenko, P. W. M. Blom, and T.-Q. Nguyen. Exciton diffusion in organic semiconductors. *Energy Environ. Sci.*, 8(7):1867–1888, 2015.

[84] F. Bloch. Über die quantenmechanik der elektronen in kristallgittern. *Z. Phys. A*, 52(7): 555–600, 1929.

[85] C. Kittel. *Introduction to solid state physics*. Wiley, 2005.

[86] A. Troisi. The speed limit for sequential charge hopping in molecular materials. *Org. Elec.*, 12(12):1988–1991, 2011.

[87] J. Spencer, F. Gajdos, and J. Blumberger. Fob-sh: Fragment orbital-based surface hopping for charge carrier transport in organic and biological molecules and materials. *J. Chem. Phys.*, 145(6):064102, 2016.

[88] T. Kubar and M. Elstner. Efficient algorithms for the simulation of non-adiabatic electron transfer in complex molecular systems: application to dna. *Phys. Chem. Chem. Phys.*, 15 (16):5794–5813, 2013.

[89] T. Kubar, U. Kleinekathofer, and M. Elstner. Solvent fluctuations drive the hole transfer in dna: A mixed quantum- classical study. *J. Phys. Chem. B*, 113(39):13107–13117, 2009.

[90] T. Kubar and M. Elstner. Coarse-grained time-dependent density functional simulation of charge transfer in complex systems: application to hole transfer in dna. *J. Phys. Chem. B*, 114(34):11221–11240, 2010.

[91] A. Heck, P. B. Woiczikowski, T. Kubar, K. Welke, T. Niehaus, B. Giese, S. Skourtis, M. Elstner, and T. B. Steinbrecher. Fragment orbital based description of charge transfer in peptides including backbone orbitals. *J. Phys. Chem. B*, 118(16):4261–4272, 2014.

[92] V. Coropceanu, J. Cornil, D. A. da Silva Filho, Y. Olivier, R. Silbey, and J.-L. Bredas. Charge transport in organic semiconductors. *Chem. Rev.*, 107(4):926–952, 2007.

[93] A. Kubas, F. Hoffmann, A. Heck, H. Oberhofer, M. Elstner, and J. Blumberger. Electronic couplings for molecular charge transfer: Benchmarking cdft, fodft, and fodftb against high-level ab initio calculations. *J. Chem. Phys.*, 140(10):104105, 2014.

[94] A. Kubas, F. Gajdos, A. Heck, H. Oberhofer, M. Elstner, and J. Blumberger. Electronic couplings for molecular charge transfer: benchmarking cdft, fodft and fodftb against high-level ab initio calculations. ii. *Phys. Chem. Chem. Phys.*, 17(22):14342–14354, 2015.

[95] P. V. Parandekar and J. C. Tully. Mixed quantum-classical equilibrium. *J. Chem. Phys.*, 122(9):094102, 2005.

[96] K. Hannewald and P. A. Bobbert. Ab-initio theory of charge transport in organic crystals. In *AIP Conference Proceedings*, volume 772, pages 1101–1104. AIP, 2005.

[97] V. Stehr, R. F. Fink, M. Tafipolski, C. Deibel, and B. Engels. Comparison of different rate constant expressions for the prediction of charge and energy transport in oligoacenes. *Comput. Mol. Sci.*, 6(6):694–720, 2016.

[98] C. I. Bayly, P. Cieplak, W. Cornell, and P. A. Kollman. A well-behaved electrostatic potential based method using charge restraints for deriving atomic charges: the resp model. *J. Phys. Chem.*, 97(40):10269–10280, 1993.

[99] J. Wang, R. M. Wolf, J. W. Caldwell, P. A. Kollman, and D. A. Case. Development and testing of a general amber force field. *J. Comput. Chem.*, 25(9):1157–1174, 2004.

[100] A. Nemkevich, H.-B. Buergi, M. A. Spackman, and B. Corry. Molecular dynamics simulations of structure and dynamics of organic molecular crystals. *Phys. Chem. Chem. Phys.*, 12(45):14916–14929, 2010.

[101] A. Heck, J. J. Kranz, and M. Elstner. Simulation of temperature-dependent charge transport in organic semiconductors with various degrees of disorder. *J. Chem. Theory Comput.*, 12(7):3087–3096, 2016.

[102] C. Deibel and V. Dyakonov. Polymer-fullerene bulk heterojunction solar cells. *Rep. Prog. Phys.*, 73(9):096401, 2010.

[103] G. Chidichimo and L. Filippelli. Organic solar cells: problems and perspectives. *Int. J. Photoenergy*, 2010, 2010.

[104] G. Dennler, M. C. Scharber, and C. J. Brabec. Polymer-fullerene bulk-heterojunction solar cells. *Adv. Mater*, 21(13):1323–1338, 2009.

[105] B. Kippelen and J.-L. Bredas. Organic photovoltaics. *Energy Environ. Sci.*, 2(3):251–261, 2009.

[106] M. Riede, T. Mueller, W. Tress, R. Schueppel, and K. Leo. Small-molecule solar cells–status and perspectives. *Nanotechnology*, 19(42):424001, 2008.

[107] S. M. Menke and R. J. Holmes. Exciton diffusion in organic photovoltaic cells. *Energy Environ. Sci.*, 7(2):499–512, 2014.

[108] D. Moses, J. Wang, A. J. Heeger, N. Kirova, and S. Brazovski. Singlet exciton binding energy in poly (phenylene vinylene). *Proc. Natl. Acad. Sci. U. S. A.*, 98(24):13496–13500, 2001.

[109] R. N. Marks, J. J. M. Halls, D. D. C. Bradley, R. H. Friend, and A. B. Holmes. The photovoltaic response in poly (p-phenylene vinylene) thin-film devices. *J. Phys.: Condens. Matter*, 6(7):1379, 1994.

[110] V. May and O. Kuehn. *Charge and energy transfer dynamics in molecular systems*. John Wiley & Sons, 2008.

[111] R. Silbey and R. W. Munn. General theory of electronic transport in molecular crystals. i. local linear electron–phonon coupling. *J. Chem. Phys.*, 72(4):2763–2773, 1980.

[112] R. W. Munn and R. Silbey. Theory of electronic transport in molecular crystals. ii. zeroth order states incorporating nonlocal linear electron–phonon coupling. *J. Chem. Phys.*, 83 (4):1843–1853, 1985.

[113] H. Haken and G. Strobl. An exactly solvable model for coherent and incoherent exciton motion. *Z. Phys.*, 262(2):135–148, 1973.

[114] H. Haken and P. Reineker. The coupled coherent and incoherent motion of excitons and its influence on the line shape of optical absorption. *Z. Phys.*, 249(3):253–268, 1972.

[115] A. Eisfeld, S. M. Vlaming, V. A. Malyshev, and J. Knoester. Excitons in molecular aggregates with lévy-type disorder: Anomalous localization and exchange broadening of optical spectra. *Phys. Rev. Lett.*, 105(13):137402, 2010.

[116] D. Fazzi, M. Barbatti, and W. Thiel. Modeling ultrafast exciton deactivation in olig-othiophenes via nonadiabatic dynamics. *Phys. Chem. Chem. Phys.*, 17(12):7787–7799, 2015.

[117] C. Olbrich and U. Kleinekathofer. Time-dependent atomistic view on the electronic relaxation in light-harvesting system ii. *J. Phys. Chem. B*, 114(38):12427–12437, 2010.

[118] H. Zhu, V. May, and B. Roeder. Mixed quantum classical simulations of electronic excitation energy transfer: The pheophorbide-a dab dendrimer p4 in solution. *Chem. Phys.*, 351(1):117–128, 2008.

[119] H. Zhu, V. May, B. Roeder, M. E.-A. Madjet, and T. Renger. The pheophorbide-a dab dendrimer p 4 in solution: Md-simulations based studies of exciton states. *Chem. Phys. Lett.*, 444(1):118–124, 2007.

[120] O. Postupna, R. Long, and O. V. Prezhdo. Time-domain ab initio simulation of energy transfer in double-walled carbon nanotubes. *J. Phys. Chem. C*, 119(21):12088–12094, 2015.

[121] T. Kubar and M. Elstner. A hybrid approach to simulation of electron transfer in complex molecular systems. *J. R. Soc., Interface*, 10(87):20130415, 2013.

[122] T. Kubar, R. Gutierrez, U. Kleinekathofer, G. Cuniberti, and M. Elstner. Modeling charge transport in dna using multi-scale methods. *Phys. Status Solidi B*, 250(11):2277–2287, 2013.

[123] J. C. Tully. Molecular dynamics with electronic transitions. *J. Chem. Phys.*, 93(2):1061–1071, 1990.

[124] A. Bastida, C. Cruz, J. Zuniga, A. Requena, and B. Miguel. A modified ehrenfest method that achieves boltzmann quantum state populations. *Chem. Phys. Lett.*, 417(1):53–57, 2006.

[125] A. Bastida, C. Cruz, J. Zuniga, A. Requena, and B. Miguel. The ehrenfest method with quantum corrections to simulate the relaxation of molecules in solution: Equilibrium and dynamics. *J. Chem. Phys.*, 126(1):014503, 2007.

[126] W. Liu, V. Settels, P. H. P. Harbach, A. Dreuw, R. F. Fink, and B. Engels. Assessment of td-dft-and td-hf-based approaches for the prediction of exciton coupling parameters, potential energy curves, and electronic characters of electronically excited aggregates. *J. Comput.. Chem.*, 32(9):1971–1981, 2011.

[127] J. Frenkel. On the transformation of light into heat in solids. i. *Phys. Rev.*, 37(1):17, 1931.

[128] M. E. Casida. Response theory for molecules. *Recent Advances in Density Functional Methods:(Part I)*, 1:155, 1995.

[129] T. A. Niehaus, S. Suhai, F. Della Sala, P. Lugli, M. Elstner, G. Seifert, and T. Frauenheim. Tight-binding approach to time-dependent density-functional response theory. *Phys. Rev. B*, 63(8):085108, 2001.

[130] C. Koenig and J. Neugebauer. Exciton coupling mechanisms analyzed with subsystem tddft: Direct vs pseudo exchange effects. *J. Phys. Chem. B*, 117(13):3480–3487, 2013.

[131] D. Beljonne, Ca. Curutchet, G. D. Scholes, and R. J. Silbey. Beyond forster resonance energy transfer in biological and nanoscale systems. *J. Phys. Chem. B*, 113(19):6583–6599, 2009.

[132] V. Stehr, B. Engels, C. Deibel, and R. F. Fink. Anisotropy of singlet exciton diffusion in organic semiconductor crystals from ab initio approaches. *J. Chem. Phys.*, 140(2): 024503, 2014.

[133] X. Zhang, Z. Li, and G. Lu. First-principles simulations of exciton diffusion in organic semiconductors. *Phys. Rev. B*, 84(23):235208, 2011.

[134] E. R. Davidson. The iterative calculation of a few of the lowest eigenvalues and corresponding eigenvectors of large real-symmetric matrices. *J. Comput. Phys.*, 17(1):87–94, 1975.

[135] P.-A. Ploetz, T. Niehaus, and O. Kuehn. A new efficient method for calculation of frenkel exciton parameters in molecular aggregates. *J. Chem. Phys.*, 140(17):174101, 2014.

[136] D. Heringer, T. A. Niehaus, M. Wanko, and T. Frauenheim. Analytical excited state forces for the time-dependent density-functional tight-binding method. *J. Comput. Chem.*, 28(16):2589–2601, 2007.

[137] A. V. Akimov and O. V. Prezhdo. The pyxaid program for non-adiabatic molecular dynamics in condensed matter systems. *J. Chem. Theory Comput.*, 9(11):4959–4972, 2013.

[138] B. R. Landry and J. E. Subotnik. Communication: Standard surface hopping predicts incorrect scaling for marcus' golden-rule rate: The decoherence problem cannot be ignored. *J. Chem. Phys.*, 135(19):191101, 2011.

[139] G. Granucci and M. Persico. Critical appraisal of the fewest switches algorithm for surface hopping. *J. Chem. Phys.*, 126(13):134114, 2007.

[140] C. Zhu, S. Nangia, A. W. Jasper, and D. G. Truhlar. Coherent switching with decay of mixing: an improved treatment of electronic coherence for non-born–oppenheimer trajectories. *J. Chem. Phys.*, 121(16):7658–7670, 2004.

[141] L. Wang and D. Beljonne. Charge transport in organic semiconductors: Assessment of the mean field theory in the hopping regime. *J. Chem. Phys.*, 139(6):064316, 2013.

[142] L. Wang and D. Beljonne. Flexible surface hopping approach to model the crossover from hopping to band-like transport in organic crystals. *J. Phys. Chem. Lett.*, 4(11): 1888–1894, 2013.

[143] J. S. Meth, C. D. Marshall, and M. D. Fayer. An examination of radiative and nonradiative excitation transport in thin anthracene crystals: Transient grating experiments. *Solid State Commun.*, 74(4):281–284, 1990.

[144] B. J. Mulder. Anisotropy of light absorption and exciton diffusion in anthracene crystals determined from the externally sensitized fluorescence. *Philips Res. Rep.*, 22:142, 1967.

[145] R. C. Powell and Z. G. Soos. Singlet exciton energy transfer in organic solids. *J. Lumin.*, 11(1):1–45, 1975.

[146] H. Yamagata, J. Norton, E. Hontz, Y. Olivier, D. Beljonne, J.-L. Bredas, R. J. Silbey, and F. C. Spano. The nature of singlet excitons in oligoacene molecular crystals. *J. Chem. Phys.*, 134(20):204703, 2011.

[147] S. Grimme and M. Parac. Substantial errors from time-dependent density functional theory for the calculation of excited states of large π systems. *ChemPhysChem*, 4(3): 292–295, 2003.

[148] B. M. Wong and T. H. Hsieh. Optoelectronic and excitonic properties of oligoacenes: substantial improvements from range-separated time-dependent density functional theory. *J. Chem. Theory Comput.*, 6(12):3704–3712, 2010.

[149] J. Arago, J. C. Sancho-Garcia, E. Orti, and D. Beljonne. Ab initio modeling of donor–acceptor interactions and charge-transfer excitations in molecular complexes: The case of terthiophene–tetracyanoquinodimethane. *J. Chem. Theory Comput.*, 7(7):2068–2077, 2011.

[150] M. R. Silva-Junior, M. Schreiber, S. P. A. Sauer, and W. Thiel. Benchmarks for electronically excited states: Time-dependent density functional theory and density functional theory based multireference configuration interaction. *J. Chem. Phys.*, 129(10):104103, 2008.

[151] M. Wanko, M. Garavelli, F. Bernardi, T. A. Niehaus, T. Frauenheim, and M. Elstner. A global investigation of excited state surfaces within time-dependent density-functional response theory. *J. Chem. Phys.*, 120(4):1674–1692, 2004.

[152] W. M. Young and E. W. Elcock. Monte carlo studies of vacancy migration in binary ordered alloys: I. *Proc. Phys. Soc.*, 89(3):735, 1966.

[153] G. I. Csonka, J. P. Perdew, and A. Ruzsinszky. Global hybrid functionals: A look at the engine under the hood. *J. Chem. Theory Comput.*, 6(12):3688–3703, 2010.

[154] Peter M. W. Gill, Ross D. Adamason, and John A. Pople. Coulomb-attenuated exchange energy density functionals. *Mol. Phys.*, 88(4):1005–1009, 1996.

[155] A. Savin. *Recent Developments and Applications of Modern Density Functional Theory*, pages 327–357. Elsevier, Amsterdam, 1996.

[156] T. Leininger, H. Stoll, H.-J. Werner, and A. Savin. Combining long-range configuration interaction with short-range density functionals. *Chem. Phys. Lett.*, 275:151, 1997.

[157] T. Yanai, D. P. Tew, and N. C. Handy. A new hybrid exchange-correlation functional using the coulomb-attenuating method (cam-b3lyp). *Chem. Phys. Lett.*, 393(1-3):51–57, 2004.

[158] H. Iikura, T. Tsuneda, T. Yanai, and K. Hirao. A long-range correction scheme for generalized-gradient-approximation exchange functionals. *J. Chem. Phys.*, 115:3540, 2001.

[159] R. Baer, E. Livshits, and U. Salzner. Tuned range-separated hybrids in density functional theory. *Annu. Rev. Phys. Chem.*, 61:85–109, 2010.

[160] L. Kronik and S. Kuemmel. Gas-phase valence-electron photoemission spectroscopy using density functional theory. In C. di Valentin, S. Botti, and M. Coccoccioni, editors,

Topics of Current Chemistry: First Principles Approaches to Spectroscopic Properties of Complex Materials, volume 347, pages 137–192. Springer. Berlin, 2014.

[161] N. Kuritz, T. Stein, R. Baer, and L. Kronik. Charge-transfer-like $\pi \to \pi^*$ excitations in time-dependent density functional theory: a conundrum and its solution. *J. Chem. Theory Comput.*, 7(8):2408–2415, 2011.

[162] A. Dreuw, J. L. Weisman, and M. Head-Gordon. Long-range charge-transfer excited states in time-dependent density functional theory require non-local exchange. *J. Chem. Phys.*, 119:2943, 2003.

[163] A. Humeniuk and R. Mitric. Long-range correction for tight-binding td-dft. *J. Chem. Phys.*, 143(13):134120, 2015.

[164] T. A. Niehaus. Approximate time-dependent density functional theory. *J. Mol. Struct.: THEOCHEM*, 914:38, 2009.

[165] F. Furche and R. Ahlrichs. Adiabatic time-dependent density functional methods for excited state properties. *J. Chem. Phys.*, 117(16):7433–7447, October 2002.

[166] C. A. Ullrich. *Time-Dependent Density-Functional Theory: Concepts and Applications.* Oxford University Press, USA, 2012.

[167] C. Koehler, G. Seifert, and T. Frauenheim. Density functional based calculations for fe n ($n <= 32$). *Chem. Phys.*, 309(1):23–31, 2005.

[168] A. Dominguez, B. Aradi, T. Frauenheim, V. Lutsker, and T. A. Niehaus. Extensions of the time-dependent density functional based tight-binding approach. *J. Chem. Theory Comput.*, 9(11):4901–4914, 2013.

[169] C. Koehler, G. Seifert, U. Gerstmann, M. Elstner, H. Overhof, and T. Frauenheim. Approximate density-functional calculations of spin densities in large molecular systems and complex solids. *Phys. Chem. Chem. Phys.*, 3(23):5109–5114, 2001.

[170] T. A. Niehaus, S. Suhai, F. Della Sala, P. Lugli, M. Elstner, G. Seifert, and T. Frauenheim. Tight-binding approach to time-dependent density-functional response theory. *Phys. Rev. B*, 63(8):085108, February 2001.

[171] R. E. Stratmann, G. E. Scuseria, and M. J. Frisch. An efficient implementation of time-dependent density-functional theory for the calculation of excitation energies of large molecules. *J. Chem. Phys.*, 109(19):8218–8224, 1998.

[172] M. Elstner and G. Seifert. Density functional tight binding. *Phil. Trans. Royal Soc. A*, 372(2011):20120483, 2014.

[173] M. Elstner, D. Porezag, G. Jungnickel, J. Elsner, M. Haugk, T. Frauenheim, S. Suhai, and G. Seifert. Self-consistent-charge density-functional tight-binding method for simulations of complex materials properties. *Phys. Rev. B*, 58(11):7260–7268, 1998.

[174] M. Schreiber, M. R. Silva-Junior, S. P. A. Sauer, and W. Thiel. Benchmarks for electronically excited states: Caspt2, cc2, ccsd, and cc3. *J. Chem. Phys.*, 128:134110, 2008.

[175] O. A. Vydrov and G. E. Scuseria. Assessment of a long-range corrected hybrid functional. *The Journal of Chemical Physics*, 125:234109, 2006.

[176] T. Yanai, D. P. Tew, and N. C. Handy. A new hybrid exchange-correlation functional using the coulomb-attenuating method (cam-b3lyp). *Chem. Phys. Lett.*, 393(1):51–57, 2004.

[177] J.-D. Chai and M. Head-Gordon. Systematic optimization of long-range corrected hybrid density functionals. *J. Chem. Phys.*, 128(8):084106, 2008.

[178] M. J. Frisch, G. W. Trucks, H. B. Schlegel, G. E. Scuseria, M. A. Robb, J. R. Cheeseman, G. Scalmani, V. Barone, B. Mennucci, G. A. Petersson, H. Nakatsuji, M. Caricato, X. Li, H. P. Hratchian, A. F. Izmaylov, J. Bloino, G. Zheng, J. L. Sonnenberg, M. Hada, M. Ehara, K. Toyota, R. Fukuda, J. Hasegawa, M. Ishida, T. Nakajima, Y. Honda, O. Kitao, H. Nakai, T. Vreven, J. A. Montgomery, Jr., J. E. Peralta, F. Ogliaro, M. Bearpark, J. J. Heyd, E. Brothers, K. N. Kudin, V. N. Staroverov, R. Kobayashi, J. Normand, K. Raghavachari, A. Rendell, J. C. Burant, S. S. Iyengar, J. Tomasi, M. Cossi, N. Rega, J. M. Millam, M. Klene, J. E. Knox, J. B. Cross, V. Bakken, C. Adamo, J. Jaramillo, R. Gomperts, R. E. Stratmann, O. Yazyev, A. J. Austin, R. Cammi, C. Pomelli, J. W. Ochterski, R. L. Martin, K. Morokuma, V. G. Zakrzewski, G. A. Voth, P. Salvador, J. J. Dannenberg, S. Dapprich, A. D. Daniels, O. Farkas, J. B. Foresman, J. V. Ortiz, J. Cioslowski, and D. J. Fox. Gaussian-09 revision d.01. Gaussian Inc. Wallingford CT 2009.

[179] D. Jacquemin, V. Wathelet, E. A. Perpete, and C. Adamo. Extensive TD-DFT Benchmark: Singlet-Excited States of Organic Molecules. *J. Chem. Theory Comput.*, 5(9): 2420–2435, 2009.

[180] R. S. Mulliken. Structures of complexes formed by halogen molecules with aromatic and with oxygenated solvents1. *J. Am. Chem. Soc.*, 72(1):600–608, 1950.

[181] T. Stein, L. Kronik, and R. Baer. Reliable prediction of charge transfer excitations in molecular complexes using time-dependent density functional theory. *J. Am. Chem. Soc.*, 131(8):2818–2820, 2009.

[182] I. Hanazaki. Vapor-phase electron donor-acceptor complexes of tetracyanoethylene and of sulfur dioxide. *J. Phys. Chem.*, 76(14):1982–1989, 1972.

[183] J. M. Masnovi, E. A. Seddon, and J. K. Kochi. Electron transfer from anthracenes. comparison of photoionization, charge-transfer excitation and electrochemical oxidation. *Can. J. Chem.*, 62(11):2552–2559, 1984.

[184] Y. Yang, A. Dominguez, D. Zhang, V. Lutsker, T. A. Niehaus, T. Frauenheim, and W. Yang. Charge transfer excitations from particle-particle random phase approximation-opportunities and challenges arising from two-electron deficient systems. *J. Phys. Chem.*, 146(12):124104, 2017.

[185] H. van Aggelen, Y. Yang, and W. Yang. *Phys. Rev. A*, 88:030501, 2013.

[186] H. van Aggelen, Y. Yang, and Weitao Yang. *J. Chem. Phys.*, 140:18A511, 2014.

[187] Oana D Jurchescu, Jacob Baas, and Thomas TM Palstra. Effect of impurities on the mobility of single crystal pentacene. *Appl. Phys. Let.*, 84(16):3061–3063, 2004.

[188] S. Grimme and M. Parac. Substantial errors from time-dependent density functional theory for the calculation of excited states of large π-systems. *ChemPhysChem*, 4(3): 292–295, 2003.

[189] D. Biermann and W. Schmidt. Diels-alder reactivity of polycyclic aromatic hydrocarbons. 1. acenes and benzologs. *J. Am. Chem. Soc.*, 102(9):3163–3173, 1980.

[190] M. Valiev, E. J. Bylaska, N. Govind, K. Kowalski, T. P. Straatsma, H. J. J. Van Dam, D. Wang, J. Nieplocha, E. Apra, and T. L. Windus. Nwchem: a comprehensive and scalable open-source solution for large scale molecular simulations. *Comput. Phys. Commun.*, 181(9):1477, 2010.

[191] W. E. Arnoldi. The principle of minimized iterations in the solution of the matrix eigenvalue problem. *Quart. Appl. Math.*, 9(1):17, 1951.

[192] M. P. Repasky, J. Chandrasekhar, and W. L. Jorgensen. Pddg/pm3 and pddg/mndo: improved semiempirical methods. *J. Comput. Chem.*, 23(16):1601–1622, 2002.

[193] M. Korth and W. Thiel. Benchmarking semiempirical methods for thermochemistry, kinetics, and noncovalent interactions: Omx methods are almost as accurate and robust as dft-gga methods for organic molecules. *J. Chem. Theory Comput.*, 7(9):2929–2936, 2011.

[194] M. Gaus, A. Goez, and M. Elstner. Parametrization and benchmark of dftb3 for organic molecules. *J. Chem. Theory Comput.*, 9(1):338–354, 2012.

[195] A. S. Christensen, T. Kubar, Q. Cui, and M. Elstner. Semiempirical quantum mechanical methods for noncovalent interactions for chemical and biochemical applications. *Chem. Rev.*, 116(9):5301–5337, 2016.

[196] M. Rupp, A. Tkatchenko, K.-R. Mueller, and O. A. Von Lilienfeld. Fast and accurate modeling of molecular atomization energies with machine learning. *Phys. Rev. Lett.*, 108 (5):058301, 2012.

[197] K. Hansen, G. Montavon, F. Biegler, S. Fazli, M. Rupp, M. Scheffler, O. A. Von Lilienfeld, A. Tkatchenko, and K.-R. Mueller. Assessment and validation of machine learning methods for predicting molecular atomization energies. *J. Chem. Theory Comput.*, 9(8): 3404–3419, 2013.

[198] K. Hansen, F. Biegler, R. Ramakrishnan, W. Pronobis, O. A. Von Lilienfeld, K.-R. Mueller, and A. Tkatchenko. Machine learning predictions of molecular properties: Accurate many-body potentials and nonlocality in chemical space. *J. Phys. Chem. Lett*, 6 (12):2326–2331, 2015.

[199] A. P. Bartok, S. De, C. Poelking, N. Bernstein, J. Kermode, G. Csanyi, and M. Ceriotti. Machine learning unifies the modelling of materials and molecules. *arXiv:1706.00179*, 2017.

[200] K. T Schuett, F. Arbabzadah, S. Chmiela, K. R. Mueller, and A. Tkatchenko. Quantum-chemical insights from deep tensor neural networks. *Nature Comm.*, 8:13890, 2017.

[201] J. Gilmer, S. S. Schoenholz, P. F. Riley, O. Vinyals, and G. E. Dahl. Neural message passing for quantum chemistry. *arXiv:1704.01212*, 2017.

[202] R. Ramakrishnan, P. O. Dral, M. Rupp, and O. A. Von Lilienfeld. Big data meets quantum chemistry approximations: the δ-machine learning approach. *J. Chem. Theory Comput.*, 11(5):2087–2096, 2015.

[203] P. O. Dral, O. A. Von Lilienfeld, and W. Thiel. Machine learning of parameters for accurate semiempirical quantum chemical calculations. *J. Chem. Theory Comput.*, 11 (5):2120–2125, 2015.

[204] M. Kubillus, T. Kubar, M. Gaus, J. Rezac, and M. Elstner. Parameterization of the dftb3 method for br, ca, cl, f, i, k, and na in organic and biological systems. *J. Chem. Theory Comput.*, 11(1):332–342, 2014.

[205] A. P. Bartok, R. Kondor, and G. Csanyi. On representing chemical environments. *Phys. Rev. B*, 87(18):184115, 2013.

[206] B. Huang and O. A. Von Lilienfeld. Communication: Understanding molecular representations in machine learning: The role of uniqueness and target similarity. *J. Chem. Phys.*, 145(16):161102–161102, 2016.

[207] J. Friedman, T. Hastie, and R. Tibshirani. *The elements of statistical learning*, volume 1. Springer series in statistics New York, 2001.

[208] H. Steinhaus. Sur la division des corp materiels en parties. *Bull. Acad. Polon. Sci*, 1 (804):801, 1956.

[209] J. MacQueen. Some methods for classification and analysis of multivariate observations. In *Proceedings of the fifth Berkeley symposium on mathematical statistics and probability*, volume 1, pages 281–297. Oakland, CA, USA., University of California Press, 1967.

[210] K. Fukunaga and L. Hostetler. The estimation of the gradient of a density function, with applications in pattern recognition. *IEEE Trans. Inf. Theory*, 21(1):32–40, 1975.

[211] Y. Cheng. Mean shift, mode seeking, and clustering. *IEEE Trans. Pattern Anal. Mach. Intell.*, 17(8):790–799, 1995.

[212] F. Pedregosa, G. Varoquaux, A. Gramfort, V. Michel, B. Thirion, O. Grisel, M. Blondel, P. Prettenhofer, R. Weiss, V. Dubourg, J. Vanderplas, A. Passos, D. Cournapeau, M. Brucher, M. Perrot, and E. Duchesnay. Scikit-learn: Machine learning in Python. *Journal of Machine Learning Research*, 12:2825–2830, 2011.

[213] S. Van der Walt, S. C. Colbert, and G. Varoquaux. The numpy array: a structure for efficient numerical computation. *Comput. Sci. Eng.*, 13(2):22–30, 2011.

[214] R. Ramakrishnan, P. O. Dral, M. Rupp, and O. A. Von Lilienfeld. Quantum chemistry structures and properties of 134 kilo molecules. *Sci. Data*, 1:140022, 2014.

[215] L. Ruddigkeit, R. Van Deursen, L. C. Blum, and J.-L. Reymond. Enumeration of 166 billion organic small molecules in the chemical universe database gdb-17. *J. Chem. Inf. Mod.*, 52(11):2864–2875, 2012.

[216] K. Pearson. Liii. on lines and planes of closest fit to systems of points in space. *Philos. Mag.*, 2(11):559–572, 1901.

[217] H. Hotelling. Analysis of a complex of statistical variables into principal components. *J. Ed. Psycho.*, 24(6):417, 1933.

[218] K. W. Sattelmeyer, J. Tirado-Rives, and W. L. Jorgensen. Comparison of scc-dftb and nddo-based semiempirical molecular orbital methods for organic molecules. *J. Phys. Chem. A*, 110(50):13551–13559, 2006.

[219] H. Oberhofer, K. Reuter, and J. Blumberger. Charge transport in molecular materials: An assessment of computational methods. *Chem. Rev.*, 117(15):10319–10357, 2017.

[220] R. P. Fornari, J. Arago, and A. Troisi. Exciton dynamics in phthalocyanine molecular crystals. *J. Phys. Chem. C*, 120(15):7987–7996, 2016.

[221] P. Shushkov, R. Li, and J. C. Tully. Ring polymer molecular dynamics with surface hopping. *J. Chem. Phys.*, 137(22):22A549, 2012.

[222] G. D. Scholes. Long-range resonance energy transfer in molecular systems. *Ann. Rev. Phys. Chem.*, 54(1):57–87, 2003.

[223] F. Fassioli, R. Dinshaw, P. C. Arpin, and G. D. Scholes. Photosynthetic light harvesting: excitons and coherence. *J. Royal Soc. Interface*, 11(92):20130901, 2014.

[224] D. Beljonne, C. Curutchet, G. D. Scholes, and R. J. Silbey. Beyond forster resonance energy transfer in biological and nanoscale systems. *J. Phys. Chem. B*, 113(19):6583–6599, 2009.

[225] J. S. Smith, O. Isayev, and A. E. Roitberg. Ani-1: an extensible neural network potential with dft accuracy at force field computational cost. *Chem. Sci.*, 8(4):3192–3203, 2017.